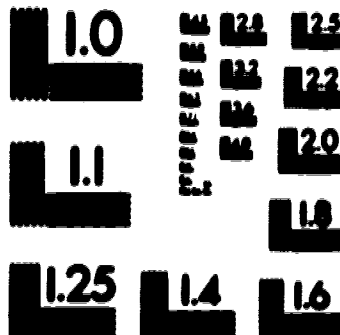


1

PM-1 3 1/2" x 4" PHOTOGRAPHIC MICROCOPY TARGET
NBS 1010a ANSI/ISO #2 EQUIVALENT



PRECISIONTM RESOLUTION TARGETS



National Library
of Canada

Acquisitions and
Bibliographic Services Branch

385 Wellington Street
Ottawa, Ontario
K1A 0N4

Bibliothèque nationale
du Canada

Direction des acquisitions et
des services bibliographiques

385, rue Wellington
Ottawa (Ontario)
K1A 0N4

Your file Votre référence :

Our file Notre référence :

NOTICE

The quality of this microform is heavily dependent upon the quality of the original thesis submitted for microfilming. Every effort has been made to ensure the highest quality of reproduction possible.

If pages are missing, contact the university which granted the degree.

Some pages may have indistinct print especially if the original pages were typed with a poor typewriter ribbon or if the university sent us an inferior photocopy.

Reproduction in full or in part of this microform is governed by the Canadian Copyright Act, R.S.C. 1970, c. C-30, and subsequent amendments.

AVIS

La qualité de cette microforme dépend grandement de la qualité de la thèse soumise au microfilmage. Nous avons tout fait pour assurer une qualité supérieure de reproduction.

S'il manque des pages, veuillez communiquer avec l'université qui a conféré le grade.

La qualité d'impression de certaines pages peut laisser à désirer, surtout si les pages originales ont été dactylographiées à l'aide d'un ruban usé ou si l'université nous a fait parvenir une photocopie de qualité inférieure.

La reproduction, même partielle, de cette microforme est soumise à la Loi canadienne sur le droit d'auteur, SRC 1970, c. C-30, et ses amendements subséquents.

Canada

UNIVERSITY OF ALBERTA

Downwash of Stack Gas Plumes

By

Clifton Reed Johnston



**A thesis submitted to the Faculty of Graduate Studies and Research in
partial fulfillment of the requirements for the degree of Master of
Science.**

DEPARTMENT OF MECHANICAL ENGINEERING

**EDMONTON, ALBERTA
SPRING 1994**



National Library
of Canada

Acquisitions and
Bibliographic Services Branch

385 Wellington Street
Ottawa, Ontario
K1A 0N4

Bibliothèque nationale
du Canada

Direction des acquisitions et
des services bibliographiques

385, rue Wellington
Ottawa (Ontario)
K1A 0N4

Your file Votre référence

Your file Votre référence

The author has granted an irrevocable non-exclusive licence allowing the National Library of Canada to reproduce, loan, distribute or sell copies of his/her thesis by any means and in any form or format, making this thesis available to interested persons.

L'auteur a accordé une licence irrévocable et non exclusive permettant à la Bibliothèque nationale du Canada de reproduire, prêter, distribuer ou vendre des copies de sa thèse de quelque manière et sous quelque forme que ce soit pour mettre des exemplaires de cette thèse à la disposition des personnes intéressées.

The author retains ownership of the copyright in his/her thesis. Neither the thesis nor substantial extracts from it may be printed or otherwise reproduced without his/her permission.

L'auteur conserve la propriété du droit d'auteur qui protège sa thèse. Ni la thèse ni des extraits substantiels de celle-ci ne doivent être imprimés ou autrement reproduits sans son autorisation.

ISBN 0-612-11259-4

Canada

UNIVERSITY OF ALBERTA

RELEASE FORM

NAME OF AUTHOR: Clifton Reed Johnston

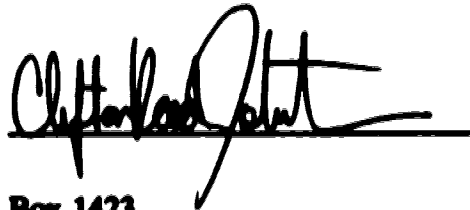
TITLE OF THESIS: Downwash of Stack Gas Plumes

DEGREE: Master of Science

YEAR THIS DEGREE GRANTED: Spring 1994

Permission is hereby granted to the University of Alberta Library to reproduce single copies of this thesis and to lend or sell such copies for private, scholarly or scientific research purposes only.

The author reserves all other publication and other rights in association with the copyright in the thesis, and except as hereinbefore provided neither the thesis nor any substantial portion thereof may be printed or otherwise reproduced in any material form whatever without the author's prior written permission.

A handwritten signature in black ink, appearing to read 'Clifton Reed Johnston', is written over a horizontal line.

Box 1423
Devon, Alberta
T0C 1E0

Date: January 17, 1994

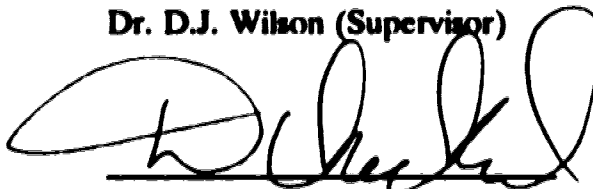
UNIVERSITY OF ALBERTA

FACULTY OF GRADUATE STUDIES AND RESEARCH

The undersigned certify that they have read, and recommend to the Faculty of Graduate Studies and Research for acceptance, a thesis entitled **DOWNWASH OF STACK GAS PLUMES** submitted by Clifton Reed Johnston in partial fulfillment of the requirements for the degree of Master of Science.



Dr. D.J. Wilson (Supervisor)



Dr. M.D. Checkel (Co-Supervisor)



Dr. L.W. Sigurdson



Dr. F. Hicks

Date: January 15, 1994

To my parents and Calleigh

Abstract

To determine the ~~area~~ near plume releases the relative height of the plume to the ground must be determined. Since the worst hazards occur when the plume is downwashed, the height of a downwashed plume relative to the ground is important. To predict the trajectory of a plume experiencing downwash a accurate model of downwash is necessary.

This study ~~was undertaken~~ to develop a new model for downwash, which would accurately predict the trajectories of plumes over a wide range of stack operating conditions. A downwash velocity model was derived specifically for this thesis. The downwash velocity model incorporates the effects of a time averaged pair of diverging line vortices in the rise of a plume. The line vortices are assumed to be imbedded in the wake at the stack tip height and move apart at the same rate as the wake spreads. The line vortices produce a negative velocity which causes a downward displacement of the plume. The downwash velocity model was found to predict, for subcritical Reynolds number flows, the trajectory of plumes to within $\pm 2\%$ over exit velocities ranging from 0 to 8 times the free stream velocity. An entrainment coefficient which varies based on the momentum ratio was used, and was found to predict plume trajectories more accurately than a constant entrainment coefficient of 0.6. A discussion of the effects of increasing Reynolds number on the downwash velocity model was conducted, highlighting some of the differences and similarities between modelled and full scale plumes. Two other downwash models were presented for comparison: Briggs' virtual origin correction and an initial entrainment model.

The visualization of the time averaged vortex pair at the stack tip, using a new and innovative method for applying fluorescein dye directly to the stack surface, provided the basis needed for the development of the downwash velocity model by substantiating the presence of the streamwise vorticity at the stack tip. Using the velocity measurements the exponent of the wake growth at the stack tip was determined to be 0.4, based on both the experimental values determined in this study and an average of the theoretical values for a two and three-dimensional wake.

Using the simple assumption that the line vortices grow apart at the rate the wake thickness increases produces an easy to use closed form solution for a downwash velocity, which very accurately corrects the trajectory of a downwashed plume.

Acknowledgements

I would like to start by thanking Dr. D. J. Wilson for his guidance and counsel throughout the development of this thesis, and for affording me the opportunity to explore the world of research. His advise over the bulk of my academic career is greatly appreciated. Dr. M. D. Checkel also deserves a vote of thanks for his help over the course of this thesis. Special thanks are extended to Dr. L. Sigurdson. His timely advise on flow visualization and insightful guidance with the vortex dynamics of this problem, allowed the construction of the model presented in this thesis. I would like to especially thank Wayne Pittman for his near brilliant suggestions on how to solve what seemed like the most insurmountable problems. Thanks also to Al Muir and all the machine shop staff for their excellent and expedient work. I am grateful to Fred Lui and Shanon Warner for their assistance in the collection of velocity and concentration measurements. Financial support from the Natural Science and Engineering Research Council and Luscar Ltd. was greatly appreciated.

I am very grateful for the support of my friends, especially Bill Peck and Eric van Meurs. Without them I would have long ago lost my sanity; thanks guys! I would also like give special thanks to my parents for their endless support, without which this thesis would never had been possible. Finally, I would like to thank Calleigh. Her constant support and love, even when things took longer than expected and we had to be 500 km apart, made completing this thesis a reality. Thanks.

Table of Contents

Chapter 1 Introduction	1
Chapter 2 Modelling Plume Rise and Downwash	4
2.1 Introduction	4
2.2 Plume Rise Equations	4
2.3 Downwash Models	10
2.3.1 Virtual Origin Downwash Correction	10
2.3.2 Initial Entrainment Downwash Correction	12
2.3.3 Continuous Downwash Velocity Correction	13
2.4 Summary	26
Chapter 3 Laboratory Simulation Methods and Equipment	27
3.1 Introduction	27
3.2 Water Channel	27
3.3 Velocity Measurements	29
3.4 Concentration Measurements	30
3.4.1 Behaviour of Disodium Fluorescein Dye	33
3.4.2 Image Processing Equipment	34
3.5 Flow Visualization by Surface Application of Fluorescein	42
3.6 Stack Orientation	47
3.7 Viewing Plume Cross Sections	47
3.8 Summary	50
Chapter 4 Flow Visualization of Vortex Shedding	52
4.1 Introduction	52
4.2 Tracking Vorticity	52
4.3 The von Karman Vortex Street	55
4.4 Visualization of Streamwise Tip Vortices	57

4.5 Effects of Stack Effluent Jet on Vortex Structure	61
4.6 Summary	61
 Chapter 5 Velocity Measurements	 64
5.1 Introduction	64
5.2 Velocity Measurements of the Water Channel	64
5.3 Stack Model Development	64
5.3.1 Average Velocity Correction for Momentum Flux	68
5.4 Selecting Averaging Time and Sampling Rate for Plume Images ..	72
5.5 Wakes Behind Cylinders	73
5.5.1 Two Dimensional Wakes	76
5.5.2 Tip Wake	76
5.5.3 The Wake around the Tip with a Strong Exit Jet	79
5.6 Determining the Exponent for the Downwash Velocity Model ...	84
5.7 Summary	84
 Chapter 6 Comparison of Downwash Models to Experimental Data	 86
6.1 Introduction	86
6.2 Effects of Entrainment Coefficient on Predicting Plume Trajectories	86
6.2.1 The Fully Bent-Over Assumption for Non-buoyant Plumes	90
6.2.2 Added Mass Acceleration Effects on the Entrainment Coefficient	92
6.3 Virtual Origin Downwash Correction	93
6.4 Initial Entrainment Downwash Correction	93
6.5 Downwash Velocity Correction	96
6.6 Reynolds Number Effects on the Downwash Velocity Model	108
6.6.1 Reynolds Number Effects on Base Pressure Coefficient ..	110
6.6.2 Reynolds Number Effects on Wake Growth	112
6.6.3 Reynolds Number Effects on Vortex Shedding	112
6.7 Application of Downwash Velocity Model to Buoyant Plumes ...	115
6.8 Empiricism in the Downwash Velocity Model	116

Chapter 7 Summary and Recommendations	119
7.1 Summary	119
7.2 Recommendations	121
 References	 123
 Appendix A Derivation of Plume Rise Equation	 127
 Appendix B Ratio of Length Scales for Vorticity and Dye Diffusion	 135

List of Tables

Table 6-1:	Entrainment coefficients from various studies over a range of Momentum ratios.	88
Table 6-2:	Vertical vs. Fully Bent-Over Portions of Trajectory	90

List of Figures

Figure 2-1:	Schematic of plume illustrating characteristic Parameters used in the development of the plume rise equations.	6
Figure 2-2:	Characteristic differences between virtual origin correction, the initial entrainment model and the downwash velocity model.	11
Figure 2-3:	Comparison between von Karman vortex shedding with cross connecting bridges and the time averaged vortex pair used in the downwash velocity model.	14
Figure 2-4:	Velocity vectors in a crosswind plane of Sherlock and Stalker's stack suggesting the presence of a streamwise vortex pair.	15
Figure 2-5:	Schematic of variables used to calculate the velocity at a point due to the influence of a line vortex.	18
Figure 2-6:	Schematic of the vortex pair outside the plume and the vortex pair imbedded in the plume.	21
Figure 2-7:	Downwash velocity model.	23
Figure 3-1:	Water Channel.	28
Figure 3-2:	Positions of light stands, injector and camera relative to the water channel, viewed from above.	32
Figure 3-3:	Video camera electronic shutter operation.	36
Figure 3-4:	Schematic diagram of image acquisition and processing system.	37

Figure 3-5:	Non-linear concentration correction of the complete image processing system.	41
Figure 3-6:	Schematic of dye injection apparatus and stack position looking upstream.	48
Figure 3-7:	Illustration of the orientations used for viewing two plume sections.	49
Figure 4-1:	Vorticity production on a cylinder.	53
Figure 4-2:	Concentration contour plot of a time averaged y-z cross section looking upstream of the von Karman vortex street at a) $x=2D$ and b) $x=30D$ downstream.	59
Figure 4-3:	Concentration contour plot of a time averaged y-z cross section looking upstream of the von Karman vortex street with centroid flutter removed at a) $x=2D$ and b) $x=30D$ downstream.	60
Figure 5-1:	Cross stream profiles of mean velocity and streamwise turbulence intensity at $x/D = 0$.	65
Figure 5-2:	Vertical profiles of mean velocity and streamwise turbulence intensity at $x/D = 0$.	66
Figure 5-3:	Stack model and fluted turbulence generator plug.	67
Figure 5-4:	Mean velocity and turbulence intensity profiles in quiescent fluid ($U_a = 0$) at $x = 0.5D$ from the stack exit with no turbulence generator inside stack.	69
Figure 5-5:	Mean velocity and turbulence intensity profiles in quiescent fluid ($U_a = 0$) at $x = 0.5D$ from the stack exit with fluted turbulence generator in place.	71

Figure 5-6:	Fifty second mean and standard deviation of rise height for various image sampling rates with $M = 3.0$ at $x = 30D$ downstream.	74
Figure 5-7:	Fifty second mean and standard deviation of rise height for various image sampling rates with $M = 0.5$ at $x = 30D$ downstream.	75
Figure 5-8:	Velocity profiles behind an infinite (full channel width) cylinder for six downstream locations. Wake width $\delta_y = (x-x_0)^{0.40}$ defined at $\Delta U/2$ (Note: x positions not to scale).	77
Figure 5-9:	Growth of momentum wake and wake invariant for a two dimensional wake behind an "infinite" (full channel width) cylinder.	78
Figure 5-10:	Vertical velocity profiles behind an open ended tube with $M = 0$ for six downstream locations. Wake height $\delta_z = (x-x_0)^{0.36}$ defined by $\Delta U/2$ (Note: x positions not to scale).	80
Figure 5-11:	Vertical growth of transition region between freestream flow and two-dimensional wake and wake invariant for three dimensional axisymmetric wake.	81
Figure 5-12:	Velocity profiles behind the tip of a cylinder with a strong jet ($M = 6.0$) exiting for six downstream locations. Wake width $\delta_y = (x-x_0)^{0.39}$ defined by $\Delta U/2$ (Note: x positions not to scale).	82
Figure 5-13:	Crosswind momentum wake width and two dimensional wake invariant at stack tip height behind a strong jet ($M = 6.0$).	83
Figure 6-1:	Comparison between experimental data and plume rise equation with a constant entrainment coefficient, $\beta=0.6$,	

	for $M = 4.0, 6.0$ and 8.0	87
Figure 6-2:	Variation of entrainment coefficient with momentum ratio.	89
Figure 6-3:	Comparison between experimental data and plume rise equation using variable entrainment coefficient.	91
Figure 6-4:	Predicted plume trajectories with no downwash correction and corresponding experimental data for $M=0.25$(diamonds), 0.5(circles), 1.0(squares) and 1.5(triangles).	94
Figure 6-5:	Predicted plume trajectories using Briggs' downwash correction and corresponding experimental data for $M=0.25$(circles), 0.75(squares) and 1.5(triangles).	95
Figure 6-6:	Initial entrainment downwash model predictions for $M = 0.25, 0.75, 1.0, 1.5$ and 2.0.	97
Figure 6-7:	Downwash correction coefficient for a constant entrainment coefficient, $\beta = 0.6$.	98
Figure 6-8:	Predicted trajectories using the downwash velocity model for a constant entrainment coefficient, $\beta = 0.6$.	99
Figure 6-9:	Downwash correction coefficient for variable entrainment coefficient.	101
Figure 6-10:	Predicted trajectories using the downwash velocity model for variable entrainment coefficient.	102
Figure 6-11:	Measured concentration profiles at $x = 2D$ for $M = 6.0$ and 0.25.	104
Figure 6-12:	Plume cross section concentration contour plots for	

M = 0.25 at x = 2D, 5D, 10D and 30D.	105
Figure 6-13: Plume cross section concentration contour plots for M = 1.5 at x = 5D, 10D and 30D.	106
Figure 6-14: Plume cross section concentration contour plots for M = 6.0 at x = 5D 10D and 30D.	107
Figure 6-15: Comparison between centroids calculated using an x-z light sheet plane (empty symbols) and a y-z cross section (filled symbols).	109
Figure 6-16: Downwash velocity model predictions compared to Snyder and Lawson's wind tunnel data for subcritical Reynolds numbers.	111
Figure 6-17: Base pressure coefficients for an infinite circular cylinder, from Neiman.	113
Figure 6-18: Rise of typical buoyant stack gas plumes for various momentum and density ratios ($U_0 = 18$ Km/hr, $D = 2$m, $Q_0 = 15.71$ m³/s).	117

List of Plates

Plate 2-1:	False coloured image of time averaged stack wake ($U_{avg}/D = 1041$).	16
Plate 2-2:	False coloured image of instantaneous (1/250 sec) wake showing the shedding of the von Karman vortex street.	16
Plate 3-1:	Laser and splitting optics used in PLIF.	31
Plate 3-2:	Optics stand and Optics used to produce a laser sheet.	31
Plate 3-3:	False colored, time averaged images for $M = 0.25, 1.5, 3.0$ and 8.0.	44
Plate 3-4:	Painting stack with fluorescein for flow visualization.	46
Plate 4-1:	von Karman vortex street shed off a 9.6 mm O.D. finite cylinder at a Strouhal number of 0.19.	56
Plate 4-2:	Connection of two vortices in the von Karman vortex street.	56
Plate 4-3:	Cross sectional stack wake looking upstream at approximately $x = 10D$ downstream showing the presence of alternating streamwise line vortex at the stack tip height (Time delay between pictures $\Delta t U/D = 6.25$).	58
Plate 4-4:	von Karman vortex street interacting with a plume exiting the stack.	62
Plate 5-1:	Fluted Turbulence generator plugs tested.	70

Symbols and Nomenclature

B_3	Downwash correction coefficient using external vortex model
$B_{3,e}$	Downwash correction coefficient using embedded vortex model
C	Pixel concentration
C_{bp}	Base pressure coefficient
D	Outside diameter of stack
f	von Karman vortex street shedding frequency
F_b	Plume buoyancy flux normalized by ambient density
F_m	Plume momentum flux normalized by ambient density
h	Total rise of plume
h_b	Plume rise height due to buoyancy
h_d	Downwash correction using external vortex model
$h_{d,e}$	Downwash correction using embedded vortex model
h_m	Plume rise height due to momentum
I	Pixel intensity
K_{dye}	Diffusion coefficient for fluorescein
M	Momentum ratio
n	exponent of wake growth
Q_d	Initial downwash entrainment
Q_p	Plume volume flux
Q_s	Volume flux at stack exit
R_d	Downwash radius for initial entrainment model
Re_d	Reynolds number $Re_d = U_s D / \nu$
R_o	Initial radius of fully bent-over plume
R_p	Plume Radius
R_s	Inside radius of stack
R_{sep}	Distance from vortex core to wake centerline
Sc	Schmidt number $Sc = \nu / K_{dye}$
St	Strouhal number $St = fD / U_s$
U_s	Free stream velocity
U_t	Velocity tangential to path around stack tip line vortex
u_p	Streamwise plume velocity
$u_{surface}$	Velocity outside boundary layer on cylinder
v_e	Entrainment velocity
w_d	Downwash velocity using external vortex model

$w_{d,e}$	Downwash velocity using embedded vortex model
w_p	Vertical plume velocity
w_s	Plume velocity at stack exit
x_n	Virtual origin for wake growth
x	Distance downstream
y	Cross stream distance
z	height above stack tip

Greek Symbols

α_m	Stack momentum correction factor
β	Entrainment coefficient
Γ_d	Circulation of stack tip line vortex
δ	Wake separation
δ_ω	Scaling parameter for vorticity diffusion
δ_c	Scaling parameter for dye diffusion
θ	Angle of plume with the horizontal axis
ρ_a	Ambient density
ρ_s	Density of plume at stack exit
ν	Kinematic viscosity
ω	vorticity

Chapter 1

Introduction

This study was undertaken to develop a new downwash model that would accurately predict the trajectories of plumes over a wide range of stack operating conditions. Three downwash models will be presented: Briggs' virtual origin correction, an initial entrainment model and the downwash velocity model. The downwash velocity model and initial entrainment model were specifically derived for this thesis, but the virtual origin correction and the initial entrainment model were used primarily for comparison. The development of the downwash velocity model encompassed many areas of study such as laser induced fluorescence, visualization of vortex structure shed from a cylinder, self-similar momentum wakes and plume rise. The study of these areas culminated in an accurate, easy to use model for predicting downwash.

The study of downwash has roots back 50 years, when Sherlock and Stalker (1941) began studying the problem. Their determination that downwash occurs in plumes with ratios of stack exit velocity to free stream velocity lower than 1.5 is still widely accepted, see Ooms (1972), Briggs (1975), Rittmann (1982) and Weil (1988). Sherlock and Stalker (1941) were also the first to suggest that a coherent vortex structure was the mechanism for downwash. They found a streamwise vortex pair at the stack tip that they felt would cause a plume to be forced down into the von Karman vortex street. The von Karman vortex street would then transport the material toward the ground. Sherlock and Stalker (1941) envisioned the von Karman vortex street as being finite, ending in space at the height of the stack. While their analysis of the vortex dynamics of the flow around a cylinder was inaccurate, the use of a vortex model in downwash will be shown to give the best estimate of plume trajectory.

Very little experimental work has been done on downwash since Sherlock and Stalker (1941). Of the few new models for downwash that exist, all ignored the vortex measurements reported by Sherlock and Stalker (1941). The currently accepted method of accounting for downwash was proposed by Briggs (1973). His method of correcting for downwash was an empirically derived virtual origin correction. The basis for Briggs' correction is the assumption that the low pressure region in the lee of the stack sucks the plume down, producing downwash. This

assumption has been widely accepted by Scorer (1959), Overcamp and Hoult (1971), Weil (1988), Carhart and Policastro (1991), and Snyder and Lawson (1991) as the physical explanation for downwash.

Scorer (1968) suggested that placing an annular disk, one stack diameter wide, at the stack tip would shield the plume from the low pressure region. This method was adopted in the design of many stacks, but never achieved the success Scorer envisioned. The examination of the trajectories of downwashed plumes indicates that plumes are being pushed down long after the force due to the low pressure region has become negligible, suggesting the low wake pressure near the stack is not the sole mechanism in downwash.

The most recent investigation of downwash was conducted by Snyder and Lawson (1991). They investigated the effect of changing Reynolds number on downwash. Their findings suggested a plume exiting into a subcritical Reynolds number flow ($Re_d < 2 \times 10^5$) will experience more downwash than a plume exiting into a supercritical Reynolds number flow ($Re_d > 2 \times 10^5$). While this is an interesting result with definite consequences for downwash models, Snyder and Lawson (1991) did not suggest a physical explanation for the results, nor did they present any new models for predicting downwash. Snyder and Lawson continued to assume that downwash is caused by the low pressure region behind the stack. They did, however, conclude that Briggs' virtual origin correction is too conservative in its prediction of downwash, and a more sophisticated model for downwash is required.

At present, Briggs' virtual origin correction is the downwash correction used by regulatory agencies like Alberta Environment and the U.S Environmental Protection Agency. Briggs' correction is used, despite the fact it is too simple, because no models exist which are as easy to use and more accurately predict plume trajectories.

The downwash velocity model in this thesis will be derived, picking up from where Sherlock and Stalker (1941) left off, by modelling a time averaged vortex pair at the stack tip. This pair of line vortices influences the trajectory of a plume by superimposing a downwash velocity on the plume's vertical velocity. The plume rise model used in this thesis will also be evaluated and a variable entrainment coefficient correction proposed for the rise of a fully bent-over plume.

The mechanisms of laser induced fluorescence and the process of digital image processing will be explained and their adaptations for determining plume concentration profiles presented. A new method of applying fluorescein dye to a surface, for use

in visualizing the vortex structure from a finite cylinder, will also be described.

The results of the flow visualization experiments to determine the vortex structure shed from a finite cylinder and of the experiments on wake development behind the stack will be presented. By comparing theoretical predictions of trajectory by the virtual origin, initial entrainment and downwash velocity corrections to experimental data, the downwash velocity model will be shown to most accurately predict the trajectories of plumes.

Chapter 2

Modelling Plume Rise and Downwash

2.1 Introduction

One of the first analytical studies dealing with entrainment in a rising plume was carried out by Morton, Taylor and Turner (1956). In the time since, at least five different methods for modelling the rise of a plume have been developed. In this thesis, however, the object was not to develop a new model to describe plume rise, but to develop a model to describe plume downwash. The problem of downwash is one that has been investigated systematically for over the past 50 years. Sherlock and Stalker (1941) considered the problem of downwash and suggested placing a nozzle on the top of the stack to reduce downwash. Only a few methods for predicting downwash have developed, such as Briggs' virtual origin correction, introduced by Briggs (1973). By Briggs' (1984) own admission, "Little guidance is available on how to calculate plume rise if downwash does occur".

This chapter will be concerned with the physical and theoretical description of plume rise and downwash. Briggs' existing model for plume rise will be presented and an equation for the rise of a bent-over plume derived. Once the foundations of plume rise are presented, three methods of modelling plume downwash will be considered: a virtual origin correction, an initial entrainment correction and a downwash velocity correction. Each of the three models will be described and the equations governing them derived.

2.2 Plume Rise Equations

The plume rise model used in this thesis is the same model used by Briggs (1975). His derivation of the plume rise equations has been followed by Weil (1988), Davidson (1989) and Snyder and Lawson (1991).

The modelling of plumes is based on the balance of mass, momentum and thermal energy through a cylindrical plume element. The model includes several key assumptions.

- The plume is fully bent-over for its entire rise and has a circular cross section.
- The density difference between the plume and the ambient air is important only in the buoyancy force terms, but not in the inertial terms.

- The free stream velocity is constant above the height of the stack exit, and the bent-over plume is carried downstream at the wind speed, U_a (This means spatial derivatives can be re-written using the relationship $d/dx = U_a d/dt$).
- Plume rise is not affected by ambient turbulence.
- The model for the plume is one dimensional varying only with x , having uniform velocity and concentration across the cross section.

As the plume rises it entrains ambient fluid at its edges and increases its volume. The entrainment is described by an entrainment velocity, v_e . Figure 2-1 illustrates the entrainment velocity concept and the other basic quantities used in the balances. The subscript, s , indicates a source quantity, subscript, p , a plume quantity and subscript, a , quantities from the atmosphere.

Conservation of mass for the plume can be determined by examining a cylindrical control volume through which the plume passes. By integrating over the control volume, the increase in volume flux is

$$\frac{dQ_p}{dx} = 2R_p v_e \quad (2-1)$$

The RHS of Equation 2-1 should be $2\pi R_p v_e$ but the π is deleted to follow the convention of Morton, Taylor and Turner (1956). This equation says the increase of the total volume flux is equal to the total inflow at the plume outer surface. The cross section in Figure 2-1 also illustrates how entrainment is modelled using the entrainment velocity.

Although the present experiments did not model buoyancy effects, buoyancy can be important. The conservation of thermal energy can be used to show that buoyancy flux is conserved at each cross section of the plume. The buoyancy flux at the stack exit is the product of the buoyancy force per unit mass and the mass flow rate at the source. The buoyancy force per unit mass of stack gas is $g(\rho_a - \rho_s)/\rho_s$ and the source mass flow rate is $\rho_s \pi R_s^2 w_s$. The buoyancy flux becomes

$$F_b = g \left(\frac{\rho_a - \rho_s}{\rho_s} \right) w_s R_s^2 \quad (2-2)$$

The RHS of Equation 2-2 should be $w_s \pi R_s^2$, but the π is deleted to follow the

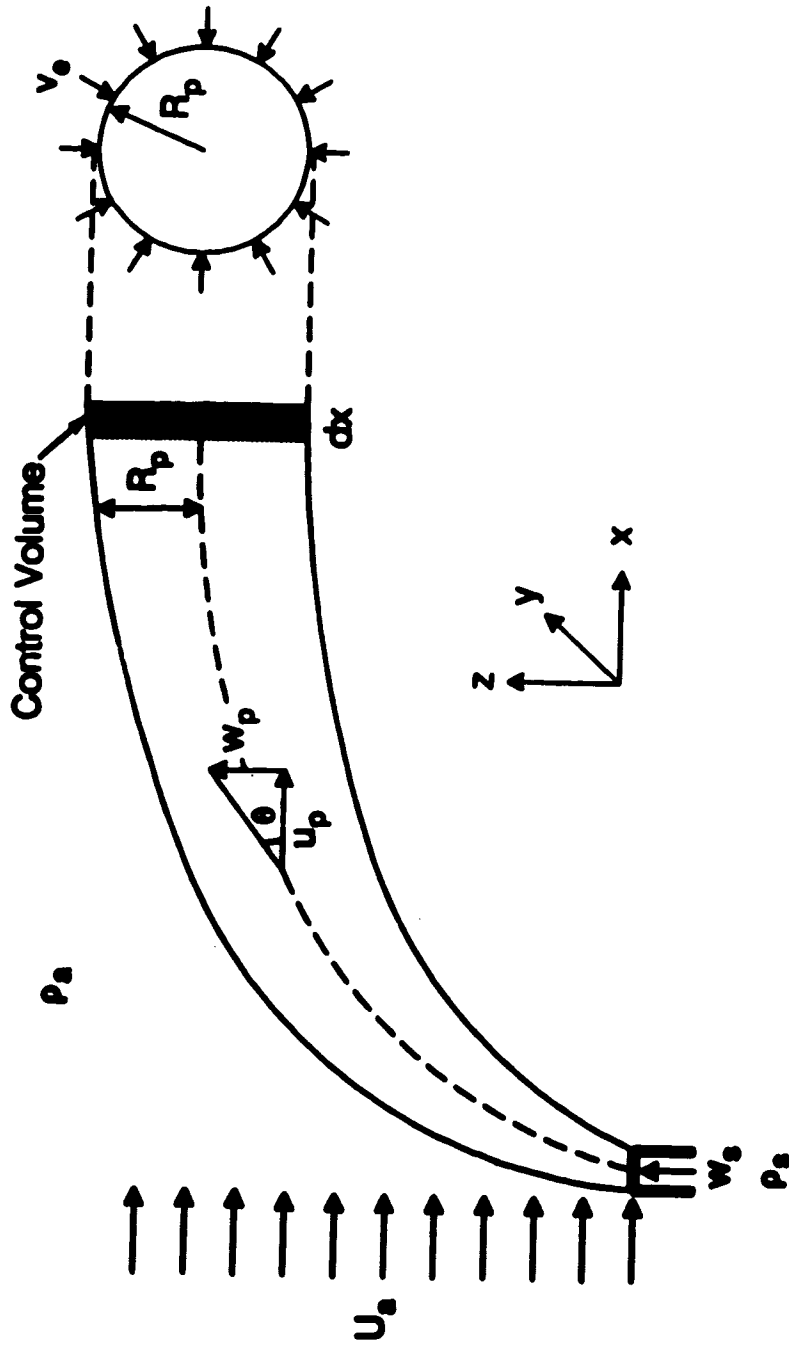


Figure 2-1: Schematic of plume illustrating characteristic Parameters used in the development of the plume rise equations.

convention of Morton, Taylor and Turner (1956). Using the Boussinesq approximation from Briggs (1975), $(\rho_p - \rho_a) \ll \rho_a$, the density of the plume is assumed to be close to the ambient density for most of the rise, so ρ_a is used as the normalizing density. The momentum flux, F_m , of the plume is defined in the same manner as the buoyancy flux. For a cylindrical plume element of radius R_p and length dx , we need only consider the conservation of momentum in the vertical direction. The vertical plume mass flux is matched to the bent-over plume mass flux to maintain mass conservation. The momentum flux is defined as the product of the vertical stack gas momentum per unit mass $(\rho_p w_p)/\rho_a$, and its mass flow rate $\rho_a \pi R_p^2 w_p$,

$$F_m = \frac{\rho_p}{\rho_a} w_p^2 R_p^2 \quad (2-3)$$

The RHS of Equation 2-3 also has the π deleted and is normalized by the ambient density.

In order to determine the rise of a buoyant plume the entrainment velocity introduced in the mass balance must be related to the rise of the plume. This is done using the Morton, Taylor and Turner (1956) entrainment hypothesis. The rate at which ambient air is drawn into the plume is assumed to be linearly proportional to the velocity difference between the plume and the ambient air. When the plume is fully bent-over the relative velocity is $w_p = dh/dt$, so

$$v_e = \beta w_p \quad (2-4)$$

The constant of proportionality, β , is called the entrainment coefficient. In this derivation, constant β is used to obtain a closed form solution, but β actually varies with x and plume angle. The entrainment coefficient is trajectory averaged to match theoretical predictions to observed trajectories. For example, a vertical jet has $\beta = 0.1$ and a trajectory averaged bent-over plume has $\beta > 0.6$, as reported by Briggs (1975). The experimental data in this thesis suggest a plume with a source velocity of about six times the free stream velocity will have a trajectory averaged β of approximately 0.45. Coelho and Hunt (1988) found that a plume which starts as a vertical jet will become bent-over due only to entrainment of ambient fluid. The entrainment coefficient would obviously change from the beginning to final stages of rise as the plume bends over. Hoult and Weil (1972), Weil (1988) and others use the same trajectory averaged β for both momentum and buoyant plumes. In this thesis,

Briggs' (1975) suggestion of using an entrainment coefficient that varies with exit velocity will be adopted. A further discussion of the entrainment coefficient will be found in Chapter 6.

From the analysis in Appendix A, the trajectory of a non-buoyant jet rising in a neutrally stable atmosphere is

$$h_m = \left(\frac{3}{\beta^2} \frac{F_m}{U_e^2} x \right)^{1/3} \quad (2-5)$$

This is known as the "1/3 Law" for momentum rise. A new variable, M , known as the momentum velocity ratio can be defined as

$$M = \left(\frac{\rho_s}{\rho_a} \right)^{1/2} \left(\frac{w_s}{U_e} \right) \quad (2-6)$$

Substituting Equation 2-3 and Equation 2-6 into Equation 2-5 yields

$$h_m = \left(\frac{3}{\beta^2} \right) M^{2/3} R_e^{2/3} x^{1/3} \quad (2-7)$$

This result contains quantities which are set during experimentation, making the calculation of rise less time consuming.

Hoult, Fay and Founney (1969) found the rise of a plume which has not yet bent past 45° would fit $x^{1/2}$ rather than $x^{1/3}$ but once the plume had bent-over it would again follow $x^{1/3}$. The $x^{1/2}$ dependence is due to their assumption that the plume only slightly departs from vertical in the early stages of rise. In this thesis, the "1/3 law" will be used for all times in the rise, but the entrainment coefficient will be varied.

Part of Appendix A reproduces, in the present notation, the analysis of Briggs (1975) for the rise, h_b , of a purely buoyant plume

$$h_b = \left(\frac{3}{2\beta^2} \frac{F_b}{U_e^2} x^2 \right)^{1/3} \quad (2-8)$$

This is the "2/3 Law" for buoyancy rise since $h_b \propto (x^2)^{1/3}$. The equation for the combined rise of a plume with both momentum and buoyancy, derived by Briggs

(1975) and used by Weil (1988) and Davidson (1989), is

$$h = \left(\frac{3}{\beta^2} \frac{F_m}{U_s^2} x + \frac{3}{2\beta^2} \frac{F_b}{U_s} x^2 \right)^{1/3} \quad (2-9)$$

Equation 2-9 combines the effects of both momentum and buoyancy for a point source release. Equation 2-9 can be written as the sum of cubes of h_m and h_b such that

$$h = (h_b^3 + h_m^3)^{1/3} \quad (2-10)$$

As Equation 2-10 suggests, either the momentum or buoyancy will dominate the rise of the plume. Near the stack, where downwash is most important, h_m is usually dominant, with h_b taking over at a transition point where $h_b = h_m$. In this thesis, it was assumed the transition occurred long after the region where downwash is of interest.

A correction can be applied to Equation 2-9 to account for the stack radius, R_s . An effective initial radius, R_o , suggested by Davidson and Slawson (1982) and refined by Davidson (1989), is incorporated in the plume rise equation. This initial radius, R_o , is determined by relating the vertical source mass flux to the bent-over mass flux. For the bent-over mass flux, the plume fluid moves downstream at speed U_s . The effective source radius is

$$R_o = \left(\frac{\rho_s w_s}{\rho_s U_s} \right)^{1/2} R_s \quad (2-11)$$

The radius of the plume, R_p , at any point during rise is then $R_p = \beta z + R_o$. From Equation A-30, the corrected plume rise equation will be

$$h = \left(\frac{3}{\beta^2} \frac{F_m}{U_s^2} x + \frac{3}{2\beta^2} \frac{F_b}{U_s} x^2 + \left(\frac{R_o}{\beta} \right)^3 \right)^{1/3} - \frac{R_o}{\beta} \quad (2-12)$$

for a fully bent-over buoyant jet with stack radius R_s or initial radius R_o .

2.3 Downwash Models

Over 30 investigations of plume trajectories, neglecting the effects of downwash, have been conducted by investigators from Bryant (1949), Sutton (1950), Fan (1967) and Hoult, Fay and Forney (1969) to more recent studies by Ooms (1972), Briggs (1975), Weil (1988) and Davidson (1989). Briggs (1984) noted that little attention has been paid to predicting trajectories of plumes experiencing downwash. As a result, the mechanism producing downwash was not fully understood. Only three explanations of downwash are widely known today. The most widely used explanation for downwash is that the low pressure area behind the stack affected the plumes ability to rise. This theory was advanced by Scorer (1968) who suggested downwash could be reduced by placing a flange at the stack exit to isolate the plume from the low pressure area. Briggs' (1984) stated that Scorer's disc method was limited in its ability to reduce downwash.

Perhaps downwash is due to a mechanism acting throughout the plume's rise (or descent in the case of a downwashed plume). Briggs (1984) suggested a method of accounting for downwash:

"One simple correction could be based on the growth of the stack wake width, which grows in proportion to $(Dx)^{1/2}$ (Overcamp and Hoult, 1971). Some fraction of this could be subtracted from the 2/3 law up to the distance calculated for final rise."

Starting with this suggestion, a downwash velocity model is derived here. For comparison, a virtual origin displacement and an initial entrainment model will also be presented.

2.3.1 Virtual Origin Downwash Correction

The most widely used correction for downwash was suggested by Briggs (1973). Briggs' correction is a virtual origin correction, h_v , that is subtracted from Equation 2-9. This correction is

$$h_v = 2.0(1.5 - M)D \quad \text{for } M < 1.5 \quad (2-13)$$

This correction does not alter the path of the plume but simply moves the source height lower. Figure 2-2a illustrates the application of a virtual origin and the

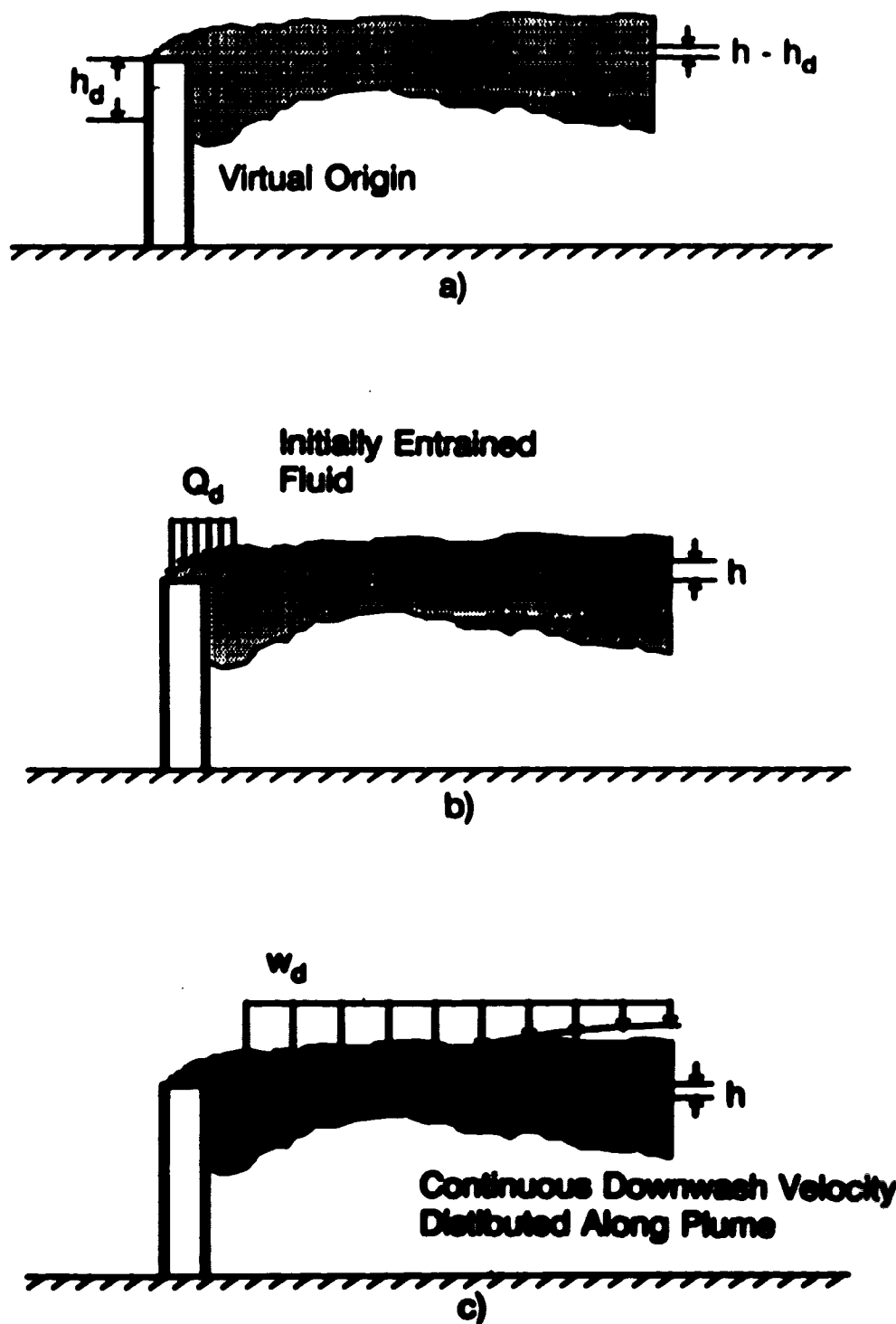


Figure 2-2: Characteristic differences between virtual origin correction, the initial entrainment model and the downwash velocity model.

unchanged plume trajectory. This model is used to correct for downwash by regulatory agencies such as Alberta Environment and the U.S. Environmental Protection Agency. Briggs (private correspondence), now suggests this correction is not robust enough to accurately account for plume downwash.

2.3.2 Initial Entrainment Downwash Correction

Another possible mechanism for downwash is increased air entrainment close to the stack. A model was developed for this thesis incorporating an initial entrainment, so that for low momentum ratios, usually $M < 1.5$, an increased amount of ambient fluid would be entrained into the plume. Figure 2-2b illustrates the entrainment process. The entrained air, Q_e , has no vertical velocity and acts to increase the mass of fluid the plume must transport upward. The entrainment velocity model used in the basic plume rise equation still applies with the addition of the initial entrainment at the origin. To incorporate this additional entrainment, the mass and vertical momentum balances must be re-evaluated. From Equation A-31, the mass balance for the plume is

$$\rho_s Q_s + \rho_a Q_e = \rho_s \pi R_d^2 U_s \quad (2-14)$$

where R_d is the effective source radius needed to accommodate the addition of Q_e . In the momentum balance we assume for simplicity that the density of the plume fluid after the addition of Q_e will remain close to the density of the stack fluid. The vertical momentum then becomes

$$\rho_s Q_s w_s + \rho_a Q_e w_e = \rho_s \pi R_d^2 U_s w_{p,d} \quad (2-15)$$

where $w_{p,d}$ is the plume vertical velocity with the initial entrainment included. We can now solve for rise height, including the initial radius, R_d , due to initial entrainment, so

$$h_m = \left(\frac{3}{\beta^2} \frac{F_m}{U_s^2} x + \left(\frac{R_d}{\beta} \right)^3 \right)^{1/3} - \left(\frac{R_d}{\beta} \right) \quad (2-16)$$

Where h_m is the momentum rise height and R_d is the effective initial radius due to the initial entrainment. The derivation of this equation is similar to the derivation for the initial radius R_s , and can be found in Appendix A. The value of Q_e is likely

a function of M . The effective radius R_d , for a non-buoyant plume, can be found using Equation A-37, where

$$R_d^2 = M \left(1 + \frac{Q_d}{Q_s} \right) R_s^2 \quad (2-17)$$

One difficulty in this model is that the correction is applied only at the stack exit, making the prediction of negative rise impossible.

2.3.3 Continuous Downwash Velocity Correction

This model was inspired by Briggs' (1984) suggestion of using a continuous downwash velocity, decreasing with x as the stack wake grew. The model developed here produces a correction caused by the interaction of the plume and a counter rotating vortex pair along the plume trajectory.

The streamwise vortex pair is created by the streamwise component of the bridges which link the von Karman vortex street. Performing our own flow visualization, the shedding of the vortex street, and the vortex street's linking bridges were observed. Figure 2-3a is a schematic of vortex shedding as seen in the flow visualization. The von Karman vortex street is shed obliquely to the stack and the sense of the cross linking vortices suggests a resulting downward velocity. However, the linking vortices do not produce a steady streamwise vortex pair, visible at all times, but rather a vortex pair that only appears in a time average (see Figure 4-3 for example). Figure 2-3b indicates how the vortex pair could be idealized as a time average. Sherlock and Stalker (1941) reported the existence of a vortex pair similar to that found in this study. Figure 2-4 is a result used to support their claim of a vortex pair's existence. While their measurement techniques were not as sophisticated as the methods used in this study, they did find evidence to support the idea of a tip vortex pair. However, Sherlock and Stalker (1941) did not link the vortex pair to the von Karman vortex street.

A second factor in downwash velocity model is linking the stack wake and the vortex pair. Plate 2-1 is a time averaged picture illustrating the growth of the wake behind the stack. The wake size, δ , increases at a rate proportional to the distance downstream. It is assumed the distance between the longitudinal vortex pair increases at a rate equal to the growth of the wake width. Plate 2-2 is an instantaneous (1/250 sec exposure) image of the wake behind the stack.

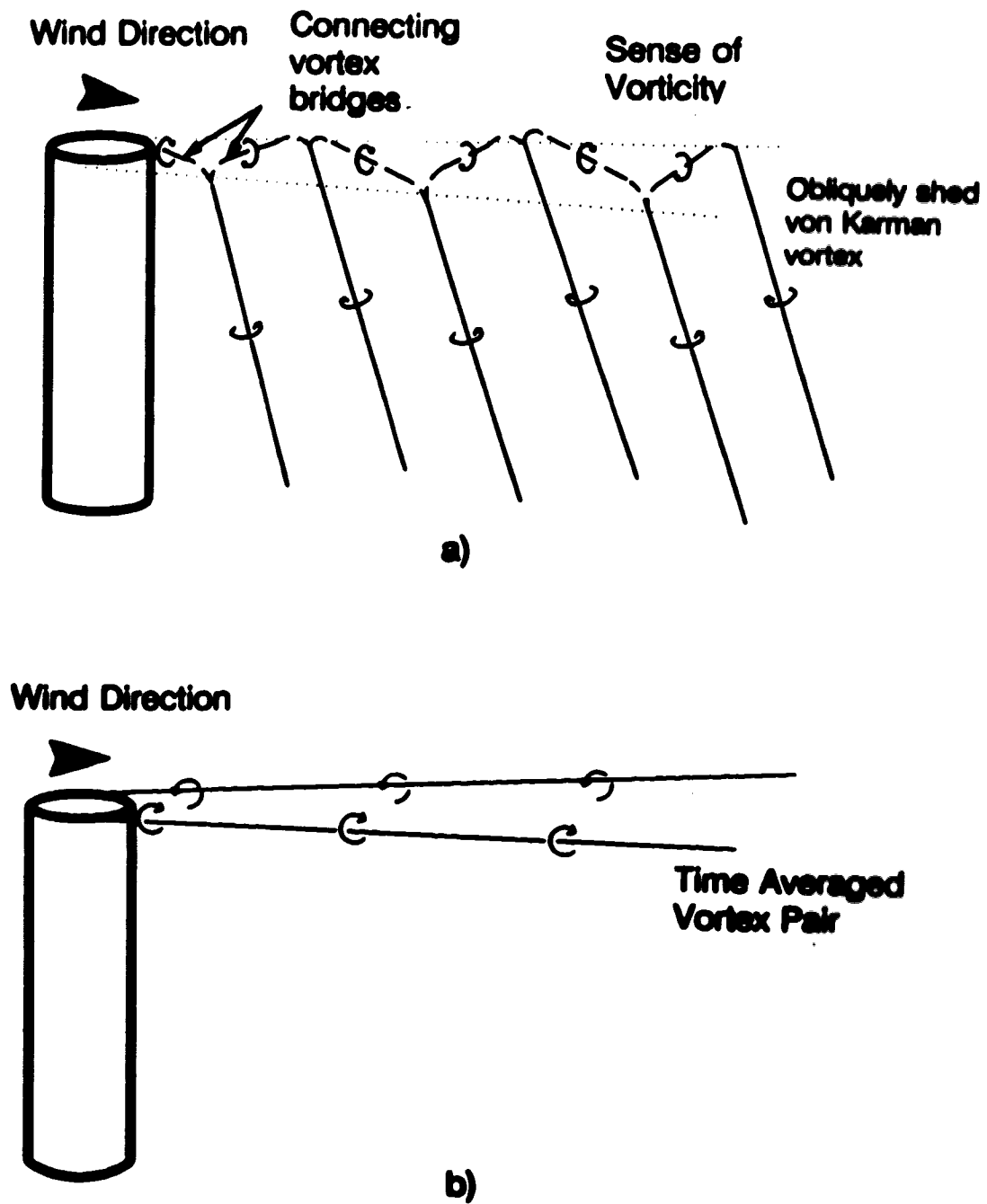


Figure 2-3: Comparison between von Karman vortex shedding with cross connecting bridges and the time averaged vortex pair used in the downwash velocity model.

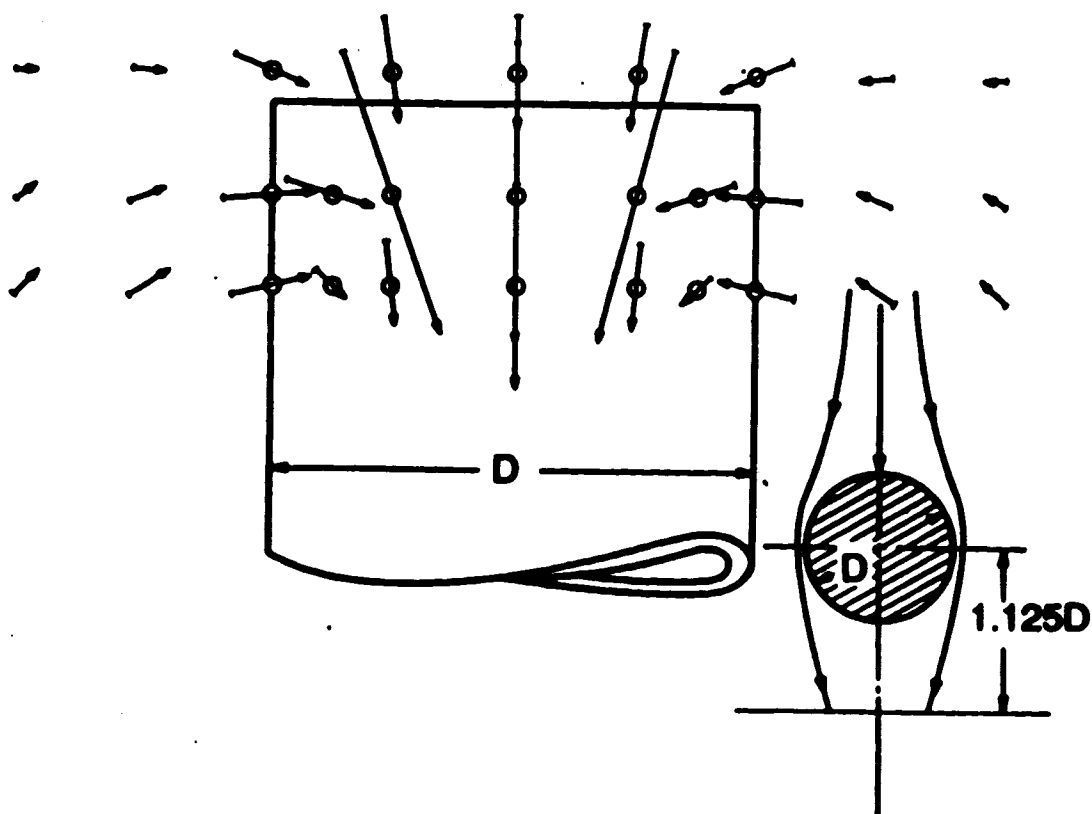


Figure 2-4: Velocity vectors in a crosswind plane of Sherlock and Stalker's stack suggesting the presence of a streamwise vortex pair.

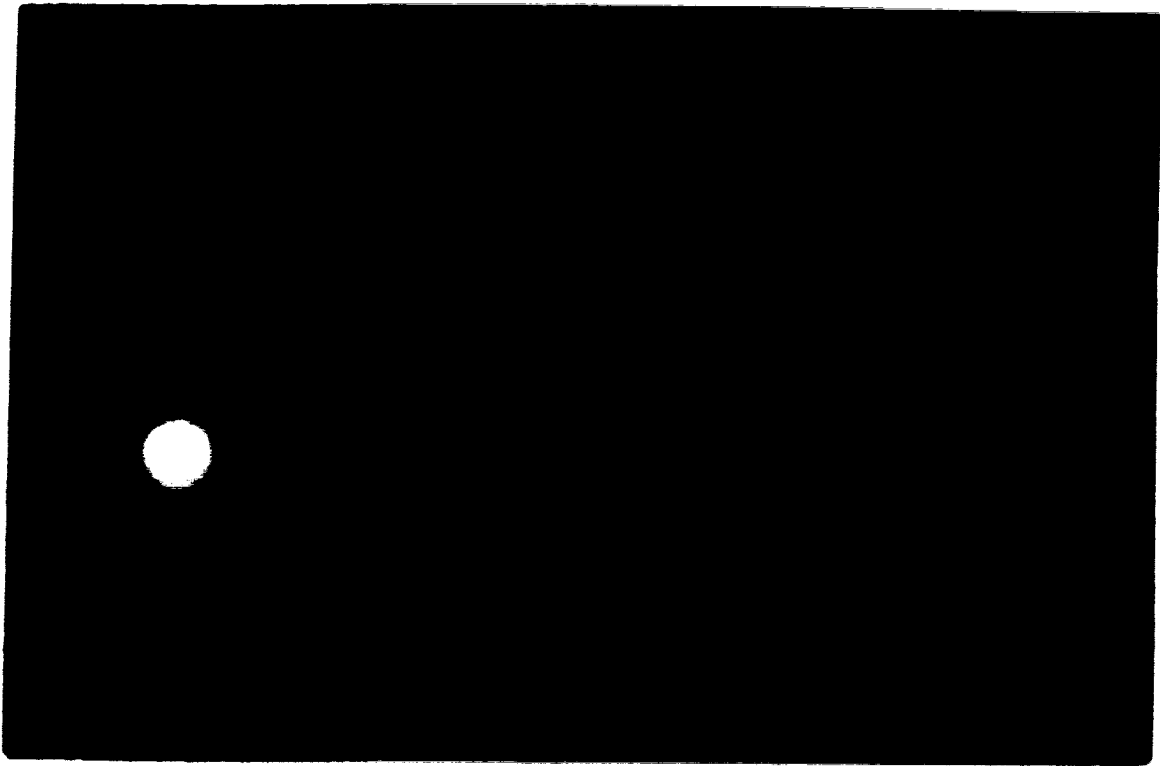


Plate 2-1: False coloured image of time averaged stack wake ($U_s t_{exp}/D = 1041$).

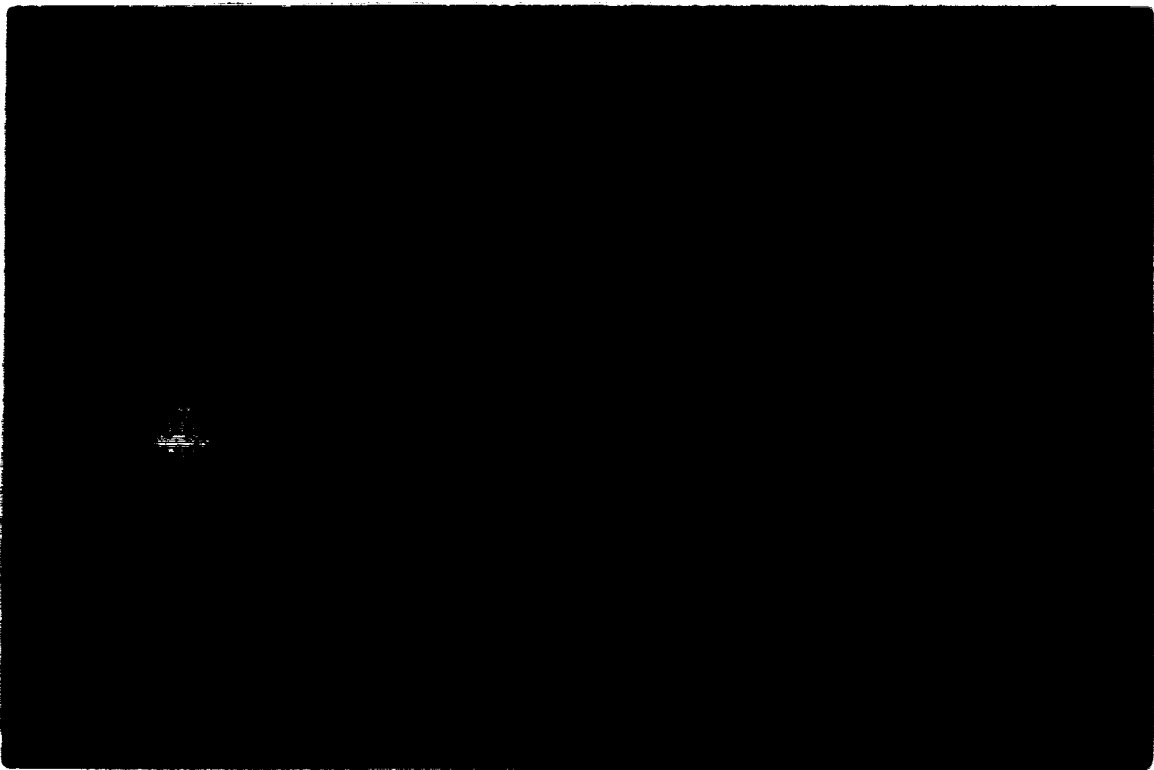


Plate 2-2: False coloured image of instantaneous (1/250 sec) wake showing the shedding of the von Kármán vortex street.

In Plate 2-2, the vortex street appears to follow the growth of the wake, providing some support for the vortex separation assumption. By assuming a vortex pair is embedded in the wake, an expression to correct plume rise for downwash was derived. However, to derive the downwash correction, two additional assumptions must be made.

- To produce a closed form solution for the downwash velocity, the angle of divergence of the wake is assumed to be small and is neglected in the derivation. Since the wake's angle of divergence is between 1° and 4°, this assumption is reasonable.
- The theory developed here assumes the circulation, Γ_d , of the vortex pair is constant with x . Each packet or leg of the von Karman vortex street will be of constant and equal circulation. Therefore, it follows that the cross linking vortices of the vortex street will have constant and equal circulation. Since the time averaged vortex pair would result from the streamwise component of the linking vortices, which have constant circulation, it is assumed that the time averaged streamwise line vortices will have constant circulation.

The circulation around a line vortex is defined as

$$\Gamma = \oint \vec{U}_t \cdot d\vec{s} \quad (2-18)$$

where U_t is the velocity tangent to the path defined by $d\vec{s}$, which is a closed contour enclosing the entire vortex. Considering one of the line vortices in the vortex pair, an equation for the velocity at any point away from a line vortex can be derived from the Biot-Savart Law. Batchelor (1967) derived this expression where

$$\vec{U} = -\frac{\Gamma_d}{4\pi} \oint \frac{\vec{r} \times d\vec{x}}{|\vec{r}|^3} \quad (2-19)$$

Figure 2-5 shows the parameters used in this equation. We can simplify Equation 2-19 by noting from Figure 2-5 that

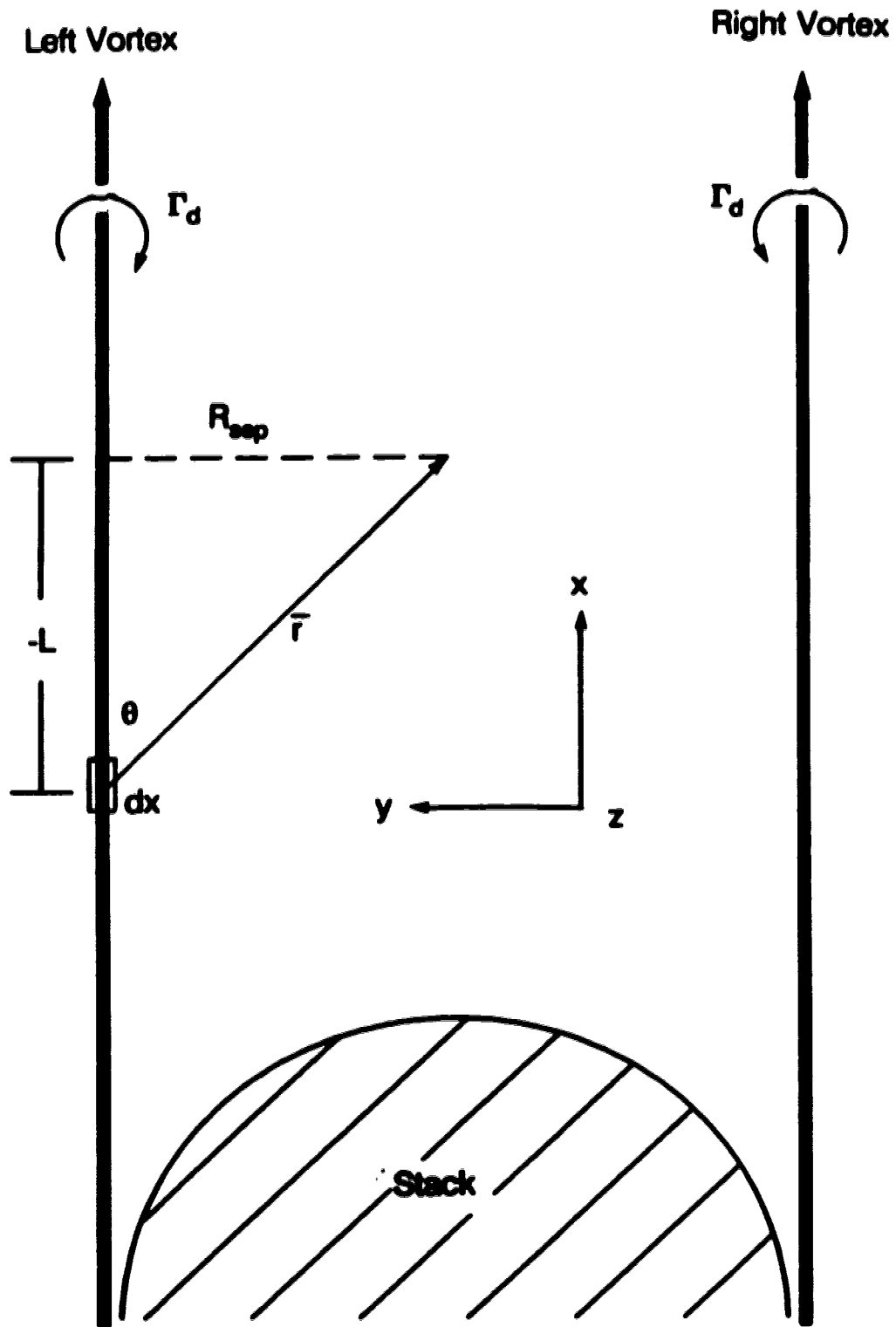


Figure 2-5: Schematic of variables used to calculate the velocity at a point due to the influence of a line vortex.

$$|\vec{r}| = \sqrt{R_{\text{sep}}^2 + L^2} \quad (2-20)$$

and by simplifying the cross product to

$$\begin{aligned} \vec{r} \times d\vec{x} &= |d\vec{x}| |\vec{r}| \sin\theta \\ &= (R_{\text{sep}}^2 + L^2)^{1/2} \frac{R_{\text{sep}}}{(R_{\text{sep}}^2 + L^2)^{1/2}} dx \\ &= R_{\text{sep}} dx \end{aligned} \quad (2-21)$$

Substituting Equation 2-20 and Equation 2-21 into Equation 2-19, noting the vortex velocity field will be perpendicular to the plane of the page and defining the induced downwash velocity w_d ,

$$w_d = \frac{-\Gamma_d}{4\pi} \int_{-\infty}^{\infty} \frac{R_{\text{sep}}}{(R_{\text{sep}}^2 + L^2)^{3/2}} dx \quad (2-22)$$

Here, the vortex velocity field due to the line vortex is determined at a distance R_{sep} from the line vortex. In Equation 2-22, R_{sep} is constant. Some confusion might occur from this assumption when considering the earlier statement that the separation of the vortex pair increases in the downstream direction. While R_{sep} is dependant on downstream distance, the derivation of the velocity field considers only the effects of the line vortex at one x position. Therefore, R_{sep} is constant in the integration of Equation 2-22. When the downstream dependence of R_{sep} is introduced, it allows the velocity at a variety of locations to be determined. The integration of Equation 2-22 can be easily carried out and yields

$$w_d = \frac{-\Gamma_d R_{\text{sep}}}{4\pi} \left(\frac{2}{R_{\text{sep}}^2} \right) \quad (2-23)$$

where R_{sep} can be any distance away from the line vortex. Simplifying Equation 2-23 and multiplying by 2 to include the contribution of both vortices in the pair produces

$$w_d = \frac{-\Gamma_d}{\pi R_{sep}} \quad (2-24)$$

In this derivation no information concerning the vortex core is needed other than to specify it must be enclosed in the area swept out by R_{sep} . In Chapter 4, it will be shown that this condition is satisfied.

An alternative view to this derivation of the downwash velocity is to assume the vortex pair is embedded in the plume. With the vortex pair embedded in the plume the downwash velocity would be a result of the self-induced velocity of the vortex pair. This downwash velocity can be found by considering Figure 2-6 and Equation 2-23. The distance separating the cores in Figure 2-6 is $2R_{sep}$. By substituting $2R_{sep}$ into Equation 2-23 for the separation distance, the self-induced velocity of the vortex pair is found to be

$$w_{d,s} = \frac{-\Gamma_d}{4\pi R_{sep}} \quad (2-25)$$

If the vortex pair was trapped in the plume, then the downwash velocity would be given by Equation 2-25. By comparing Equation 2-25 and Equation 2-24, we see that by assuming the vortex pair is embedded in the plume the downwash velocity becomes 1/4 of the velocity when the line vortices are outside the plume, everything else remains the same.

Continuing with the external vortex pair model, the separation of the streamwise vortex pair is set using self preserving wake theory. Changing separation is used to estimate how the downwash velocity will change in the downstream direction. From dimensional analysis we know the growth of a self-preserving wake is

$$\delta \propto x^2 \quad (2-26)$$

Assuming that the separation of the vortex pair is proportional to the growth of the wake, $R_{sep} \propto \delta \propto x^2$. Introducing a constant of proportionality, B_1 , and normalizing by the stack outside diameter D ,

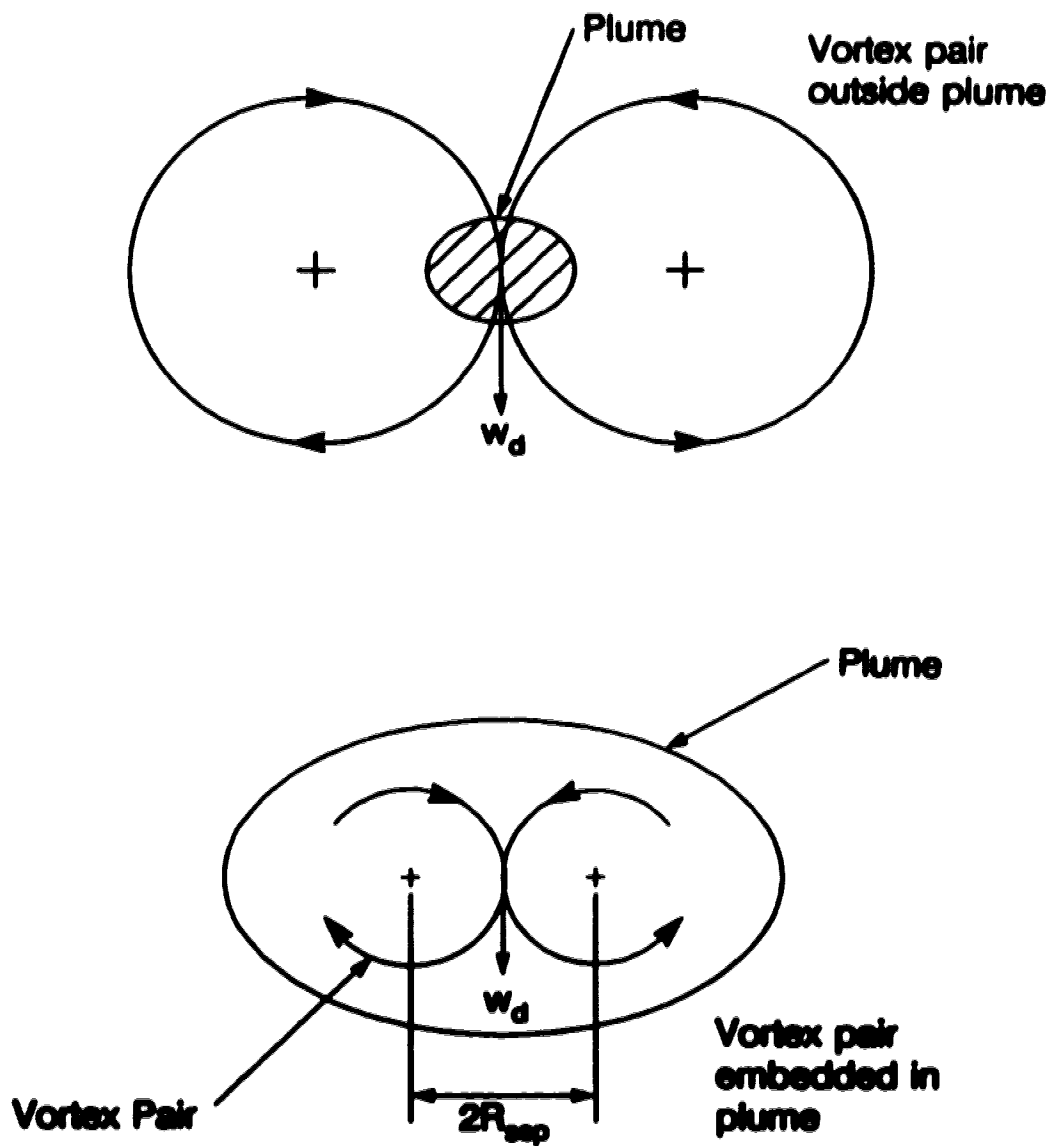


Figure 2-6: Schematic of the vortex pair outside the plume and the vortex pair imbedded in the plume.

$$\frac{R_{mp}}{D} = B_1 \left(\frac{x}{D} \right)^n \quad (2-27)$$

Substituting Equation 2-27 into Equation 2-24 produces

$$w_d = \frac{-\Gamma_d}{\pi B_1 \left(\frac{x}{D} \right)^n D} \quad (2-28)$$

as the effective downwash velocity produced by a pair of line vortices outside the plume. If the vortex pair was embedded in the plume, substituting Equation 2-27 into 2-25 would produce the effective downwash velocity

$$w_{d,e} = \frac{-\Gamma_d}{4 \pi B_1 \left(\frac{x}{D} \right)^n D} \quad (2-29)$$

The downwash velocity produces a downwash displacement on any fluid in the area of influence of the vorticity. Figure 2-7 shows how the vortex separation grows with the wake and how the downwash velocity would change with the distance downstream. The downwash velocity produces a displacement h_d , governed by

$$w_d = \frac{dh_d}{dt} \quad (2-30)$$

For the downwash velocity to be written in terms of a downwash displacement, another assumption must be made. It must be assumed that the downwash velocity does not affect the entrainment process, so Morton, Taylor and Turner's (1956) entrainment hypothesis, where entrainment is proportional to the plume vertical velocity, will have the same β . For Morton, Taylor and Turner's (1956) entrainment hypothesis to be unaffected, the vertical velocity of a plume with downwash must simply be the result of a superposition of the vertical velocity without downwash and the downwash velocity.

Substituting $dt = dx/U_p$, Equation 2-30 becomes

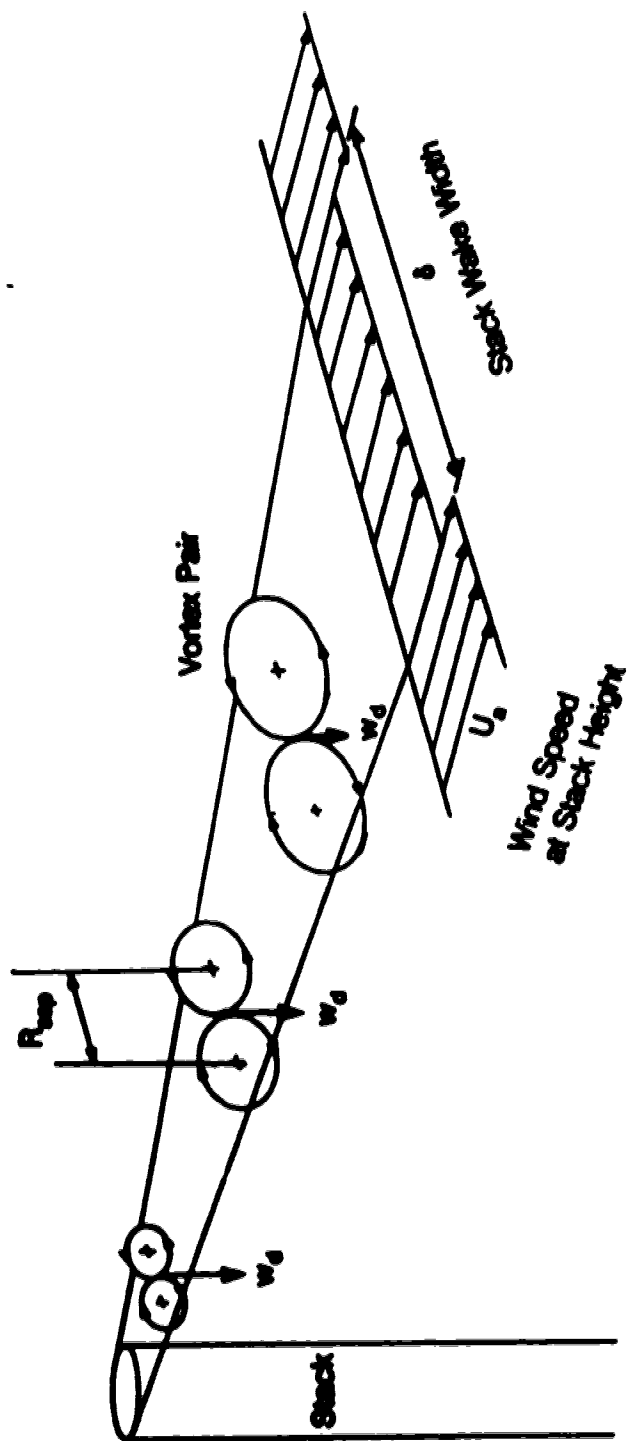


Figure 2-7: Downwash velocity model.

$$w_d = U_s \frac{dh_d}{dx} \quad (2-31)$$

Equating w_d in Equation 2-28 and Equation 2-31 and rearranging

$$\int \frac{-\Gamma_d}{\pi B_1 \left(\frac{x}{D}\right)^n D} dx = \int U_s dh_d \quad (2-32)$$

Integrating Equation 2-32 and assuming U_s is constant

$$h_d = \frac{-1}{1-n} \frac{\Gamma_d}{\pi U_s B_1} \left(\frac{x}{D}\right)^{1-n} + B_2 \quad (2-33)$$

If we evaluate Equation 2-33 at $x=0$, where $h_d=0$, then $B_2=0$. Integration in Equation 2-32 requires that B_2 is not a function of x , but it may be a function of M , D or other variables that are independent of downwind distance x . Making B_2 a function of M and D would allow a virtual origin displacement at the stack exit, like Equation 2-13, to account for stack gas entrainment into the recirculating wake immediately behind the stack. No virtual origin displacement will be used here, and $B_2 = 0$ will be assumed. Non-dimensionalizing Equation 2-33 by the stack diameter D produces,

$$\frac{h_d}{D} = \frac{-1}{1-n} \frac{\Gamma_d}{\pi D U_s} \left(\frac{x}{D}\right)^{1-n} \quad (2-34)$$

If Equation 2-29 were equated with Equation 2-31 and then integrated, the resulting non-dimensionalized downwash displacement for the case where the vortex pair is embedded in the plume would be

$$\frac{h_{d,e}}{D} = \frac{-1}{1-n} \frac{\Gamma_d}{4\pi D U_s} \left(\frac{x}{D}\right)^{1-n} \quad (2-35)$$

We can define

$$B_3 = \frac{\Gamma_d}{\pi U_\infty D(1-n)} \quad (2-36)$$

as a constant with x , for the case where the vortex pair is outside the plume. When the vortex pair is embedded in the plume the coefficient would be defined as

$$B_{3,e} = \frac{\Gamma_d}{4 \pi U_\infty D(1-n)} \quad (2-37)$$

The only difference between Equation 2-36 and Equation 2-37 is that $B_{3,e} = B_3/4$, the same factor introduced when the downwash velocities were compared. Later, the normalized circulation $\Gamma_d/U_\infty D$, will be expressed as an empirical function of the momentum ratio M .

We must now choose one of the two possible methods of modelling the downwash velocity, which are:

- the vortex pair lies outside the plume. Using this assumption the distance between the vortex cores increases with the wake's growth and is uncoupled from the growth of the plume (i.e. plume growth is independent of the vortex pair). This model will produce a closed form solution.
- the vortex pair is embedded in the plume. Using this method the growth of the vortex pair is directly dependent on the growth of the plume. This method would produce a coupled equation where the growth of the plume and the downwash velocity will be linked, requiring an iterative solution.

As a first iteration in this thesis, the vortex pair will be modelled outside the plume, producing a closed form solution.

Using B_3 , the external vortex pair downwash correction is then

$$\frac{h_d}{D} = -B_3 \left(\frac{x}{D} \right)^{1-n} \quad (2-38)$$

We now have an equation that predicts the amount of downwash a plume would

experience by the influence of the vortex pair. This makes the non-dimensionalized plume rise equation for a non-buoyant fully bent-over jet, accounting for downwash,

$$\frac{h_m}{D} = \left(\frac{3}{\beta^2} \frac{F_m}{D^2 U_s^2} \frac{x}{D} \right)^{1/3} - B_3 \left(\frac{x}{D} \right)^{1-n} \quad (2-39)$$

The value of the exponent $(1-n)$ is different for two-dimensional than for three-dimensional wakes. For example, n is 0.5 for a two-dimensional wake, according to Panton (1984), producing $(1-n) = 0.5$. A three-dimensional wake has $n = 0.33$, found in Batchelor (1967), producing a downwash correction exponent of $(1-n) = 0.67$.

2.4 Summary

In this chapter, the equations of plume rise and three models for downwash were presented. Several important considerations for both plume rise and downwash were discussed. The main points were:

- The entrainment coefficient is trajectory averaged to reduce errors due to simplifying assumptions used in the derivation of the plume rise equation.
- The virtual origin correction is an empirical correction reducing the rise of a plume by moving its origin down by h_v .
- The initial entrainment correction adds an extra entrainment at the stack exit, increasing the mass of plume. This correction will only produce slower rising plumes, while experimental data suggest some low momentum plumes will descend below the stack tip rather than rise.
- The downwash velocity correction is based on a vortex pair at the height of the stack tip which becomes embedded in the wake. The vortex pair creates a downwash velocity along the plume centerline, inducing a negative displacement of the plume. This correction is able to predict the negative rise indicated by the experimental data for some low exit momentum plumes.

Chapter 3

Laboratory Simulation Methods and Equipment

3.1 Introduction

The experimental methods and equipment used to simulate and measure the downwash of a plume will be discussed in this chapter. Methods for measuring wake velocity profiles and visualizing flow around a finite cylinder will also be discussed. Methods used to study the downwash of a plume were:

- Velocity profiles using Laser Doppler Anemometry (LDA).
- Full field concentration measurements using Planar Laser Induced Fluorescence (PLIF).
- Full Field flow visualization of flow around a finite cylinder using a newly developed technique of applying fluorescein dye directly on the stack surface.

Each of these techniques provided valuable data, such as plume centerline concentrations, wake growth rates and vortex structure. These data enabled the development of a downwash model.

3.2 Water Channel

All the experiments in this study were conducted in the Mechanical Engineering water channel. The water channel test section is 5000 mm long x 684 mm wide x 476 mm deep. A schematic of the water channel is shown in Figure 3-1. Two stainless steel tanks were situated on the ends of the test section. Using two 5 H.P. pumps, water was circulated from tank to tank through a 152 mm I.D. return pipe lying under the test section. The flow rate through the water channel was monitored using an orifice plate, placed in the return pipe, and a manometer. The 420 mm water level was controlled by a weir gate located at the end of the test section. Before it entered the test section, the flow was passed through two flow straighteners. The mean velocity and turbulence measurements, discussed in Chapter 5, were made using a Laser Doppler Anemometer.

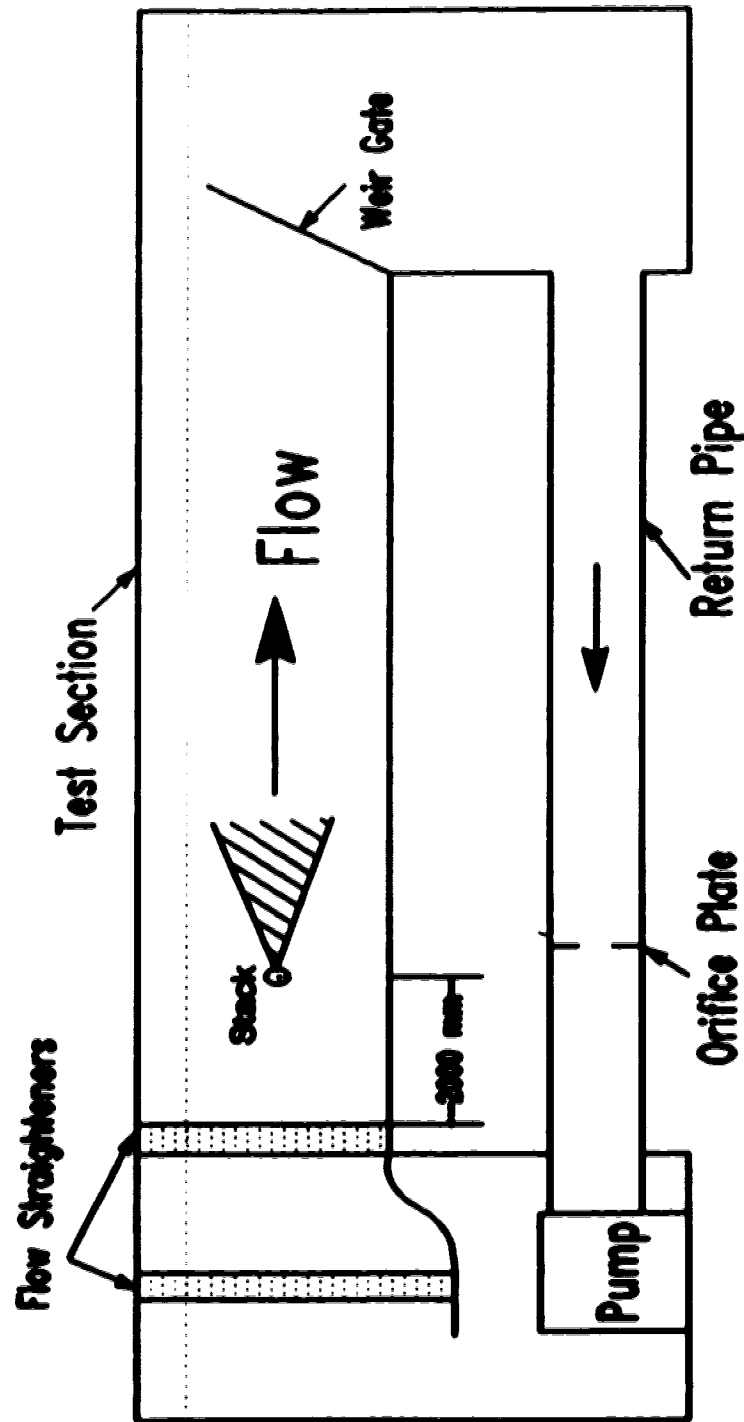


Figure 3-1: Water Channel.

3.3 Velocity Measurements

To collect velocity data a Laser Doppler Anemometer (LDA) and particle counter signal processor were used. The LDA consisted of two key components: the laser and the focusing/receiving optics. The laser used was an Ion Laser Technologies 300 mW argon-ion continuous wave laser. For these experiments the laser was run at a single wavelength of 514.5 nm (green). This reduced the maximum power to 100 mW, which was regulated to 75 mW to increase the life of the laser.

The focusing/receiving optics were manufactured by Thermo Systems Inc. (TSI) and consist of several components which included:

- **Beam splitter** - separated the single beam into two equal intensity beams.
- **Bragg cell** - shifted the frequency of one beam enabling the measuring of negative velocities.
- **Beam expander** - further separated the beams and made each beam thicker. Produced a smaller measuring volume when the beams were focused.
- **Focusing lens** - spherical lenses which focused the beams to a crossing point. Two lenses were used: a 571 mm focal length lens, so the entire width of the channel could be traversed and a 351 mm focal length lens, for its increased spatial resolution.
- **Receiving optics** - light scattered back from the measuring volume was focused onto a photomultiplier. The photomultiplier converted light intensity into voltage and sent the signal to a TSI 1980B signal processor. The signal processor then passed the information to a 386/33MHz PC.

The laser and optics assembly were mounted on computer controlled three axis traverse. To seed the flow, 25 mL of a 2 g/L mixture of Titanium dioxide (TiO_2) was used. This amount of seeding would be sufficient to keep the flow properly seeded for 7 to 10 days. The data collected in the water channel flow were 50 second averages, at approximately 250 randomly spaced data points per second. The velocity data of the stack exit flow used 30 second averages, also at approximately 250 samples per second. The software used to analyse the data was written by B.W. Zelt,

and is described in detail in Zelt (1991).

3.4 Concentration Measurements

Concentration measurements were made using Planar Laser Induced Fluorescence (PLIF). In the present experiment, disodium fluorescein was illuminated using a laser light sheet. A video image was taken of the dye, and the concentration of the dye determined from its intensity.

The PLIF system used was similar to the one developed by Campbell (1991). The present study was performed in the water channel rather than Campbell's towing tank, so the apparatus and procedures were refined for that environment. The laser used was a Coherent Innova 70, 4 watt argon-ion continuous wave laser run in multi wavelength mode, producing light at wavelengths of 488 nm and 514.5 nm (blue-green). The beam was split using a 50/50 dielectric mirror beam splitter, shown in Plate 3-1. These beams were then passed through 20x microscope objectives to make their diameter smaller than the 50 μ m core diameter fiber optic cable. The fiber optic cable was run to two optics stands which held the optics necessary to produce a light sheet.

Plate 3-2 is a picture of the optics used to produce a laser light sheet. The beams emerged from the fiber optic cable as an expanding cone. To produce a narrow light sheet, the emerging light first required refocusing into a narrow light beam. The light from the fiber optic cable was collimated using a 20x microscope objective and 100 mm and 300 mm focal length spherical lenses. The microscope objective was positioned directly in front of the fiber optic cable. The 100 mm and 300 mm focal length spherical lenses were 5 mm and 400 mm from the microscope objective respectively. A 10 mm focal length cylindrical lens, 15 mm from the 300 mm lens, spread the laser beam to produce an expanding laser sheet.

The laser light sheet had a minimum thickness of approximately 1.5 mm increasing to about 3 mm at ± 500 mm from the minimum. The distribution of light intensity across the light sheet was gaussian. The gaussian intensity profile made the center brighter than the edges of the light sheet. The overall power transmission efficiency from laser output shutter to light sheet, of this system was approximately 60%-65%.

The optics stands were placed as shown in Figure 3-2. The test section was lit from both sides in order to produce a more uniform light distribution and avoid problems of light sheet attenuation.



Plate 3-1: Laser and splitting optics used in PLIF.



Plate 3-2: Optics stand and Optics used to produce a laser sheet.

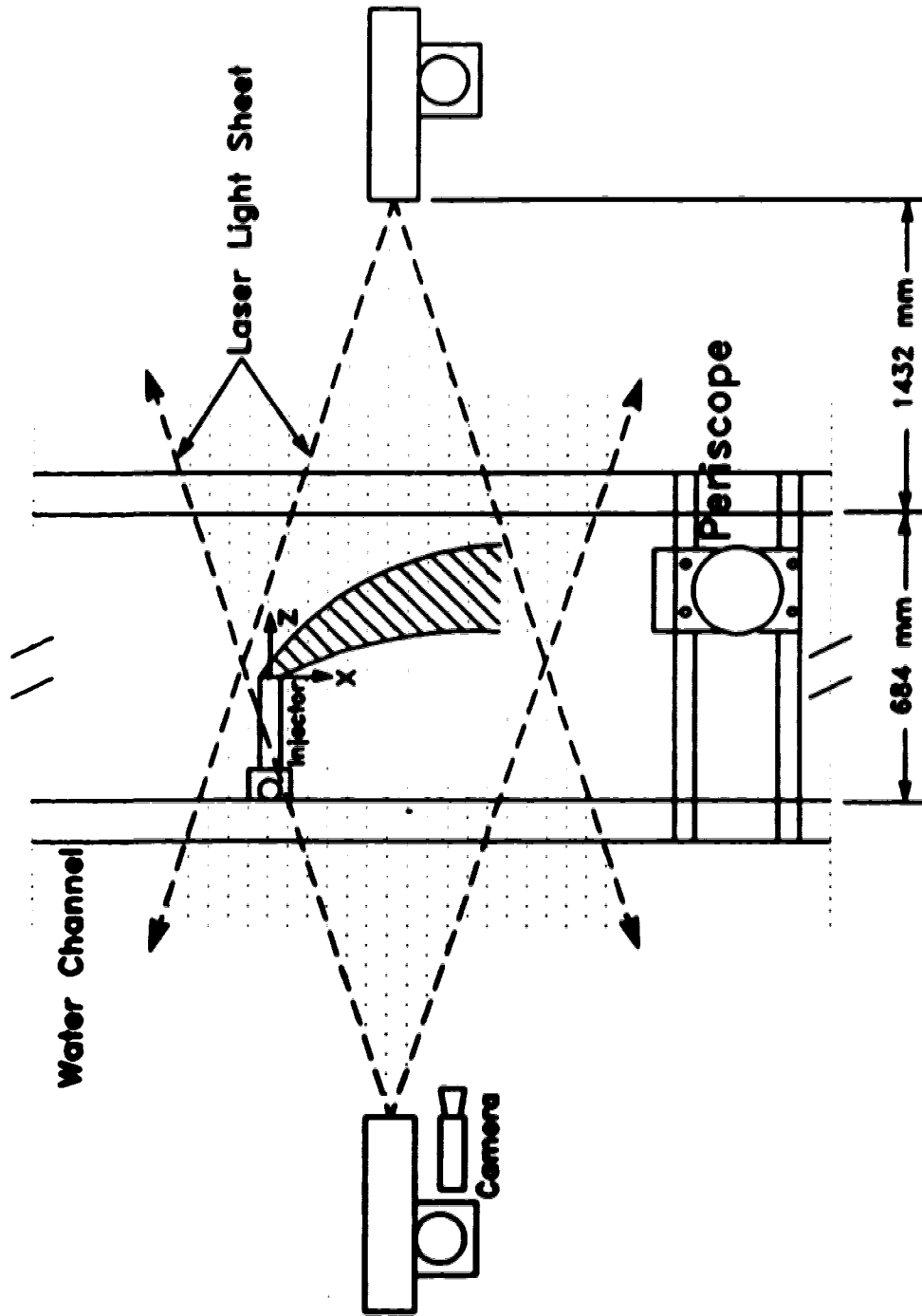


Figure 3-2: Positions of light stands, injector and camera relative to the water channel, viewed from above

3.4.1 Behaviour of Disodium Fluorescein Tracer Dye

When stimulated with the argon-ion laser, disodium fluorescein emits light at wavelengths ranging from 530 nm to 580 nm, with peak output at 550 nm. The laser light was at 488 and 514.5 nm. The difference in wavelength between the laser light and the fluorescing dye allowed the laser light to be removed using filters. No filters were used in this thesis because it was found that by using appropriate intensity thresholds, the laser light could be removed. As Walker (1987) described, the intensity of the light emitted by fluorescent dye depends on several factors. These factors include:

- dye concentration
- laser sheet light intensity
- pH of the solution
- dye temperature

If light sheet intensity, pH and temperature were constant, dye concentration would be directly proportional to dye intensity. Unfortunately, the light sheet intensity has a gaussian variation, but pH and temperature of the dye are easily controlled.

It was found by Walker (1987) that disodium fluorescein emission intensity will drop as pH of the dye falls below 8.0. At a pH above 8.0, intensity of the dye remains constant. A buffering solution consisting of ammonium hydroxide and ammonium chloride was formulated by calculating the amounts of each required to keep the pH of the water channel and dye at 9.0. Using a pH meter, the pH of the dye and water channel was measured to be within 5% of 9.0 after 30 minutes. The buffer was added to the water channel to ensure the pH of the dye did not change when the dye and ambient fluids mixed.

Walker (1987) also investigated the effects of temperature change on fluorescence of disodium fluorescein and found a 0.6%/°C change in fluorescence intensity occurred. To minimize this effect, the water channel and dye were allowed to reach a constant temperature of $18^{\circ}\text{C} \pm 2^{\circ}\text{C}$. It was assumed the temperature for each run was constant. Any temperature variations which occurred from run to run were removed by normalizing the concentration in each run by the known injection

dye concentration.

3.4.2 Image Processing Equipment

Image processing required the following steps:

- collection using video tape to allow expanded-time playback
- digitizing from video tape and averaging of digitized images
- correction for background, lightsheet non-uniformity and system non-linearity
- analyses to determine concentration profiles and plume centroids

Collection using video tape:

The experiments were recorded on video tape to maximize the amount of data acquisition possible since the image processing system was not able to work in real time. Saving the images on video tape permitted playback at a slower rate so each image could be digitized. Using video tape to record data also made both individual and time averaged images easily available. The North American standard for video signal is NTSC or composite video. Under this standard both color and intensity information is contained in one signal. An adaptation of this standard is Super VHS (S-VHS) where intensity and color information is transferred separately. In this study, only intensity information was used in determining concentrations, so S-VHS was used. The separate intensity signal should produce a better image than could be obtained using composite video. The camera used in this study was a Sony DXC-151 S-VHS/RGB color video camera. It had an Interline-transfer CCD (Charge Coupled Device) having 768 horizontal x 493 vertical picture element resolution.

The camera also had an electronic shutter feature with shutter speeds ranging from 1/30th of a second to 1/10000th of a second. For these experiments the shutter speed was set at 1/250th of a second instead of the NTSC standard 1/30th of a second. The faster shutter speed was used for greater spatial resolution for each pixel in the images. With the shutter speed set at 1/30th of a second a particle in the flow would move approximately 5 pixels or 3.3 mm in one frame. With the shutter speed set at 1/250th of a second, the resolution of the same particle was 1 pixel or less than 1 mm for a frame.

Using the electronic shutter created an interesting problem for individual images. An entire frame was scanned as two distinct fields. In the first $1/60^{\text{th}}$ of a second, the even lines of the frame were scanned and in the second $1/60^{\text{th}}$ of a second the odd lines of the frame were scanned. When the shutter speed was $1/30^{\text{th}}$ of a second, there was no time between fields, as shown in Figure 3-3. When the shutter speed was increased, there was a gap between the two fields, also shown in Figure 3-3. At the faster shutter speed the two fields were still $1/60^{\text{th}}$ of a second apart, but the shutter was only open for a fraction of the $1/60^{\text{th}}$ of a second. The problem in using the electronic shutter was that during the time shift between the scanning of each field the image changes. However, the two fields were still required to make up a single image.

An experiment was done to test the significance of the electronic shutter irregularity. A pendulum was video taped swinging and the resulting images analyzed. At a shutter speed of $1/250^{\text{th}}$ of a second, the difference between the two fields was found to be significant for instantaneous images but was inconsequential for the 50 second time averages used in the downwash study.

The S-VHS signal was recorded on a JVC editing VCR. Figure 3-4 is a schematic of the images collection process showing the processing order and the type of signal used at each step.

Digitizing from video tape:

To digitize images from the VCR, a conversion from S-VHS to RGB was necessary. To do this, a NEC SVC-10, S-VHS to RGB decoder was used. An RGB signal was fed into the image processing system after conversion from S-VHS, as seen in Figure 3-4. The image processing system consists of three Data Translation image processing boards, taking RGB or NTSC as an input. These boards were housed in a 486-66MHz personal computer. The three boards were: a frame grabber, an auxiliary frame processor and a composite to RGB converter, as shown in Figure 3-4.

The frame grabber used was a Data Translation model DT2871. It was capable of digitizing a standard RGB television signal, converting to HSI (Hue, Saturation and Intensity) for processing and back to RGB. The images in this study were used in the HSI format for extracting concentration information from the intensity array. The digital output image has a spatial resolution of 512×512 pixels (picture elements). The video signal uses only 480 of the horizontal lines, with the last 32 horizontal lines unused. The information for each image is stored in

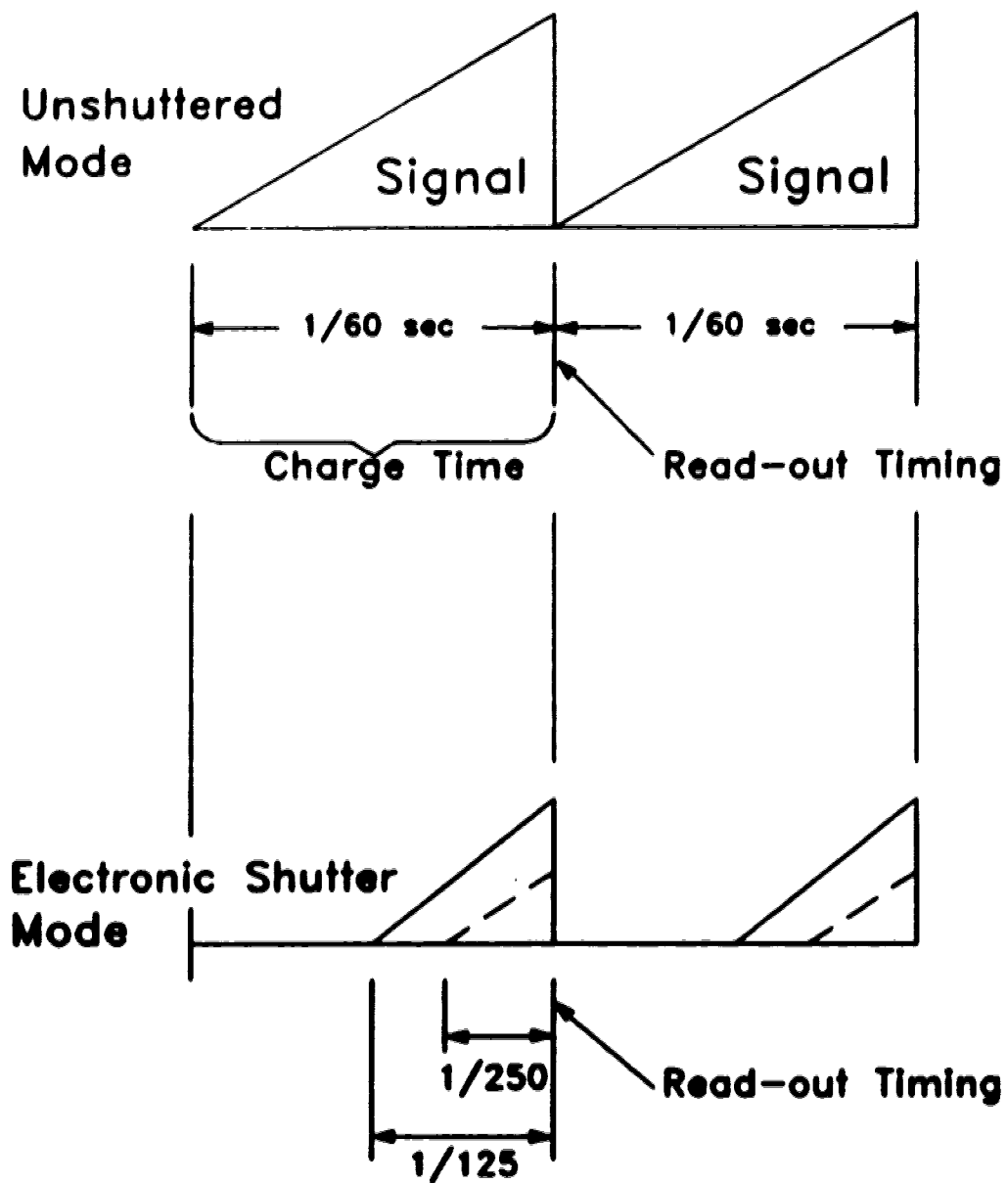


Figure 3-3: Video camera electronic shutter operation.

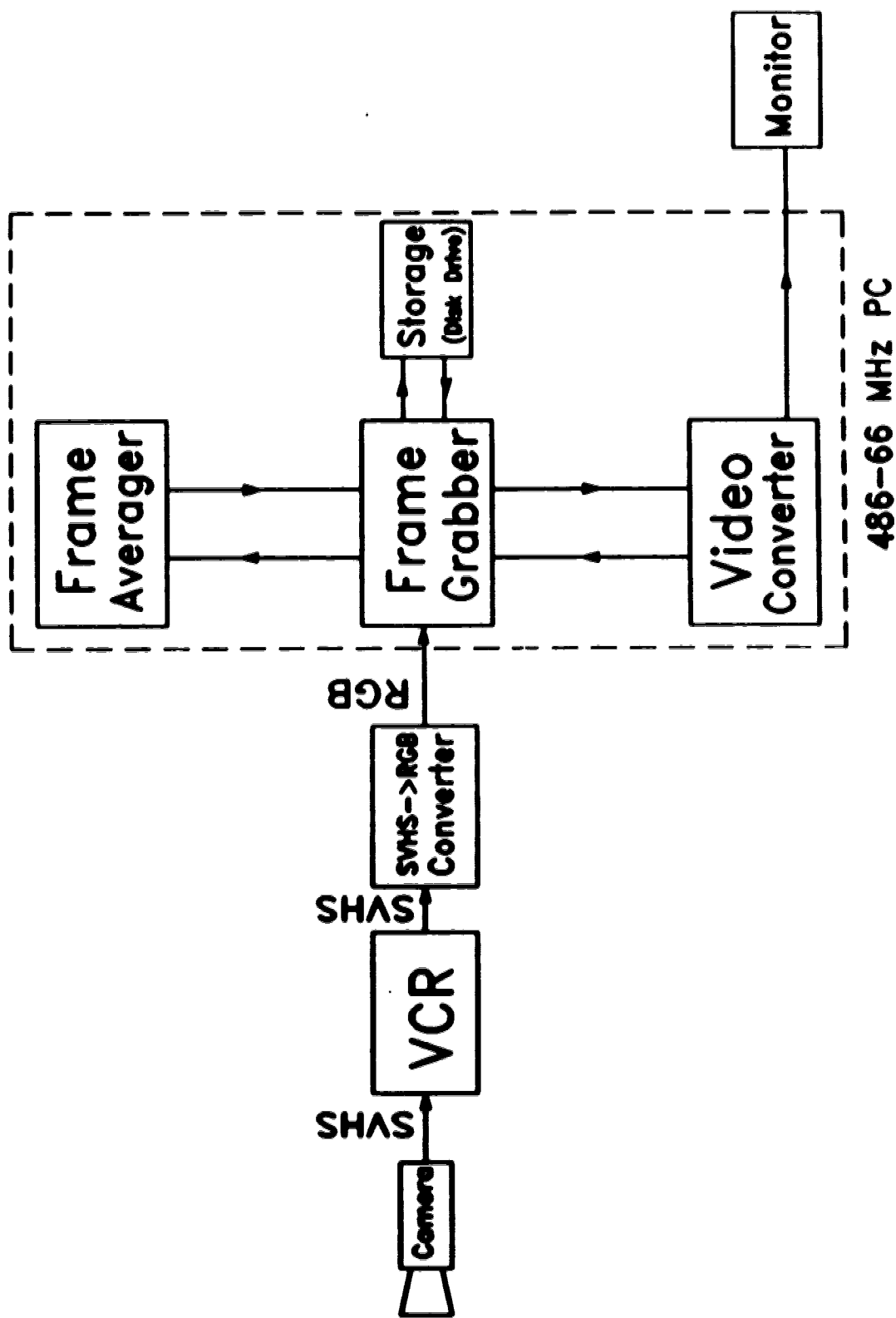


Figure 3-4: Schematic diagram of image acquisition and processing system.

three buffers, one for each of the red, green and blue signals or the hue, saturation and intensity signals. Each of the pixels stored for the three buffers uses 8 bits. This corresponds to 256 different levels (including zero) for each pixel. After the images were stored, they were transferred from the frame grabber to disk, as illustrated in Figure 3-4.

The frame averager was a Data Translation model DT2858 auxiliary frame processor. This was used to perform high speed mathematical operations on one of the three frame buffers. The operation that it performed for this study was the online averaging of video images. Unfortunately, the DT2858 could not average in real time and was limited to averaging a maximum of 10 frames per second. It produced the same spatial resolution (512 x 512 pixels) as the frame grabber, but each pixel was stored with 16 bits of memory, allowing it to average a minimum of 256 frames before overflowing.

The video converter was a Data Translation model DT2869 real time video conversion board. The video converter allowed digital images to be displayed using a standard composite monitor.

Correction for various image anomalies:

The correction and analysis of images was done independently of the image acquisition system. The first step in image correction was to remove the background concentration accumulated during image collection. As described earlier, dye released into the water channel was recirculated, increasing the background fluorescence. To produce a clear plume image, this background intensity had to be removed. A time average of approximately 60 images was taken of the background at the end of each run. The background time average was then subtracted from the time averaged plume image, removing the background fluorescence. The pixel intensity of the background time average ranged from 5 to 7, compared to the injection dye intensity, I_0 , of 200.

Two alternate methods of removing the background were also tested: subtracting the background intensity from the individual images, then averaging, and a time weighted background intensity. Both of these methods were compared to the method used in this thesis, but did not produce noticeably different results.

The second step in image correction was adjustment for the laser light sheet non-uniformity. As described earlier, the intensity of the dye depended on four key factors. Dye temperature and pH were controlled during the experiment, but

correcting for varying laser sheet light intensity was done after collection.

If the light sheet intensity had been constant in space, with pH and temperature controlled, the concentration of the dye would have been directly proportional to the dye fluorescence intensity. The light sheet intensity was not constant, varying with a gaussian intensity distribution across the sheet in the transverse direction. Also, the intensity of a light sheet is reduced as the sheet expands radially away from the source. Using two light sheets reduces these non-uniformities but does not eliminate them. By combining two light sheets, on opposite sides of the test section the radial decrease in intensity was reduced to 10%.

Using two light sheets also reduces the effects of attenuation by dye absorption. The higher the concentration of dye, the greater the light sheet attenuation. For a typical experiment conducted in this study the theoretical maximum attenuation was only 2% using two light sheets, as compared to 11% using one sheet and were confirmed experimentally. The equation needed to determine the theoretical attenuation are found in Campbell (1991). Since two sheets were used for all experiments, the effects of attenuation were neglected.

To eliminate the effects of changing intensity of the light sheet, a digital intensity map of the light sheet was made and used to remove the variations. The map was an image of the light sheet illuminating a background of a known concentration of dilute disodium fluorescein (1×10^{-7} mol/L). Since the concentration of fluorescein was known and constant any variation in the measured intensities would be due to the changes in intensity of the light sheet. The concentration C_{ref} produced a corresponding intensity I_{ref} . The light sheet image was median spatially filtered using 3×3 pixel arrays to remove any small variations in the intensity of the light sheet image due to electronic noise or air bubbles in the water. A plume image was corrected by dividing the intensity of each pixel in the plume image by the intensity of the corresponding pixel in the light sheet intensity map. The pixels in the image were then referenced to the same known intensity, I_{ref} , removing variations in intensity due to light sheet non-uniformity. The changes in light sheet intensity were found to be less than 5% of the maximum intensity. The basis for this correction can be found in Campbell (1991).

The next step was to normalize the intensity of the plume image. To provide a value to use in normalizing the intensities, a bottle of the injection solution, placed at the stack exit, was video taped before each run. This image was used to determine the intensity, I_0 , of the initial injection concentration, C_0 , to use in the normalization.

An experiment was conducted in which a bottle containing disodium fluorescein was immersed in a tank of water with the same dye concentration as the water in the bottle. The image was digitized and it was found the bottle had no effect on the measured intensity of the dye if the measurement was taken more than 1 cm from the edge of the bottle. The normalization image was also divided by the light sheet intensity map to remove any intensity variations.

The intensity of the injection concentration was averaged over 100 pixels (10 x 10) in the center of the bottle. This number of pixels was determined by a trial and error process, and was found to produce the most repeatable results. The intensity, I_o , varied only $\pm 3\%$ between all runs performed. Any larger or smaller number of pixels produced too much deviation in I_o from run to run. The intensity of each pixel in the plume image was normalized by the averaged intensity produced by the injection concentration. Since both the plume intensity and the injection intensity were referenced to I_{ref} when the light sheet intensity variations were removed, normalizing the plume intensities by I_o eliminated any dependence on I_{ref} . Consequently, I_{ref} does not appear in any equations and the value of C_{ref} does not need to be known, as shown in Equation 3-1.

$$\frac{I/I_{ref}}{I_o/I_{ref}} = \frac{I}{I_o} \quad (3-1)$$

The intensities ranged from 0 to 1 after being normalized by the injection concentration.

A correction for system non-linearity was made which converted the measured intensities into concentrations. The image processing system was calibrated using 10 different concentrations of disodium fluorescein, ranging from 1×10^{-6} mol/L, the injection concentration, to 3.125×10^{-9} mol/L. The response of the system was measured and a calibration curve plotted, shown in Figure 3-5. The equation that was chosen to fit the calibration was

$$\frac{C}{C_o} = 0.0185 \exp\left(4.0 \frac{I}{I_o}\right) - 0.0185 \left(\frac{1}{\frac{I}{I_o} + 1} \right) \quad (3-2)$$

This calibration was performed on two separate occasions several months apart and

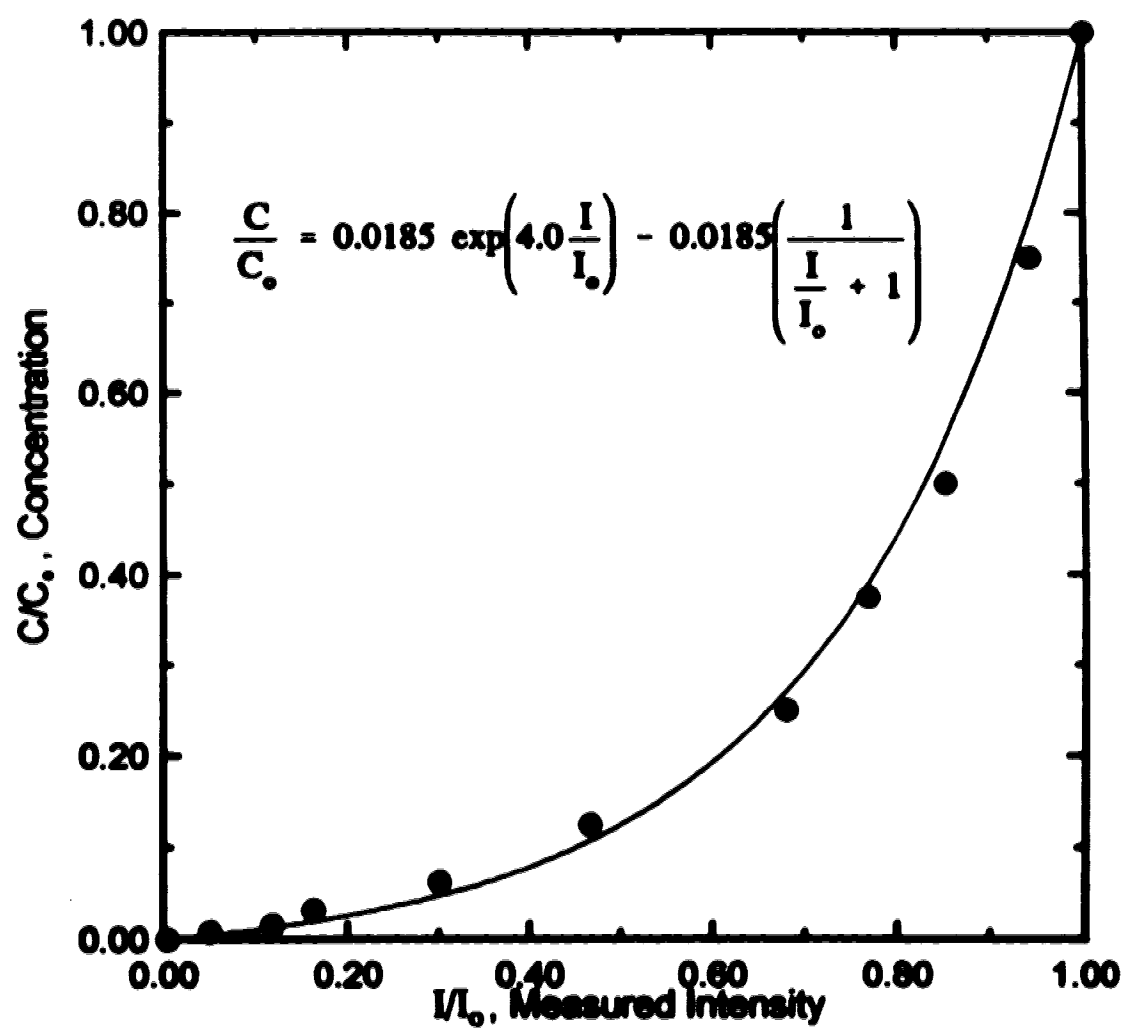


Figure 3-5: Non-linear concentration correction of the complete image processing system.

the results agreed within $\pm 2\%$. The concentration correction was applied to each pixel to account for any non-linear response in the system and to convert the intensities to concentrations. The plume image was then in terms of concentration, from 0 to 1, normalized by the injection concentration of 1×10^{-6} mol/L.

Small errors in concentration contours could be introduced through the subtraction of the background intensity before conversion to concentrations. When the background intensity is subtracted from the plume images, the intensity of the entire image is reduced. Since ambient fluid is entrained as the plume moves downstream, very little ambient fluid has reached the plume centerline near the stack exit. Therefore, when the background is subtracted near the stack the actual intensity of the plume is changed. For example, if the plume intensity on the centerline was 180 and a background of 5 was subtracted, the apparent normalized intensity would be 0.875, while the actual normalized intensity would be 0.90. The error in concentration, from Figure 3-5, would be about 10%. As the normalized intensity moves towards $I/I_0 = 0$, Figure 3-5 suggests the same change in intensity will produce an increasing error in concentration. Fortunately, the error introduced by subtraction of the background intensity produced no effect on the measured centroids of the plume. Different methods of removing the background concentration should be considered in future work.

Analysis of plume images:

Samples of the time averaged, fully corrected image can be seen in Plate 3-3. False colored images are shown for momentum ratios of $M = 0.25, 1.5, 3.0, 8.0$. The different colors represent different ranges of concentration starting at $C/C_0 = 1.0$ (the white area) stepping down in intervals of $C/C_0 = 0.0625$ to zero. The thresholds of concentration for each color can be altered, allowing the display of different combinations of concentration. Using several specially written programs, these images are used to determine the trajectory and the concentration profiles of the plumes.

3.5 Flow Visualization by Surface Application of Fluorescein

A major aspect of this study was to visualize the flow around the end of a finite cylinder to determine the structure of the shed vortices. Sherlock and Stalker (1941) reported a vortex pair could be found at the tip of a stack and suggested it was shed from the stack tip. The flow around infinite or semi-infinite cylinders has been

Plate 3-3: False colored, time averaged images for $M = 0.25, 1.5, 3.0$ and 8.0 .

studied but very little has been reported on the structure of flow around the tip of a finite cylinder. To ascertain the structure of vorticity shed off a finite cylinder a method of visualizing the vorticity as it was shed off of the stack was needed.

In a study done by Bays-Muchmore and Ahmed (1992), the vortex shedding from an infinite cylinder was studied by painting the cylinder with fluorescein dissolved in a corn starch and water mixture. They were able to visualize the flow for less than a minute before the fluorescein mixture would flake off the cylinder. Williamson (1989) conducted another study of the modes of vortex shedding off an infinite cylinder by painting fluorescein onto the cylinder. His method of applying the fluorescein was not given.

Several methods of applying fluorescein onto the cylinder surface were considered for this study. The first was to duplicate the method of Bays-Muchmore and Ahmed (1992). This method did not work well, as very little fluorescein could be deposited on the cylinder. Several other binders, such as latex paint and corn syrup, were tried but none were effective. A new method was suggested by a colleague (Bill Peck); the fluorescein would be suspended in an insoluble varnish applied to the cylinder. The flow would then dissolve the dye particles exposed on the surface. This method of applying the dye to the stack sounds impractical but works effectively. First, 1.5 g of disodium fluorescein was mixed with 10 mL of butyrate dope. Butyrate dope is a clear, viscous fluid that is used to add strength to fabric covered model airplanes. The dope was thinned using 15 mL of thinner or acetone. The thinned dope did not dissolve the fluorescein but held it in suspension. This mixture was slightly more viscous than water. It was applied to the cylinder using a Paasche single action air brush, shown in Plate 3-4, with 15 psig air pressure. To cover a 1 cm diameter cylinder 25 cm long, 10 mL to 15 mL of the fluorescein mixture was needed. Once the fluorescein-dope mixture was applied it required 10 to 15 minutes to dry. A light sanding using 600 grit sand paper was performed on the dry surface to expose fluorescein particles in suspension. The amount of time dye was visible during an experiment was between 45 and 60 minutes, depending on the concentration of fluorescein on the stack. It was necessary to occasionally re-sand the surface to expose more fluorescein particles.

The fluorescein dissolved into the water was illuminated using a modification of the light sheet described in Section 3.4. The 300 mm spherical lens was moved 25 cm back from the cylindrical lens. This created a light sheet that was 3 cm thick. The dye from the cylinder was also visualized using a Xenon strobe but the laser



Plate 3-4. Painting stack with fluorescein for flow visualization.

sheet allowed greater detail to be seen in the vortex structure. The results of these experiments will be discussed in Chapter 4.

3.6 Stack Orientation

Normally, a stack would be orientated vertically to include the effects of buoyancy, but in this experiment the effects of buoyancy were not studied. The orientation of the stack in the water channel was also not limited by the presence of a shear layer since the approach flow had uniform mean velocity. Since the water channel has a glass bottom the easiest orientation of the stack, relative to the camera, was to place the stack perpendicular to the side wall and view the stack from below the water channel. Figure 3-6 is a schematic showing the stack position and equipment used for injecting the dyed water. The dashed lines represent the planes in which the light sheets were oriented. The disodium fluorescein was mixed in a 20 L container and transferred into the 60 L pressure vessel shown. The vessel was pressurized by compressed air which was regulated to 10 psig. The dye then passed through a needle valve used for fine flow control and a solenoid shut-off valve. A rotameter was used to measure the flow rate. The dye passed into the stack and was injected into the flow.

Figure 3-6 shows the orientation of the y and z axis of the model with the origin at the center of the stack tip. The x axis for the model was in the downstream direction. To determine any distance from the origin in the model two points needed to be marked. The zero position (center of the stack tip) of the model and a point 70 mm away from the zero were located using a positioning template. Using these two points all other model coordinates could be determined. Using this method the resolution was approximately 0.88 mm per pixel element and was accurate to within $\pm 2\%$. The largest distance measured was approximately 280 mm.

3.7 Viewing Plume Cross Sections

The two sections of the plume used in the study of downwash are labelled in Figure 3-7 as sections A-A and B-B. With the laser sheets orientated horizontally, section A-A was illuminated. To view section A-A, the video camera was located beside the left optics stand, as Figure 3-2 indicates. The plume image could be seen in the bottom viewing mirror located underneath the water channel, shown in Figure 3-7. The mirror, which is 760 mm long, is mounted on a frame angled at 45° . The other plume section examined is shown by section B-B. To view this cross sectional

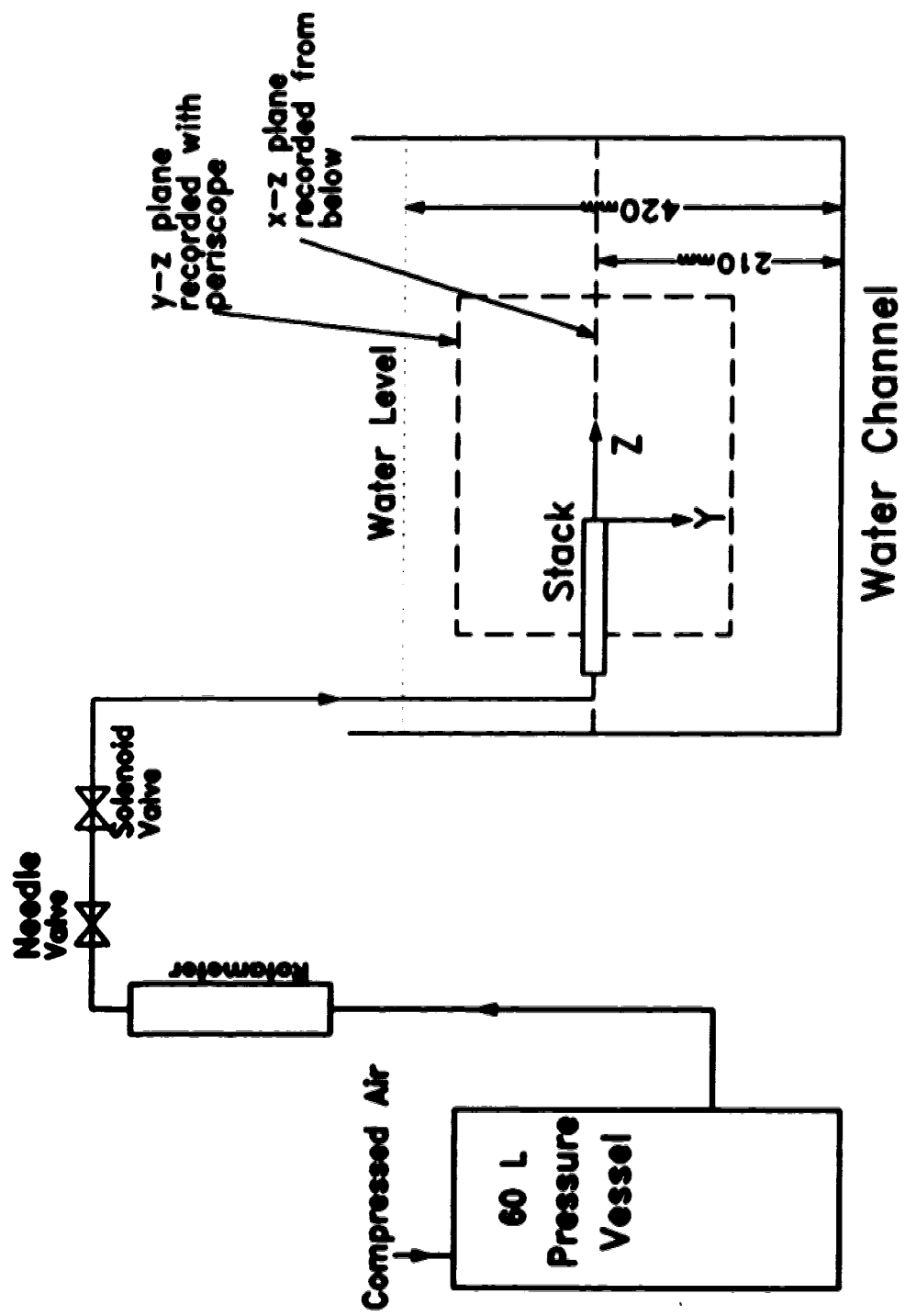


Figure 3-6: Schematic of dye injection apparatus and stack position looking upstream (periscope view).

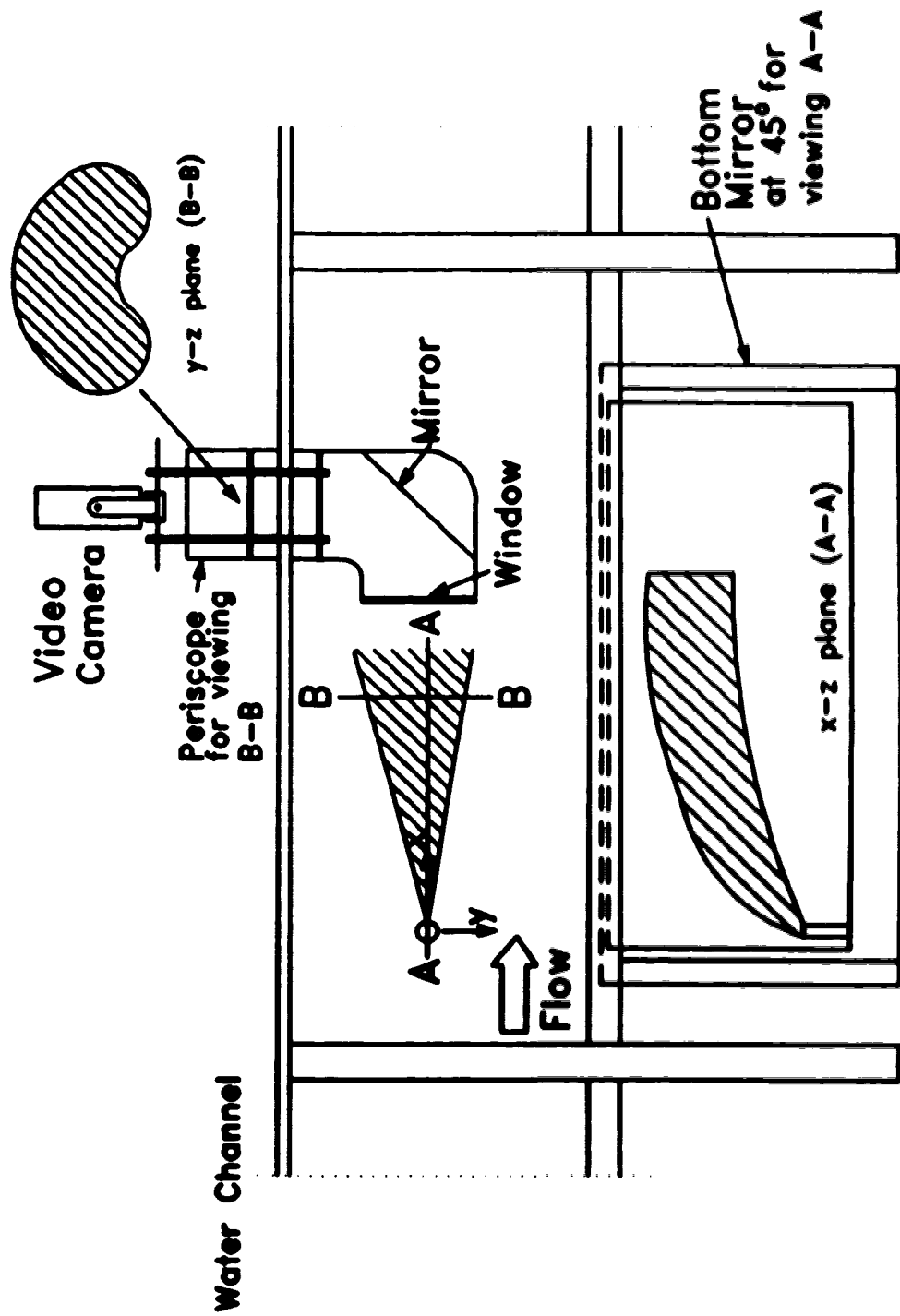


Figure 3-7: Illustration of the orientations used for viewing two plume sections.

view of the plume, a periscope was constructed. The periscope was fabricated out of 12" PVC pipe. A mirror was placed inside the elbow at 45° and the opening facing upstream was sealed using a piece of glass and silicone sealant. A piece of straight tubing was attached above the elbow and mounting brackets and camera mounts were fastened to the extension. The mounting brackets attached to a frame secured to the water channel railing. The camera was attached to a bracket at the top of the periscope.

To change from a center-line to a cross-section image, the optics stands did not need to be moved. The only adjustment required was a rotation of the cylindrical lens from horizontal to vertical, making re-alignment of the optics unnecessary when the laser sheet orientation was changed. To obtain cross-sections at various downstream locations the stack was moved, rather than moving the laser optics. The stack could be moved since the turbulence intensity and the mean velocity did not change over the range of stack positions studied.

3.8 Summary

Three experimental methods, and the equipment required in each, were described in this chapter. The main areas discussed were:

- A Laser Doppler Anemometer, consisting of a ILT 300 mW laser and TSI focusing/receiving optics, was used to collect velocity data for the ambient flow, stack flow and wake flow.
- Planar Laser Induced Fluorescence (PLIF) was used to collect full field concentration measurements of plumes.
- The fluorescence of disodium fluorescein was dependant on dye temperature, dye pH, dye concentration and laser light sheet intensity.
- Dye pH and temperature were constant during an experiment but the laser light sheet intensity had a gaussian intensity distribution in the axial direction of the light sheet.
- Light sheet intensity was normalized using a measured map of the light sheet intensity. The map was an image of the light sheet illuminating a

dilute, constant concentration background of disodium fluorescein.

- Using a pair of opposing light sheets the effects of attenuation could be neglected.
- Flow visualization of the vortex street shed off a finite cylinder was done by painting disodium fluorescein , suspended in butyrate dope, onto the stack model.
- Two views of the plume were used in studying downwash. A plume centerline profile using a horizontal light sheet, was viewed through a mirror, angled at 45° , underneath the water channel and . A plume cross-section was viewed using a vertical light sheet and a periscope pointed upstream.

Chapter 4

Flow Visualization of Vortex Shedding

4.1 Introduction

The downwash velocity model presented in Chapter 2 is based on the existence of a counter rotating streamwise pair of line vortices at the stack tip. An early study on downwash, conducted by Sherlock and Stalker (1941), suggested a stack tip streamwise vortex pair exists and presented evidence, shown in Figure 2-4, to support this claim. Mauli and Young (1973) performed studies that support Sherlock and Stalker's claim. Ayoub and Karamcheti (1982), contend that such a streamwise vortex pair could not exist.

Flow visualization experiments were performed to help ascertain if a tip vortex pair existed. By painting fluorescein onto a stack, as described in Chapter 3, the flow around the stack model used in the plume rise experiments was observed. In this chapter the images obtained from the visualization verify that a time averaged streamwise vortex pair exists.

4.2 Tracking Vorticity

The key to successfully visualizing the vorticity is placing the dye where the vorticity is produced. It is a consequence of Helmholtz's theorem that for an inviscid fluid, fluid particles that are once vortical shall remain so and will move with the fluid as material lines. For a circular cylinder, the bulk of the vorticity is produced before the boundary layer on the cylinder separates. The vorticity flux from the stack surface is proportional to the square of the velocity, u_{surface} just outside the boundary layer on the cylinder, see Figure 4-1. According to Batchelor (1967), the greatest differences in u_{surface} and consequently vorticity flux, are found in the first 60° from the stagnation point. The large increases in vorticity flux suggest a significant amount of new vorticity is being produced. In Figure 4-1, the shaded region on either side of the stagnation point marks the location and amount of vorticity production on the cylinder. A comparatively small amount of vorticity will be produced along the rest of the cylinder.

The development of the von Karman vortex street can be described in terms of vorticity transport. The positive (clockwise) vorticity produced on one side of the cylinder and the negative (counterclockwise) vorticity produced on the other side

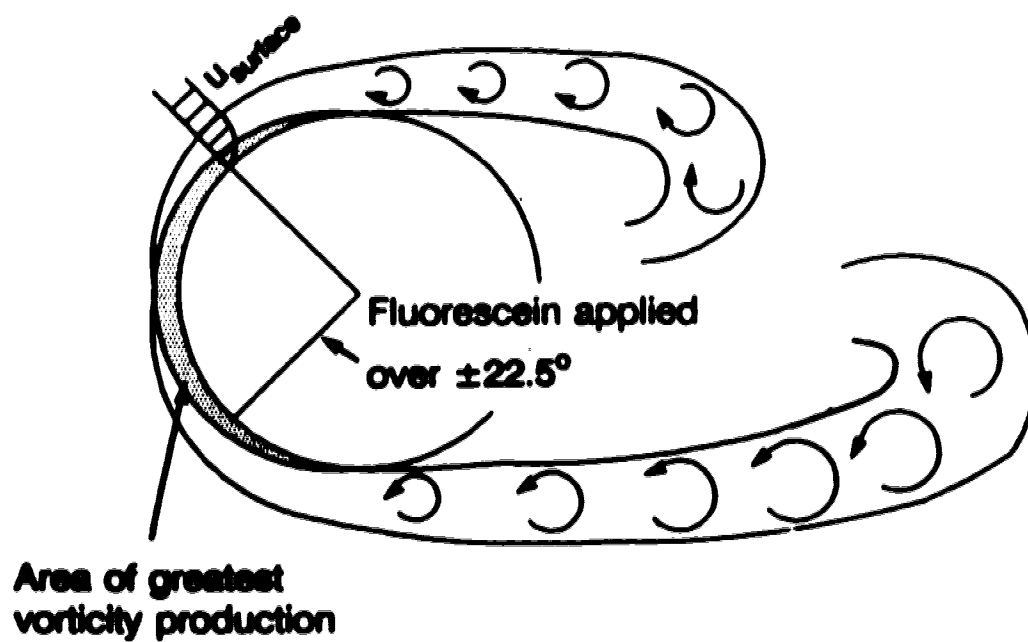


Figure 4-1: Vorticity production on a cylinder.

of the cylinder are carried to the rear of the cylinder. Ultimately more of each sign of vorticity is present at the rear surface than is needed to satisfy the no slip condition and back flow is induced creating two standing eddies. At Reynolds numbers above 40 the back flow becomes unstable and the two standing eddies begin to oscillate. At regular intervals, rotating fluid is shed into the wake as discrete vortices. These vortices arrange themselves into two regularly staggered rows on either side of the stack. Batchelor (1967) suggests that most of the vorticity in the wake is concentrated in these vortices.

Some experimenters try to track vorticity in the wake by releasing dye into the flow upstream of the stack, but this method only tracks streaklines which may be deflected by the vortical flow. To follow the actual vortical fluid, dye must be placed on the surface of the stack where the vorticity is produced.

For this study the stack was painted in three patterns. The entire stack was initially painted to ensure all vorticity was tracked. This method released too much dye into the flow making identification of flow structure very difficult. In a second trial, only one side of the stack was painted. Again, too much dye was released making identification of flow structure difficult. Painting 25% of the stack circumference on either side of the stagnation point, see Figure 4-1, was the final and most effective method used. The vorticity was tracked effectively because most of the vorticity is produced within the area covered with fluorescein and is carried to the other regions of vorticity production.

The spatial dissipation of the vorticity for subcritical Reynolds numbers is dominated by momentum diffusion by viscosity. A pertinent question when using dye to track vorticity is which will diffuse faster, the dye or the vorticity? If dye diffuses faster than vorticity, the presence of dye would not guarantee vorticity is also present. This could cast suspicion on conclusions made from the flow visualization. The relative diffusion can be determined by comparing the diffusion rate of vorticity and dye from a line source. Appendix B is a detailed derivation of the ratio of diffusion for the vorticity and dye. The result, from Equation B-29, is

$$\frac{\delta_v}{\delta_c} = \left(\frac{\nu}{K_{dy}} \right)^{0.5} \quad (4-1)$$

where δ is the diffusive length scale to which 90% of the vorticity or dye is contained. We recognize the Schmidt number, a ratio of the viscous diffusion to concentration

diffusion, appearing in Equation 4-1 is

$$\frac{\delta_v}{\delta_c} = Sc^{0.5} \quad (4-2)$$

Therefore, the vorticity will diffuse $Sc^{1/2}$ times faster than the dye. The Schmidt number in this experiment was much greater than one. Therefore, the vorticity would diffuse faster than the dye, implying dye will always be in the presence of vorticity when diffusion is dominant in material transport.

4.3 The von Karman Vortex Street

Only a few studies have been reported for the structure of the von Karman vortex street shed near the end of a finite cylinder. Visualizing the von Karman vortex street was the first goal of the flow visualization. Plate 4-1 is a picture of the von Karman vortex street shed from the stack, with no exit flow. Two key points are raised in this picture. The first point is the oblique, as opposed to parallel, shedding of the vortex street. The oblique shedding is not surprising, as Williamson (1989) showed oblique shedding could be produced by changing the pressure conditions at the end of a cylinder so the end condition did not match the flow over the span (in this case height) of the cylinder. Since the flow over the span of the stack will be different than the flow at the free end, oblique shedding should result.

The second point from Plate 4-1, concerns the connection of the vortex street. It is known, from Batchelor (1967), that a line vortex must either end on itself, at infinity or at a boundary satisfying the no slip condition (i.e. spinning disk). In the case of the vortex street, which does not extend to infinity, the line vortex making up the vortex street must end on itself. As vorticity was produced on either side of the stack, the vorticity from each side appeared to connect over the stack tip. As each packet of the von Karman vortex street was shed from the cylinder the connection remained intact. This produced a criss-cross pattern of vorticity connecting each vortex in the vortex street. This pattern is shown in Figure 2-3. In Plate 4-1, the bridges or linking vorticity are indicated by the lines seen at the top of the vortex street. Each of the linking vortices will have a vorticity component in the streamwise and cross stream directions. The streamwise component of the vortex street bridges would create vorticity perpendicular to the stack. The sign of this vorticity would be the correct sign to produce downwash.

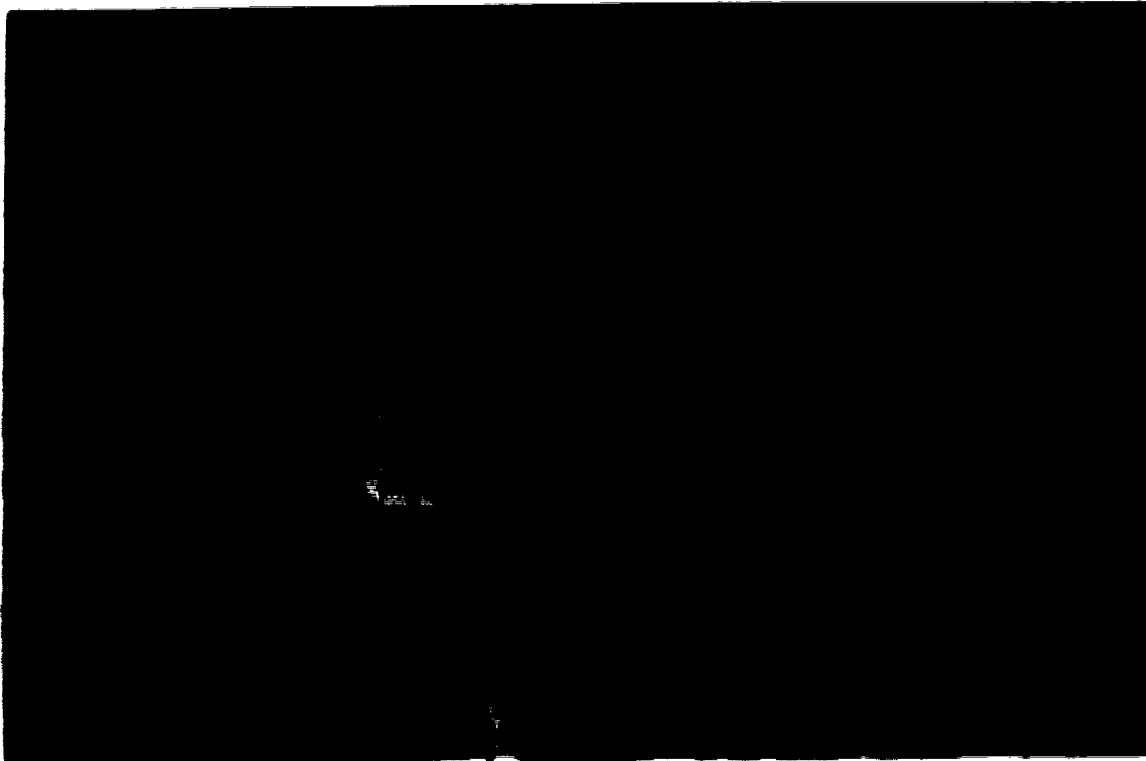


Plate 4-1: von Karman vortex street shed off a 9.6 mm O.D. finite cylinder at a Strouhal number of 0.19.

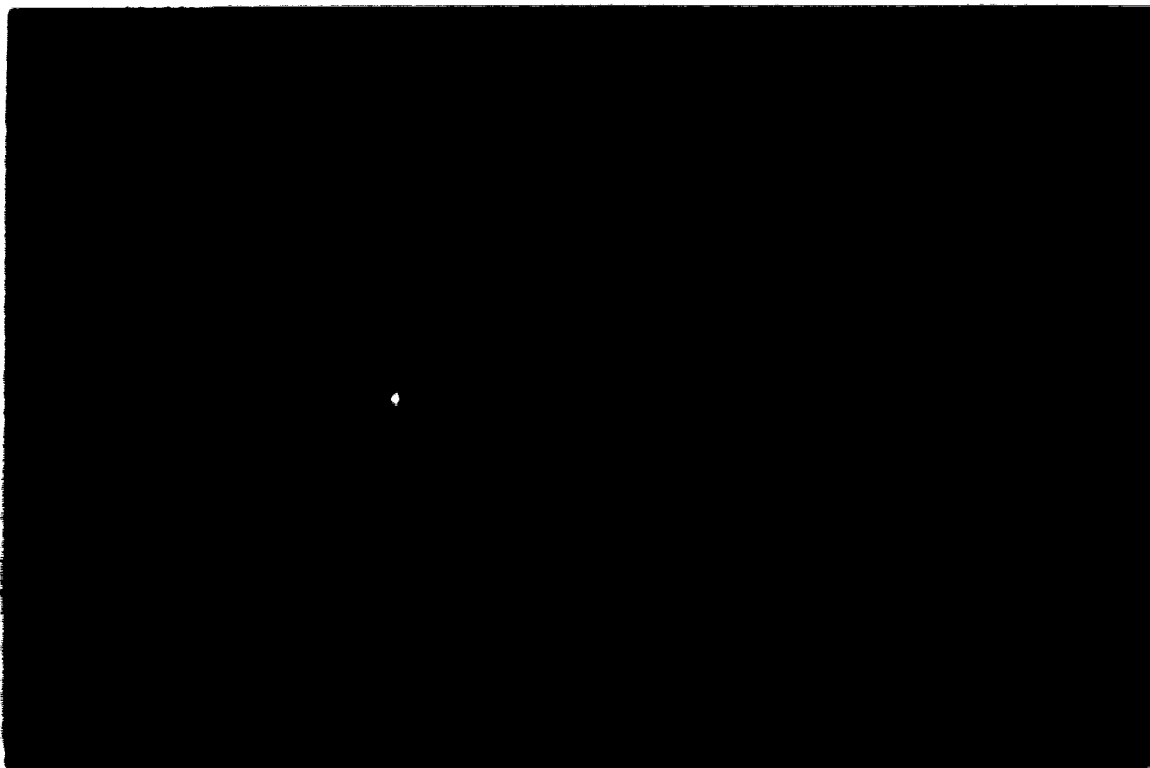


Plate 4-2: Connection of two vortices in the von Karman vortex street.

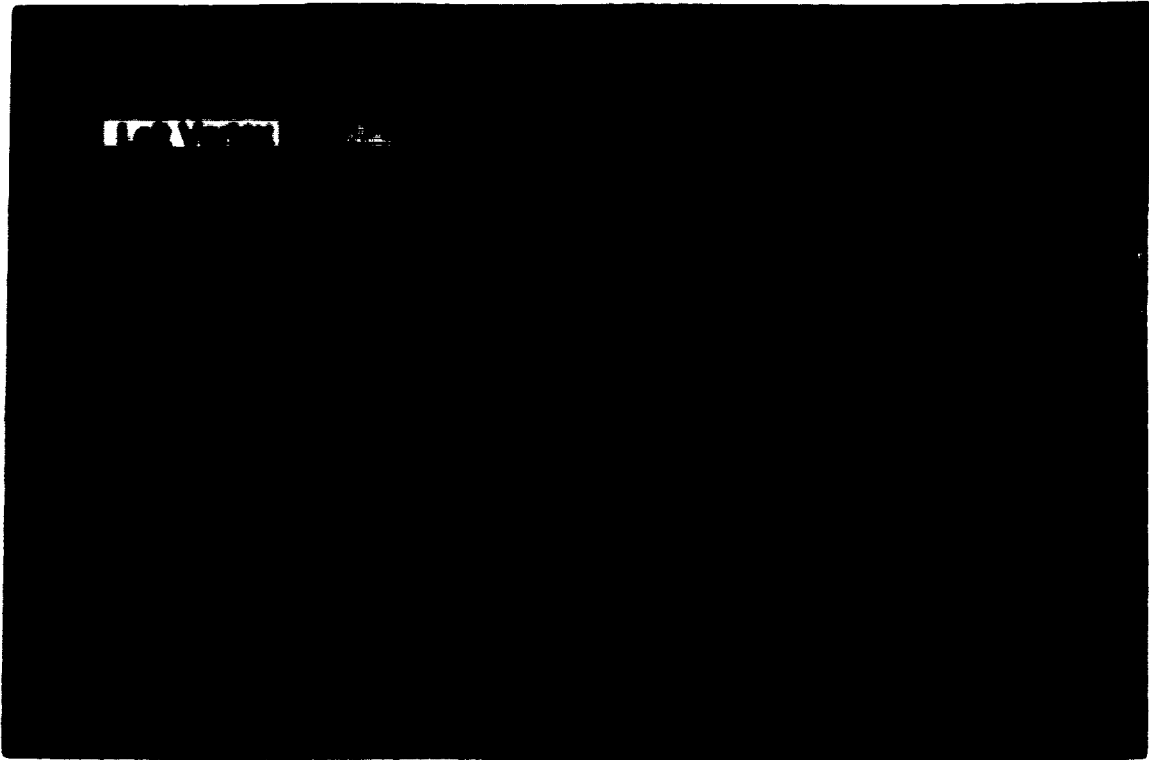
Plate 4-2 is a picture of the vortex shedding close to the stack tip. The dashed line in Plate 4-2 traces a vortex filament that is connected to the already shed packet and connects to the packet about to be shed. As the vortex street moves downstream, the filament remained connected to both packets of the vortex street.

The cross connection of the vortex street suggests a net streamwise vorticity could be created producing a flow pattern similar to a vortex pair. To examine the streamwise vortices the vortex shedding was visualized looking upstream at the stack.

4.4 Visualization of Streamwise Tip Vortices

The laser sheets were positioned so the periscope, looking upstream, could be used to view a cross section of the vortex street. In individual images the flow field did not appear to resemble the flow field produced by a vortex pair. There appeared to be a single vortex moving laterally at approximately the frequency of the shedding vortex street. Plate 4-3 illustrates the presence of streamwise vorticity on the end of its lateral travel. In Plate 4-3a, a vortex is seen on the left side of the stack (dashed line) while in Plate 4-3b another vortex is seen on the right side of the stack. The vortices are at the same height in reference to the stack tip. A time average was taken of the alternating vortices to determine if any structure would be visible.

Figure 4-2 is a concentration contour plot of a 50 second time averaged image at $x = 2D$ and $x = 30D$ downstream. In Figure 4-2a, the contour lines suggest a flow pattern consistent with the presence of a vortex pair. In Figure 4-2b this pattern does not appear as well defined, but it is detectable. The clutter in Figure 4-2b could be attributed to the lateral movement, or fluttering, of the vortex street, smearing the image. This side to side y direction fluttering was removed by aligning the concentration centroids of the individual images and then time averaging. The resulting averages are shown, as concentration contour plots, in Figure 4-3. In Figure 4-3b, removing the flutter 30 diameters downstream produced a clearer picture of the flow structure, exhibiting structure characteristic of a vortex pair. The presence of flow structure similar to flow produced by a vortex pair suggests a vortex pair exists at the stack tip as a time averaged quantity. Since each packet in the von Karman vortex street is connected by a linking vortex which has vorticity components in the streamwise direction, the time averaged vortex pair will be a combination of the connecting vorticity from many packets. The structure observed in Figure 4-2 and Figure 4-3 is a result of an effective, time averaged vortex pair. Since plume quantities such as rise height and dilution are based on time averaged plumes, the

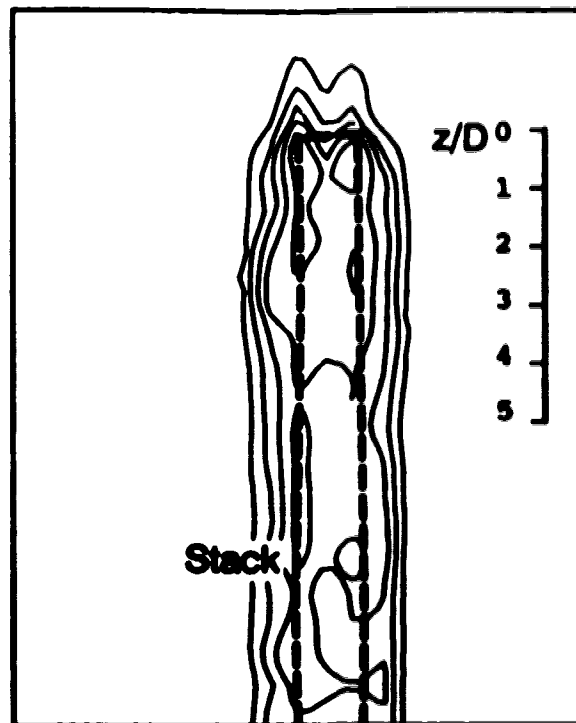


a)

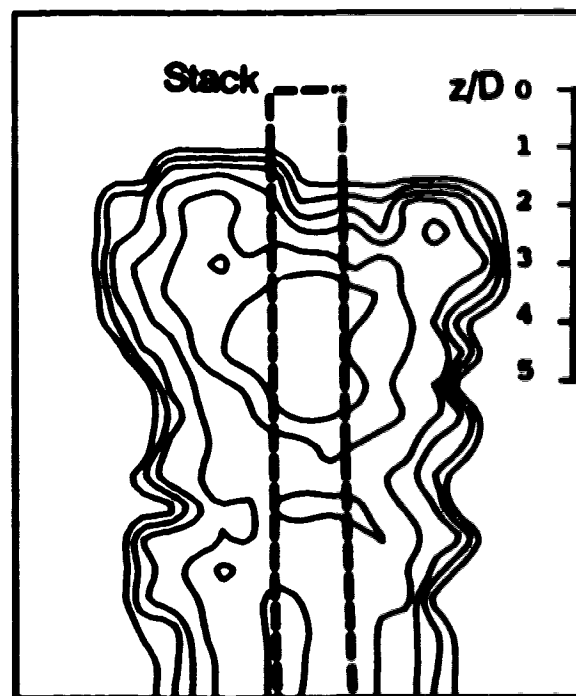


b)

Plate 4-3: Cross sectional stack wake looking upstream at approximately $x = 16D$ downstream showing the presence of alternating streamwise line vortex at the stack tip height (Time delay between pictures $\Delta t U_j/D = 6.25$).

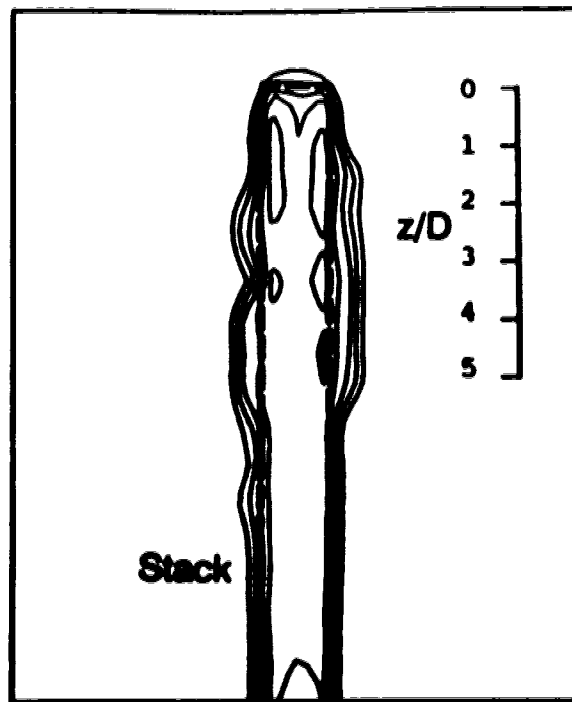


a)

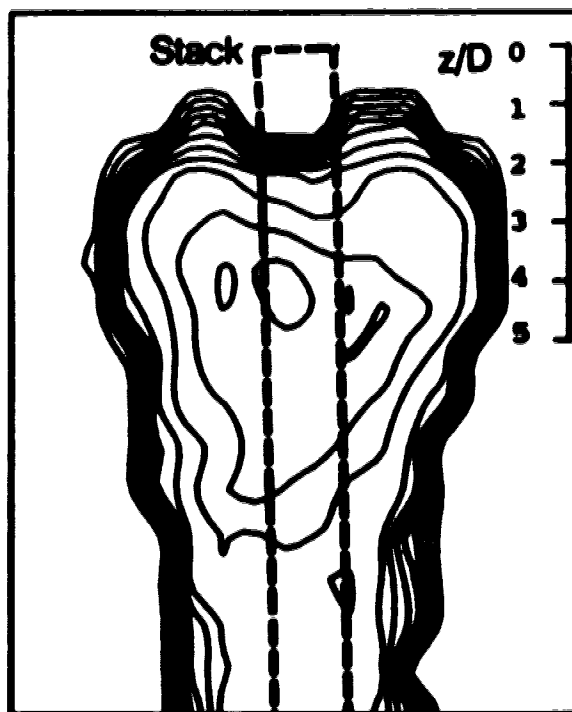


b)

Figure 4-2: Concentration contour plot of a time averaged y-z cross section looking upstream of the von Karman vortex street at a) $x=2D$ and b) $x=30D$ downstream.



a)



b)

Figure 4-3: Concentration contour plot of a time averaged y-z cross section looking up stream of the von Karman vortex street with centroid flutter removed at a) $x=2D$ and b) $x=30D$ downstream.

appearance of a time averaged vortex pair is consistent.

The presence of a time averaged vortex pair, produced as a result of the connection of each packet in the von Karman vortex street, provides an explanation of the results found by other experimenters, like Sherlock and Stalker (1941). According to Ayoub and Karamcheti (1982), a vortex pair is dynamically impossible since the cylinder is a non-lifting body. The results of this flow visualization experiment suggest the non-lifting body argument does not preclude the presence of a time averaged vortex pair at the stack tip.

4.5 Effect of Stack Effluent Jet on Vortex Structure

The vortex structure behind a stack emitting a momentum jet was also studied. A plume would be expected to have some impact on the connection of the vortex street. To examine this, similar experiments to those described in Section 4.2 were performed with a plume, at high and low exit velocities. The low exit velocity jet ($M = 0.5$) did not seem to noticeably change the vortex shedding pattern and the time averaged vortex pair could still be seen. However, when the plume had a high exit velocity ($M = 8.0$) the result was quite different. Plate 4-4 shows how the vortex street is carried up with the plume, apparently connected in the plume, rather than connected at the stack tip. Plate 4-4 does not present enough information to determine how the vortex street interacts with the plume. As the exit velocity of the plume increases the connection of the vortex street which produced the time averaged vortex pair will be altered. In the downwash velocity model, the alteration of the connection of the vortex street is accounted for by a reduction in the strength of the pair of streamwise line vortices, as M increases.

4.6 Summary

The investigation of the structure of vortex shedding from a finite cylinder produced several important results.

- The von Karman vortex street is shed obliquely from the stack and has cross connecting vortex bridges which connects each of the vortex packets.
- The cross connection of each of the packets in the vortex street produces net streamwise vorticity in the horizontal plane (in reference to the stack).



Plate 4-4: von Karman vortex street interacting with a plume exiting the stack.

- The horizontal vorticity does not produce a continuous steady vortex pair. A steady, time averaged streamwise vortex pair is produced by the streamwise component of the connection of each packet in the vortex street. The time averaged vortex pair will produce the same average downwash effects as a stationary vortex pair.
- The connection of the von Karman vortex street is not significantly altered when a low exit velocity plume exits the stack. The connection is altered when a high velocity plume exits the stack. The von Karman vortex street appears to connect into the plume, but the nature of the connection was not clear.

Chapter 5

Velocity Measurements

5.1 Introduction

This chapter presents the results of the Laser Doppler Anemometry experiments. The velocities and turbulent intensities of the water channel flow and the stack exit flow were measured. This information was used to determine Reynolds numbers and momentum correction factors.

Two and three dimensional wakes behind the stack were studied, as well as the wake at the stack tip with and without a jet. The wake at the stack tip with a jet issuing from the stack closely resembles a two dimensional wake. This wake investigation agreed with existing theories for self-similar wakes, and aided in the determination of the power, n , used in the downwash velocity model.

5.2 Velocity Measurements of the Water Channel

The velocity and turbulence intensities are shown in Figure 5-1 and Figure 5-2. Data were collected at distances from the stack exit $x = -30D$, $-20D$, $-10D$ and $0D$, but only the data at $x = 0D$ are shown. Data were collected at those four positions because the stack was positioned at those locations for various tests. The velocity data at all locations agreed within one percent. Figure 5-1 shows the velocity and turbulence intensity for the horizontal $x-z$ plane of the water channel. The stack exit was horizontal, pointing across the channel, in the z direction 305 mm from the side wall. There was a boundary layer on the side wall which extends out to 75 mm. An average velocity of about 19.3 cm/s was found with a maximum velocity of 20 cm/s and a minimum of 18.8 cm/s. Once outside the sidewall boundary layer the turbulence intensity was approximately 2%. The dotted line indicates the position of the source in this plane. Figure 5-2 shows the same information in the vertical $x-y$ plane. There was a boundary layer near the bottom wall, an average velocity of 19.3 cm/s and turbulence intensity of about 2%. The dotted lines on this figure represent the source height and the water level.

5.3 Stack Model Development

As discussed in Chapter 3, the stack was fashioned with a 90° bend so dye could be injected horizontally from the side wall of the water channel. Figure 5-3 is

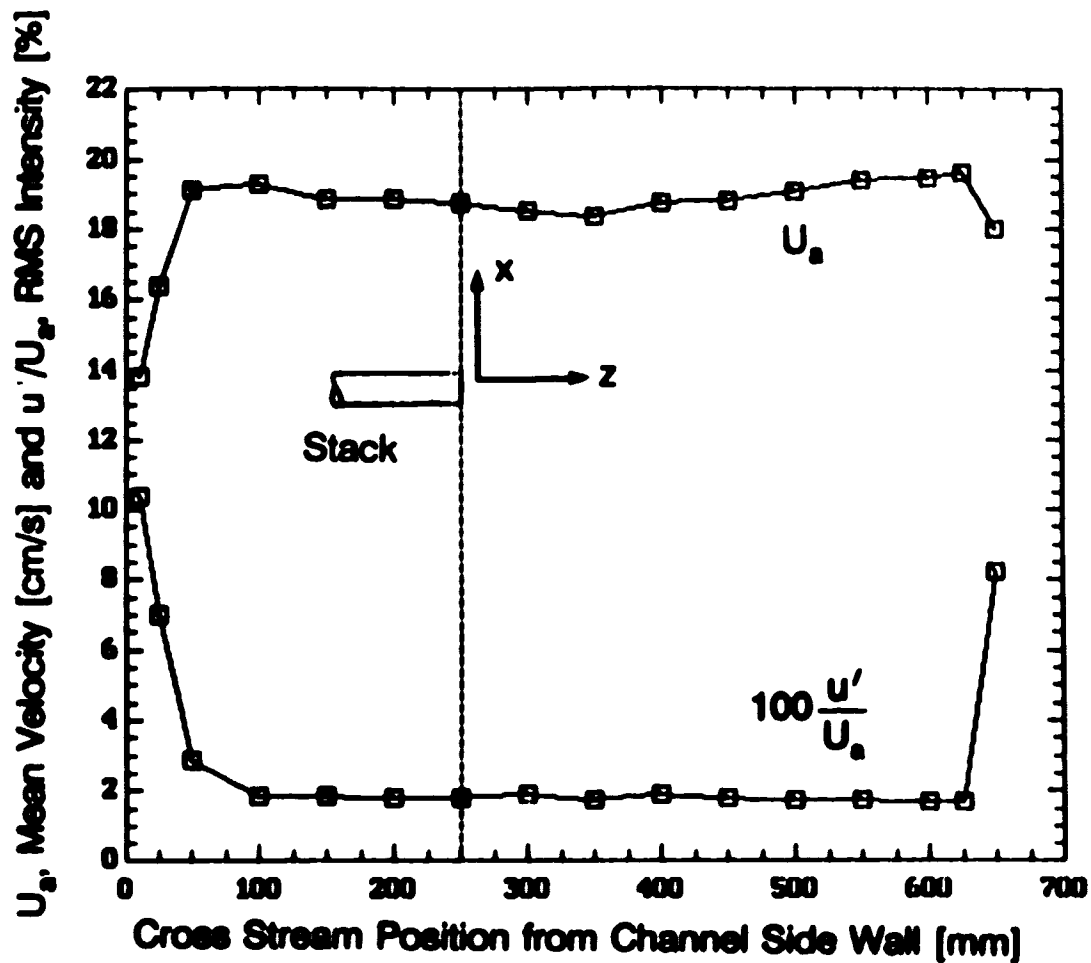


Figure 5-1: Cross stream profiles of mean velocity and streamwise turbulence intensity at $x/D = 0$.

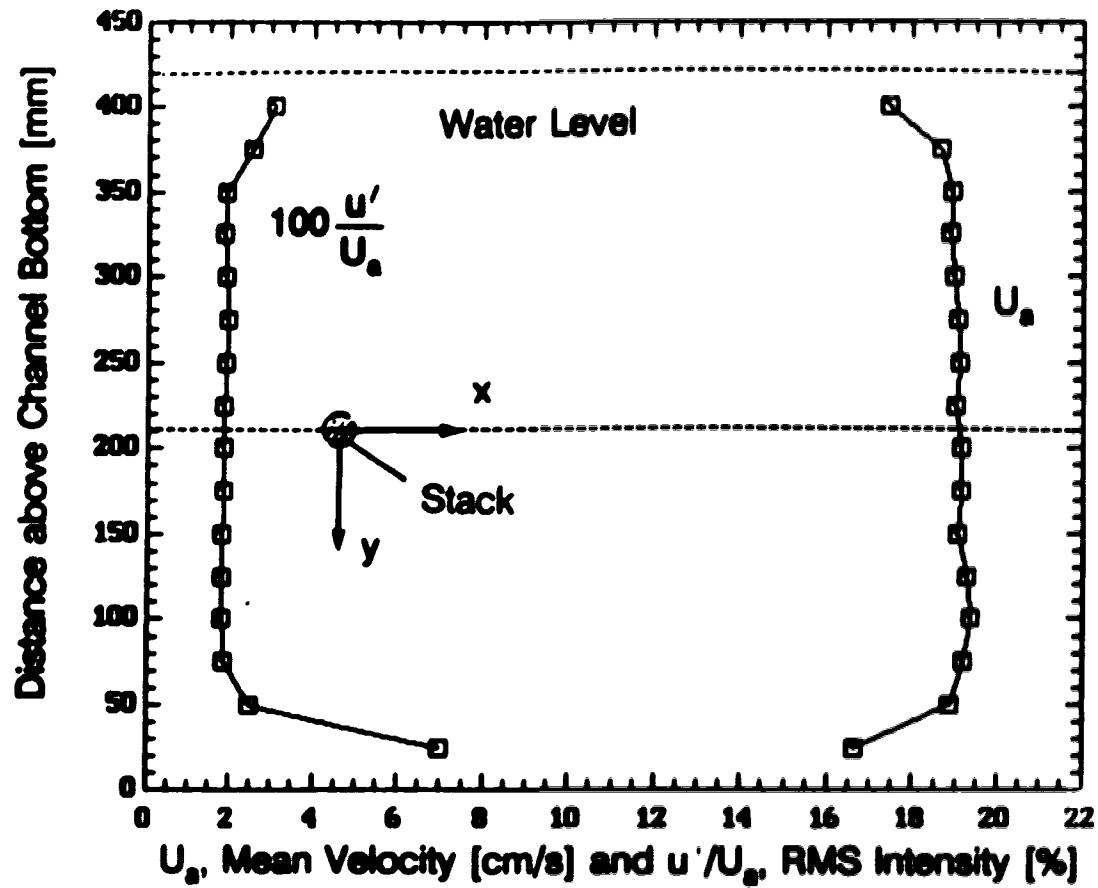


Figure 5-2: Vertical profiles of mean velocity and streamwise turbulence intensity at $x/D = 0$.

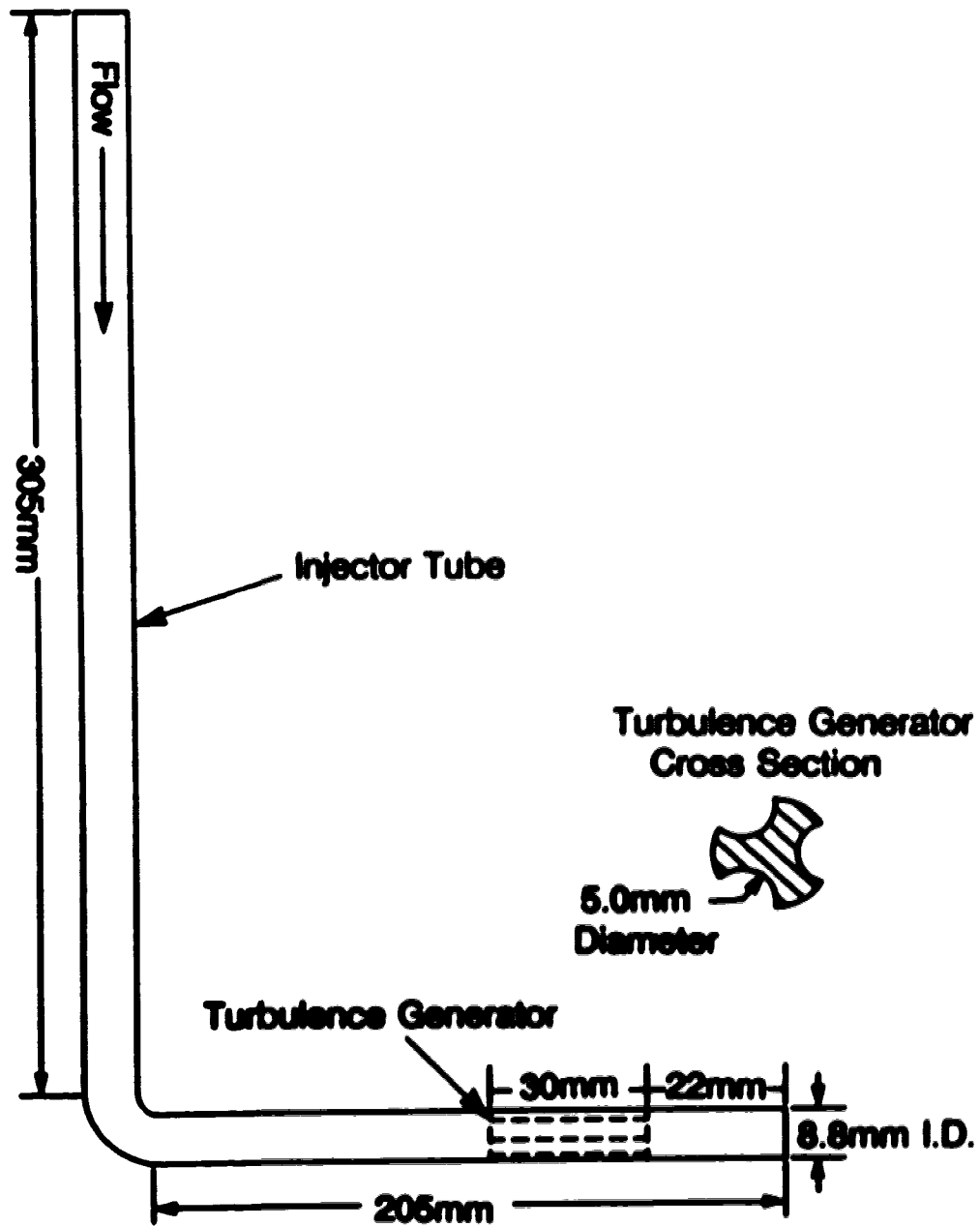


Figure 5-3: Stack model and fluted turbulence generator plug.

a schematic of the stack showing how it was designed to inject horizontally. The long end could be attached to the water channel using a clamp and positioned so the short end was perpendicular to the flow. The stack was made of thin walled brass tubing (9.6 mm O.D., 0.4 mm wall thickness) and was painted flat black to reduce any reflections of the laser light.

The undisturbed velocity profile exiting the stack is shown in Figure 5-4. The undisturbed velocity profile did not satisfy the top-hat profile assumption of the plume rise model. To develop a flat, turbulent profile a turbulence generating plug was placed in the stack to force the undisturbed flow to become turbulent. Several different plugs were tested and are labelled a) through d) in Plate 5-1. The fluted turbulence generator used in this thesis, seen in Figure 5-3 and labelled d) in Plate 5-1, had three 5.0 mm diameter holes drilled at 120° intervals with their center's on the plug circumference, producing an open area of 44%. The turbulence generator was 30 mm in length and was placed 2.5 diameters from the exit. This plug acted not only as a turbulence generator, but also as a flow straightener. It produced the velocity profile shown in Figure 5-5, with approximately 12% turbulence at $Re = 1600$.

An interesting, but unusual result was that the turbulence intensity at the exit for the turbulent flow, shown in Figure 5-5, was lower than for the undisturbed flow, shown in Figure 5-4. A possible explanation for this difference is that a secondary flow was produced by the elbow, causing the increased turbulence in the undisturbed flow. Another cause for the difference could be due to the difference in the undisturbed and turbulent velocity profiles. Since the velocities in the undisturbed profile were lower than the velocities in the turbulent profile, the turbulent intensity would be higher for in the undisturbed flow due to the definition of turbulent intensity. The undisturbed flow was not used in any experiments. Profiles taken in the y and z directions indicated the flow was similar in both directions.

5.3.1 Average Velocity Corrections for Momentum Flux

The momentum ratio in Equation 2-6 was based on the assumption that the stack exit velocity was a uniform top-hat profile. This meant the average velocity could be used in the calculation of both mass and momentum fluxes. As we have shown in the previous section, the stack exit velocity profile is not an exact top-hat profile. To use the average stack exit velocity in momentum calculations, a momentum correction factor, α_m , must be included in the equation for momentum

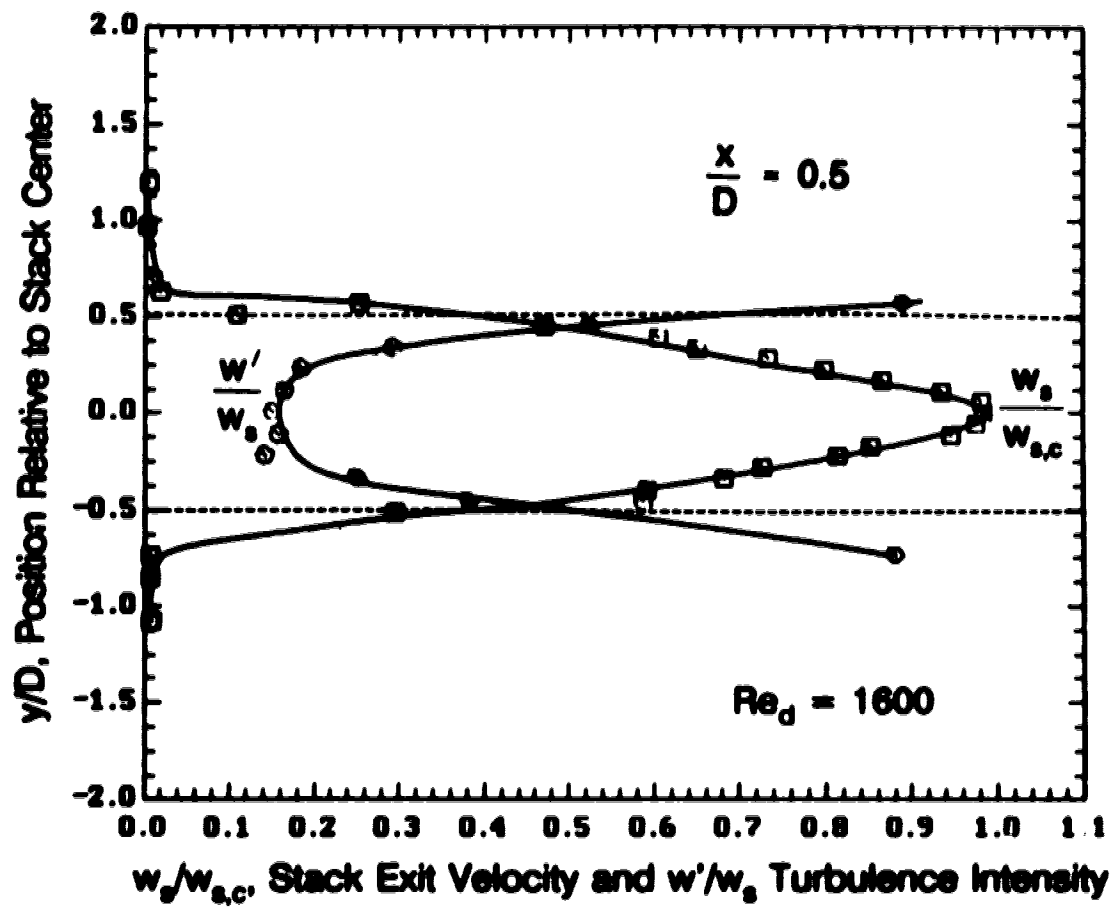


Figure 5-4: Mean velocity and turbulence intensity profiles in quiescent fluid ($U_s = 0$) at $x = 0.5D$ from the stack exit with no turbulence generator inside stack.

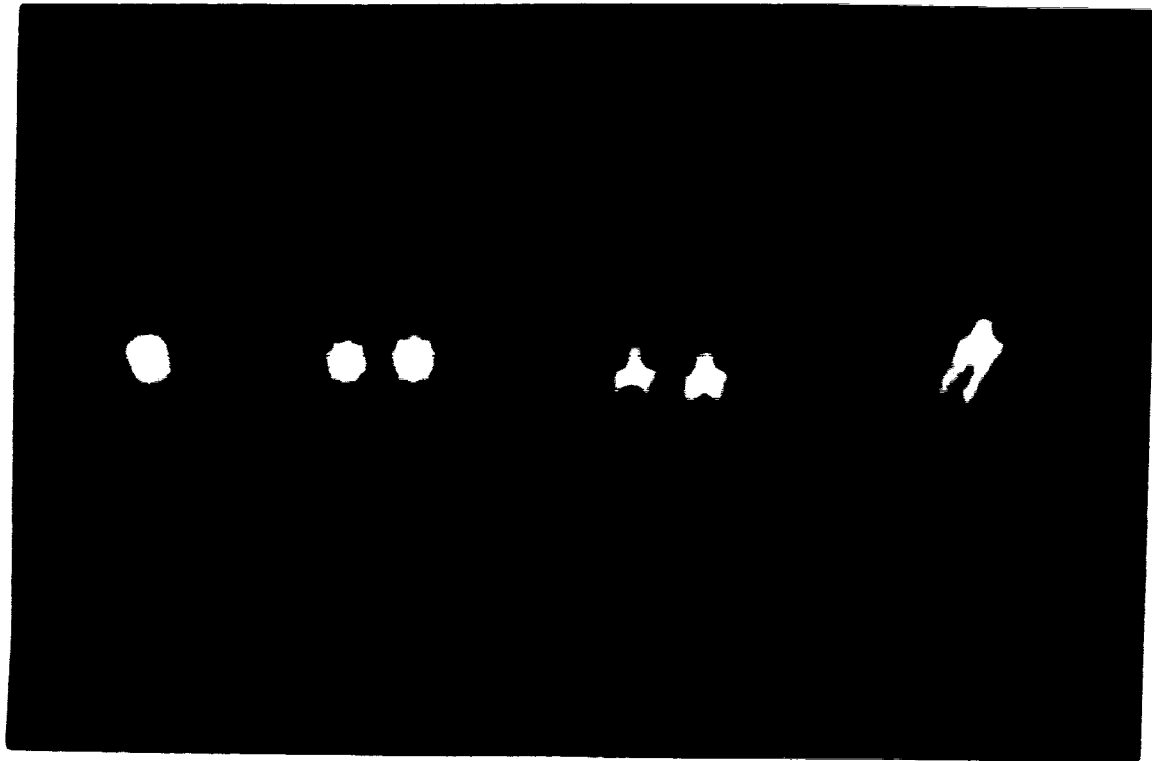


Plate S-1: Fluted Turbulence generator plugs tested.

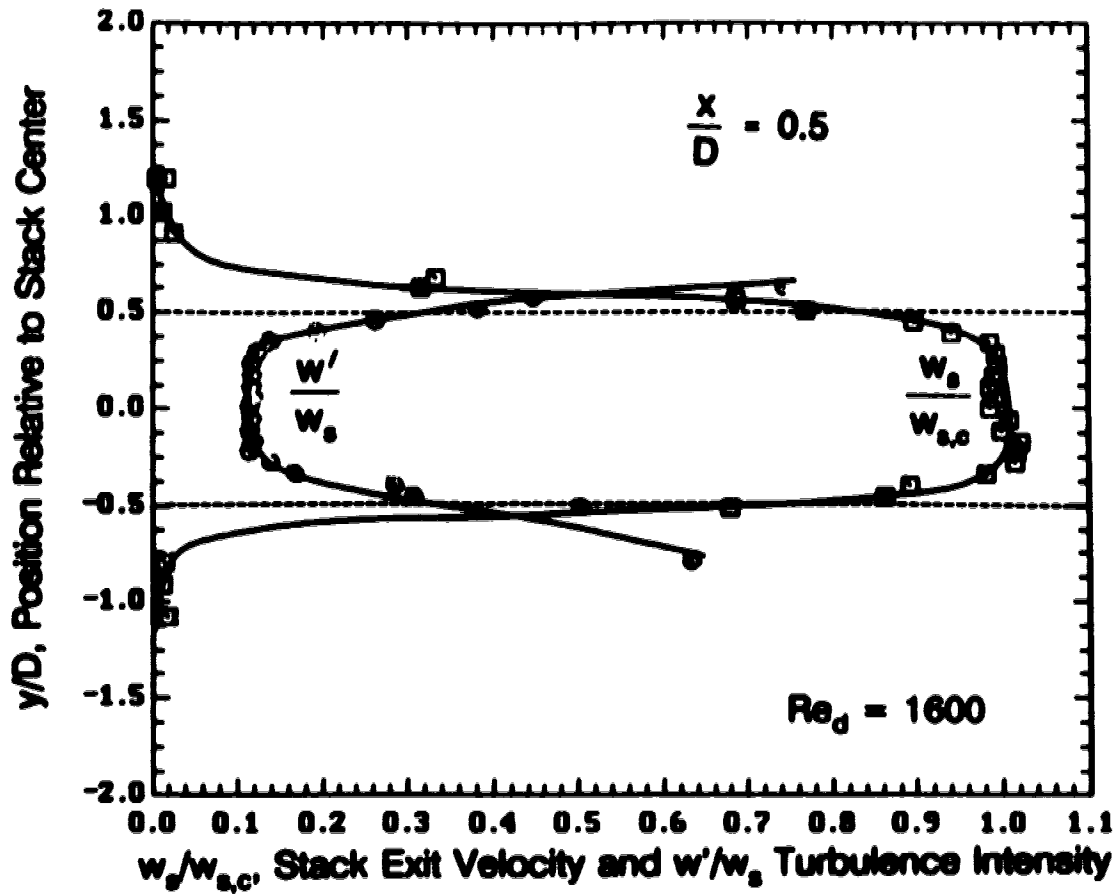


Figure 5-5: Mean velocity and turbulence intensity profiles in quiescent fluid ($U_s = 0$) at $x = 0.5D$ from the stack exit with fluted turbulence generator in place.

flux. This correction factor is defined by

$$\alpha_m \rho_s \pi R_s^2 \left(\frac{\bar{w}_s}{w_{s,c}} \right)^2 = \int_0^{R_s} \rho_s 2\pi r \left(\frac{w_s}{w_{s,c}} \right)^2 dr \quad (5-1)$$

where R_s is the radius of the exit, w_s is the plume velocity at any radius r , and $w_{s,c}$ is the plume centerline velocity. This correction is made in other studies such as Neiman (197ⁿ). The extreme values for α_m would be 2.0 for a laminar parabolic profile and 1.0 for a uniform flow. The correction factor for a full scale stack, assuming a $1/7^{\text{th}}$ power law profile, would be about 1.03. Using the trapezoidal rule to integrate Equation 5-1 over the stack exit, α_m was found to be 1.28. This was also done for a velocity profile 90° to the original plane and agreed within $\pm 3\%$. This affects Equation 2-6 so the corrected momentum ratio would be

$$M = \alpha_m^{1/2} \left(\frac{\rho_s}{\rho_a} \right)^{1/2} \left(\frac{\bar{w}_s}{U_s} \right) \quad (5-2)$$

The momentum correction term was included in the calculations to determine the flow rates used in the experiments.

5.4 Selecting Averaging Time and Sampling Rate for Plume Images

Several factors affected the decision on what averaging time to use and the number of images to average per second. One consideration was that the water channel is a closed system and any dye injected into the water channel recirculates causing an increase in the background concentration. The pressure vessel used in this experiment was able to hold 60 L of injection dye, allowing experiments to run for 30 minutes. Injecting dye for 30 minutes would produce excessive background levels. It was originally felt that to obtain stationary statistics an averaging time of 100 seconds was needed to capture the time-dependant movements of the plume. However, injecting dye for 100 seconds increased the background concentration too quickly. To determine a suitable averaging time less than 100 seconds, data were collected at two velocity ratios, $M = 0.5$ and 3.0 . Ten frames per second were digitized, producing 1000 individual images for each momentum ratio and each image was analysed to determine its centroid. From the 1000 individual centroids, statistics for several smaller sets of data were calculated. The mean rise height remained

constant, within $\pm 2\%$, from 100 to 40 seconds of data. Averaging for less than 40 seconds produced errors in the mean rise height as high as 20%. The standard deviation increased from 100 to 40 seconds within the expected range, where the ratio of standard deviation is $(n_1/n_2)^{0.5}$. To ensure that the statistics would remain constant, an averaging time of 50 seconds was chosen. Averaging for only 50 seconds also significantly reduced the high background concentrations.

The next question was how many frames per second need to be averaged to produce stationary statistics. Figure 5-6 and Figure 5-7 are plots of the mean and standard deviation of plume rise height over 50 seconds of data, averaging several different numbers of frames per second. From Figure 5-6 and Figure 5-7, it is apparent averaging all possible images (30 frames per second) was not necessary, and averaging only five frames per second produced acceptable plume statistics. The image averaging hardware could only average a maximum of 256 images before overflowing. By averaging only 5 frames/second over 50 seconds, 250 images would be averaged and the time averaging hardware would not overflow. Averaging 5 frames/second over 50 seconds satisfied the constraints of long averages for stationary statistics and low background concentrations.

5.5 Wakes Behind Cylinders

One of the key assumptions in the downwash velocity model is that the streamwise vortex pair separation increases at the same rate as the momentum wake growth. This assumption requires the growth of the wake, δ , to be known. The exponents, $n = 0.5$ and $n = 0.33$, for a two dimensional and three dimensional self similar wakes are derived in Batchelor (1967) and Panton (1984). For this study, however, it was the growth of the wake at the tip of the stack that was of greatest interest. Unfortunately, no existing data or theory could be found on the wake at the stack tip, and a study of the growth of three types of wakes was studied to gain new information and confirm existing theories. The three wakes studied were:

- two dimensional wake behind a cylinder
- wake at the stack tip with no effluent jet
- wake at the stack tip with a strong effluent jet

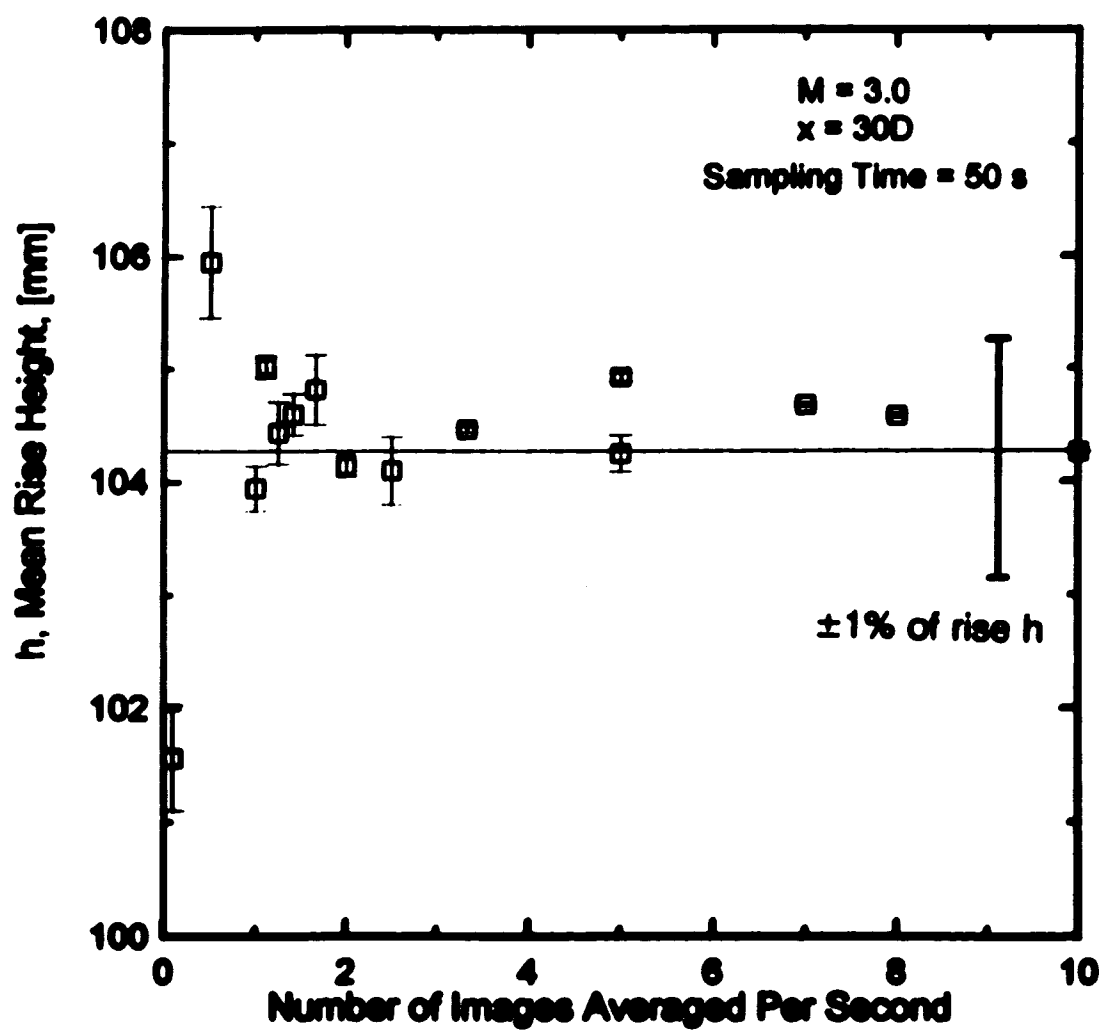


Figure 5-6: Fifty second mean and standard deviation of rise height for various image sampling rates with $M = 3.0$ at $x = 30D$ downstream.

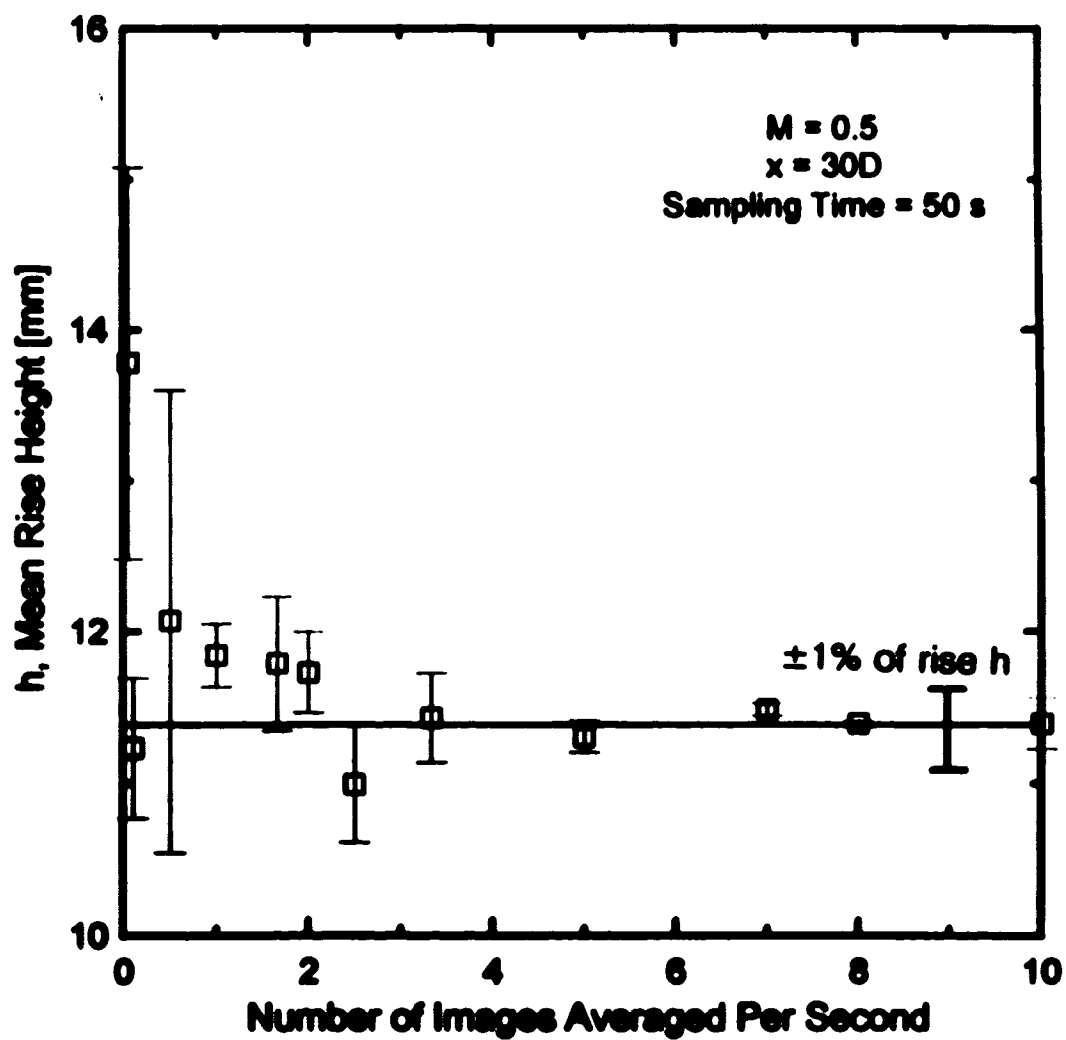


Figure 5-7: Fifty second mean and standard deviation of rise height for various image sampling rates with $M = 0.5$ at $x = 30D$ downstream.

5.5.1 Two Dimensional Wakes

The stack shown in Figure 5-3 was used with a 200 mm extension added to the end to model a full channel width (infinite) cylinder. The velocity data were collected at $z = 0$ (the stack exit) so no changes in the background flow could affect the wake measurements, and no end effects would affect the wake measurements. Velocity measurements were taken over $y = \pm 11D$ on either side of the stack centerline.

Figure 5-8 is a plot of the wake velocity profiles at seven positions downstream of the stack. The growth of the wake was determined by measuring its width δ_y , where the velocity was $(U_s - U_\infty)/2$ or $\Delta U/2$. One point of interest in Figure 5-8 is that in the very near wake ($x = 2D$ and $3D$), the wake velocity profile has a slight increase in velocity above free stream before decreasing in the wake. For these positions, self-similar wake theory will not apply since a mass balance would be incorrect if the velocity increase is not considered. The assumption in self-similar wake theory that $\Delta U \ll U_s$ would not be true at $x = 2D$ and $3D$, invalidating the self-similarity of the wake at those locations.

The exponent of the wake growth n , in $\delta_y = (x-x_0)^n$ was defined in Equation 2-23. In Figure 5-9, the wake growth has been plotted against downstream distance and $n = 0.40$ was determined. To find this power a virtual origin of $x_0/D = 1.0$, was used in determining n for all three types of wakes studied here. The theoretical exponent for a two dimensional wake is expected to be 0.50. A plausible explanation for the difference between the theoretical and measured value is the flow acceleration in the water channel that would transport the wake faster than $x = U_s t$, and would reduce n from 0.5. A set of measurements of U_s with x showed $U_s = x^{0.08}$, making the exponent $n = 0.4(1 + 0.08) = 0.44$. Also shown in Figure 5-9 is the 2D momentum invariant for a self-similar two dimensional wake, $\Delta U \delta_y$. As Figure 5-9 illustrates, once outside the initial near wake region, the 2D momentum invariant is constant, suggesting the far wake behind a 2D cylinder is self similar for $x > 20D$.

5.5.2 Tip Wakes

The growth of two and three dimensional wakes is well documented, but the growth of the wake downstream from the tip of a stack is not. The present study attempted to determine how the wake behaved at the stack tip height ($z = 0$). The first attempt to measure the wake in the x - y plane with $M = 0$ at the same height as the stack tip did not prove to be very enlightening. The measured differences in velocity in the wake were about 0.1% of free stream approach velocity, U_s . This did

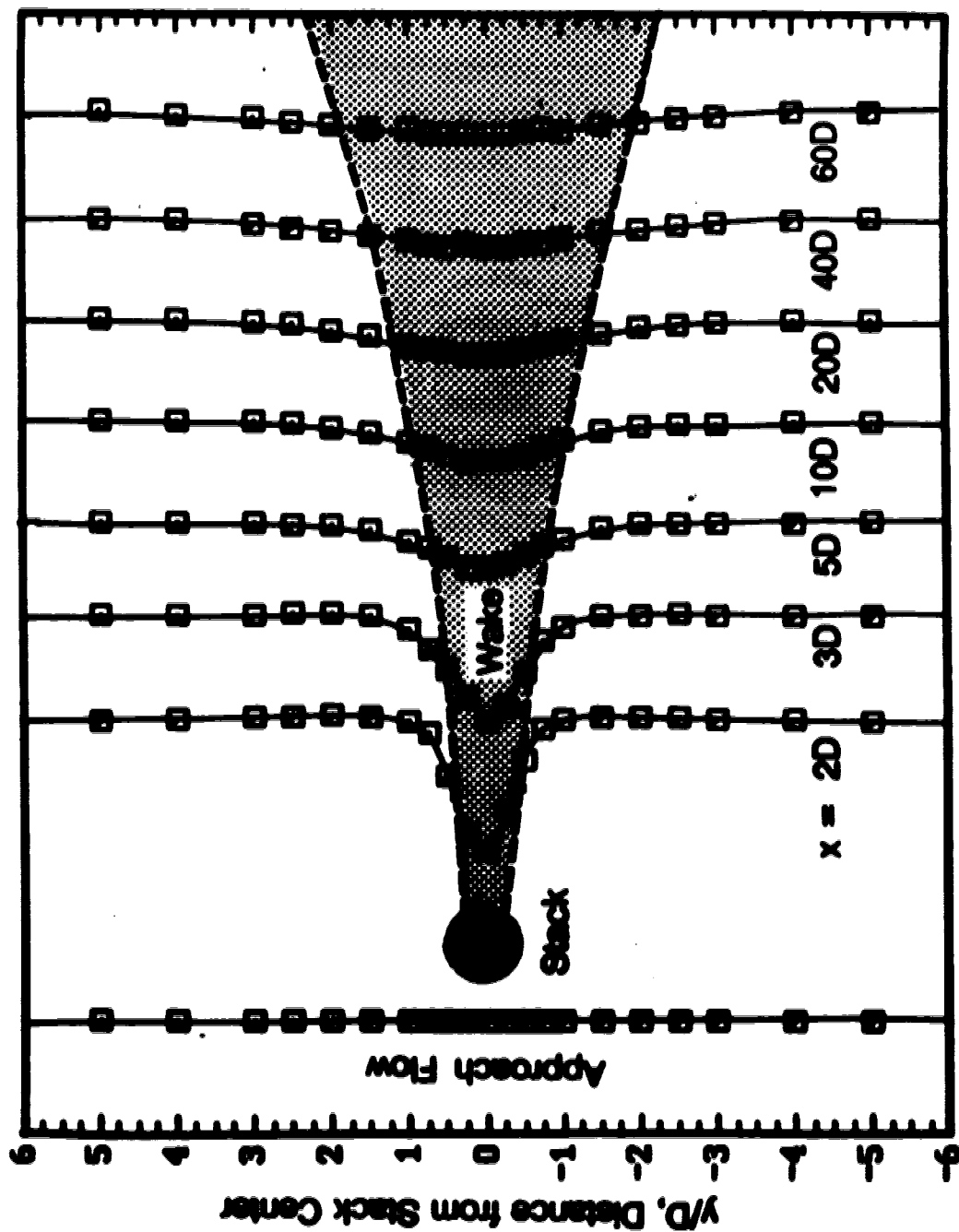
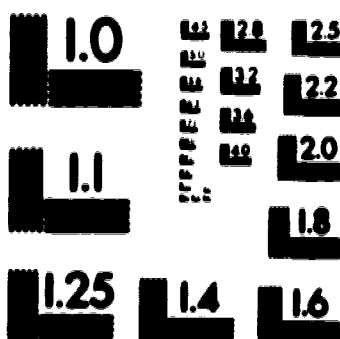


Figure 5-8: Velocity profiles behind an infinite (full channel width) cylinder for six downstream locations. Wake width $\delta_y = (x-x_0)^{0.66}$ defined at $\Delta U/2$ (Note: x positions not to scale).

2 of/de 2

PM-1 3 1/2" x 4" PHOTOGRAPHIC MICROCOPY TARGET
NBS 1910a ANSI/ISO #2 EQUIVALENT



PRECISION[®] RESOLUTION TARGETS

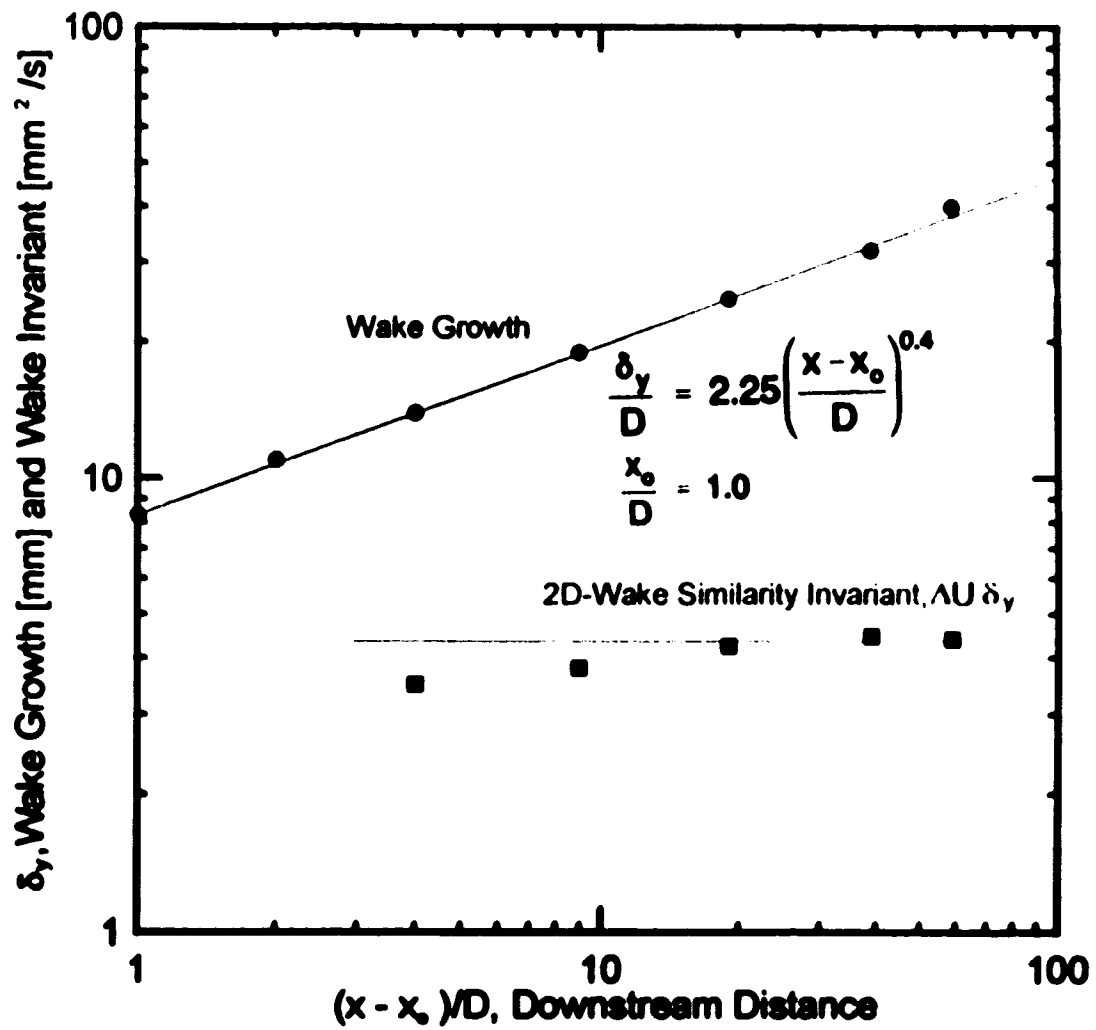


Figure 5-9: Growth of momentum wake and wake invariant for a two dimensional wake behind an "infinite" (full channel width) cylinder.

not permit any reasonable calculation of wake growth. Beyond five diameters downstream of the stack, no detectable velocity difference could be observed. Later flow visualization showed that the tip streamline deflects down about $5D$, so the tip level velocity profiles were in free stream fluid that was washed down into the stack wake. Since the x-y plane measurements provided no usable data a new approach was taken to try and determine information concerning the flow around the stack tip.

To produce some insight of the growth of the wake at the stack tip, the rate of streamline deflection from the stack tip height was measured in the x-z plane. Velocity measurements were made from $z = 11D$ above the stack tip to $z = 13D$ below, along the length of the stack. Figure 5-10 shows the velocity profiles from the seven downstream locations. The top dashed line is the stack height and the bottom line represents the point where the velocity is $(U_s - U_{min})/2$. The shaded region is the transition region between the free stream flow and the full two dimensional wake. The exponent n , of the transition growth, $\delta_z \propto (x-x_0)^n$ was determined to be $n = 0.36$. This is very close to the theoretical three dimensional axisymmetric value of 0.33. To determine if the transition region could be approximated as a three dimensional wake, the 3D momentum invariant, $\Delta U \delta_z^2$, was determined. The invariant, plotted in Figure 5-11, is constant for the far wake and verifies that the transition region exhibits three dimensional axisymmetric wake behaviour.

5.5.3 The Wake Around the Tip with a Strong Exit Jet

The growth of the wake at the stack tip with a strong exit jet was also studied. The behaviour of the flow around a jet from a stack or hole has been studied by Moussa, Trischka, and Eskinazi (1977) and Fric and Roshko (1991). In the present study, a jet with a momentum ratio of 6.0 was emitted from the stack, and the wake in the x-y plane measured. Figure 5-12 shows the velocity profiles at various downstream locations and the stack tip height. The dashed line represents the wake growth and the shaded region shows the wake defined by the point δ_y where the velocity is $\Delta U/2$. The exponent of growth, n , was determined to be $n = 0.39$, as seen in Figure 5-13. This is almost identical to the value determined for the two dimensional wake. A comparison between the velocity profiles of the two dimensional wake and the tip wake with a strong jet indicates they are virtually identical. From this evidence, it was concluded the wake behind the tip with a strong ($M = 6.0$) jet exiting the stack behaves as a two dimensional wake. This conclusion was supported by Figure 5-13, by noting that the 2D momentum invariant, $\Delta U \delta_y$, was

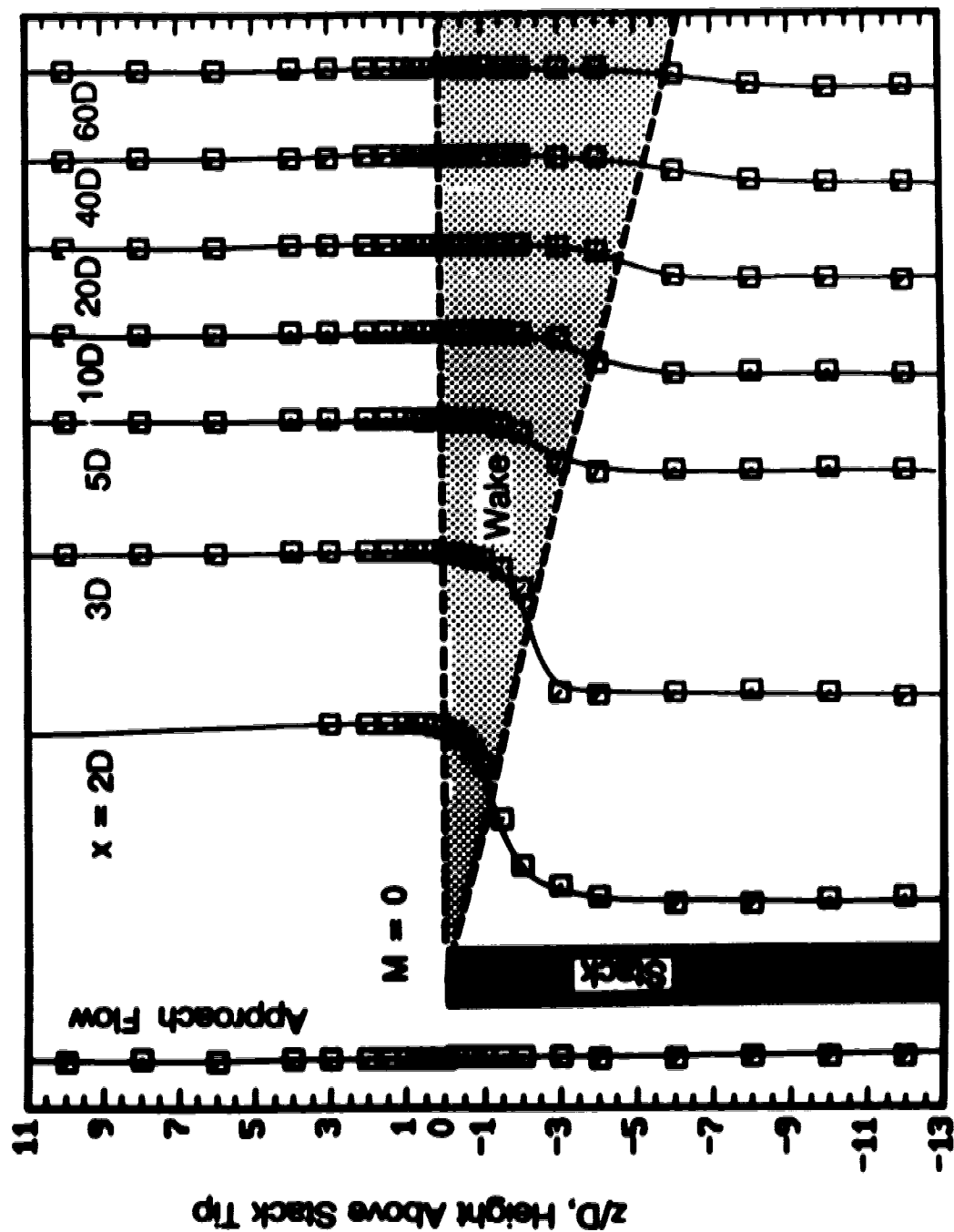


Figure 5-10: Vertical velocity profiles behind an open ended tube with $M = 0$ for six downstream locations. Wake height $\delta_z \propto (x-x_0)^{0.36}$ defined by ΔU^2 (Note: x positions not to scale).

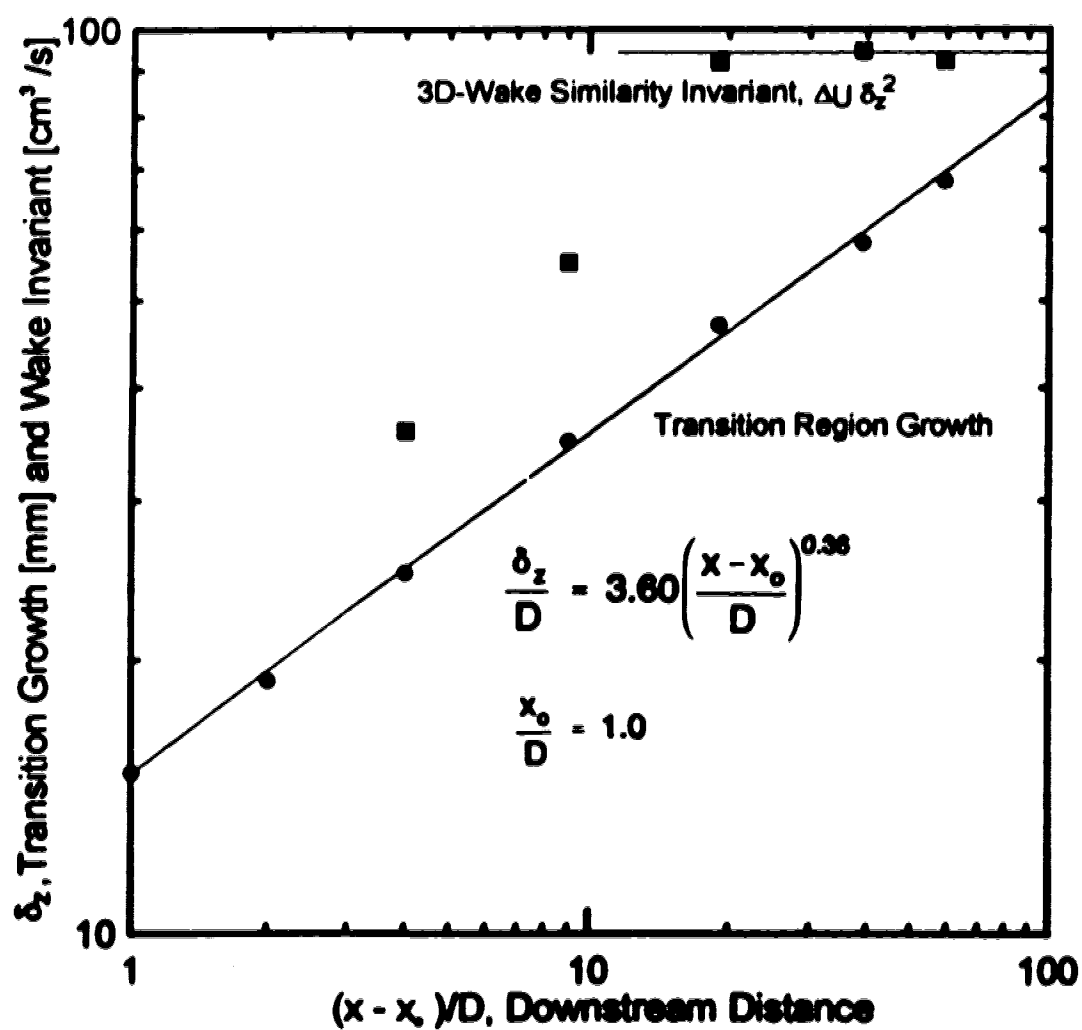


Figure 5-11: Vertical growth of transition region between freestream flow and two-dimensional wake and wake invariant for three dimensional axisymmetric wake.

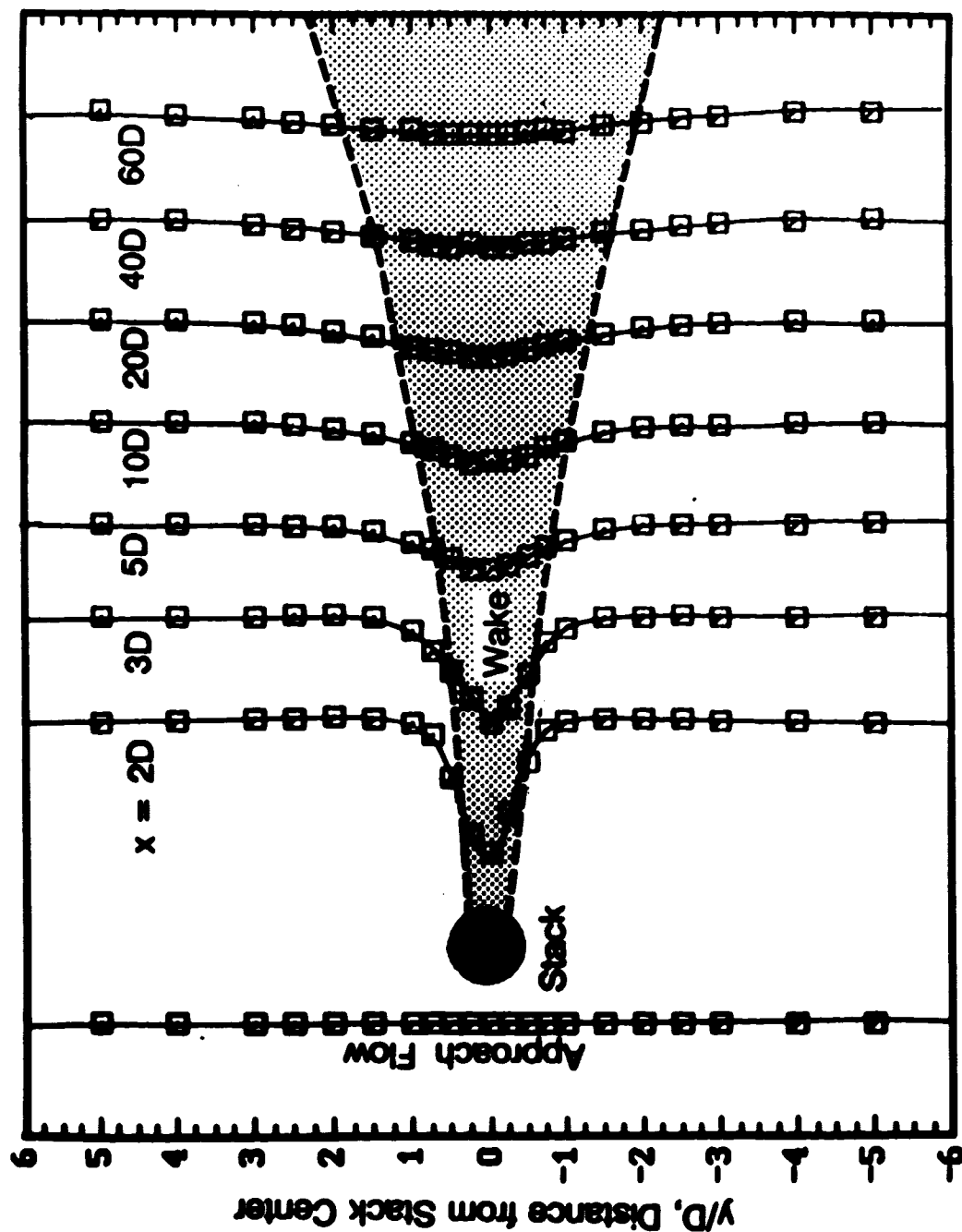


Figure 5-12: Velocity profiles behind the tip of a cylinder with a strong jet ($M = 6.0$) exiting for six downstream locations. Wake width $\delta_1 \propto (x-x_0)^{0.39}$ defined by $\Delta U/2$ (Note: x positions not to scale).

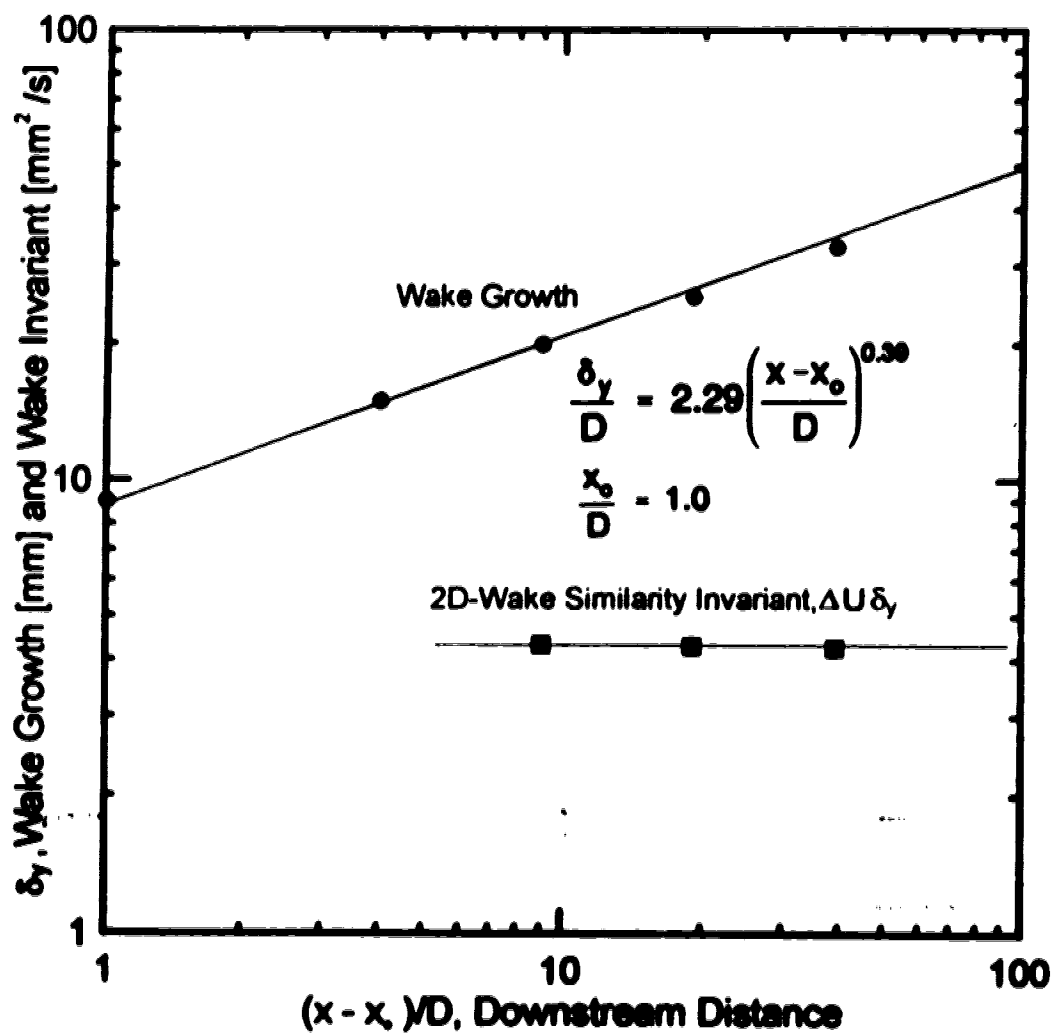


Figure 5-13: Crosswind momentum wake width and two dimensional wake invariant at stack tip height behind a strong jet ($M = 6.0$).

constant in the far region for $x > 10D$. This is an interesting result when compared to the results in section 5.5.2, where no momentum wake could be found in the x-y plane at the stack tip with no exit jet, $M = 0$.

5.6 Determining a Power of Growth For the Downwash Velocity Model

Some reasoning was required to determine what exponent, n , would be suitable for use in the downwash velocity model. The wake at the tip would probably not be a two dimensional wake, since the downwash over the tip displaced the wake edge below the stack tip. It was decided that the exponent, $n = 0.40$ should be used in the downwash velocity model. This exponent was chosen based on two properties:

- It is close to the measured values of the wake growth exponent of $n = 0.39$ with $M = 6.0$ and $n = 0.36$ for the δ_z wake width for $M = 0$.
- It is a compromise between the two and three dimensional axisymmetric self-preserving wake exponents of $n = 0.5$ and $n = 0.33$.

Using an exponent of $n = 0.40$ is a logical choice because it is near the measured values of n found for both the 2D and 3D wakes. It is a semi-empirical determination, based on the physical properties measured in the present study.

5.7 Summary

In this chapter the results of several LDA experiments were discussed. The main conclusions of these experiments were:

- The water channel had a mean velocity of about 19.3 cm/s and a turbulence intensity of 2%, which were constant $\pm 1\%$ over the range of stack positions studied.
- To produce a uniform top-hat profile at the stack exit velocity, a turbulence generating plug was placed inside the stack. The stack exit velocity had a momentum correction factor of 1.28 when the turbulence generating plug was used.
- To compromise between long time averages for better statistics and short

averages to reduce the background concentration an averaging time of 50 seconds taking 5 frames/second was used.

- The growth of three wakes was examined to help determine what exponent, n , should be used in the downwash velocity model. For the 2D wake $n = 0.40$ was found and for the 3D wake in the x - z plane $n = 0.36$ was found. For the x - y crosswind the wake behind a jet of $M = 6.0$ the exponent, n , was found to be 0.39, close to the value of the 2D wake. No useful data could be collected for the x - y wake at the stack tip when $M = 0$.
- The exponent, n , in the downwash velocity model was set at $n = 0.40$. This is a compromise between the theoretical values of $n = 0.5$ and $n = 0.33$, for a 2D and 3D wake and was close to the values of 0.36 and 0.39 observed in the present study for $M = 0$ and $M = 6.0$.

Chapter 6

Comparison of Downwash Models to Experimental Data

6.1 Introduction

In this chapter, three methods of predicting downwash will be compared to experimental data taken for this study. The three models are: a virtual origin correction, an initial dilution correction and a downwash velocity correction. The effects of the entrainment models and changing Reynolds numbers on downwash will be discussed. Finally, the ability of the downwash velocity model to predict dilution and buoyant rise will be examined.

6.2 Effects of Entrainment Coefficient on Predicting Plume Trajectories

The choice of entrainment coefficient for a plume has a large effect on predicted trajectory. The entrainment coefficient encompasses many assumptions in the rise of the plume, as discussed in Section 2.2. Some investigators, such as Hoult and Weil(1972) and Weil(1988) suggest that the entrainment coefficient should be a constant, $\beta = 0.6$, while others like Briggs (1975) suggest that β should have some dependence on the momentum ratio. Fay, Escudier and Hoult (1970) found a dependence on momentum ratio up to $M=1.2$, after which they suggest β would be constant. There are also those, like Ooms (1972), who suggest the entrainment coefficient should vary over the path of a plume, changing for the vertical and horizontal portions of plume rise.

In this thesis the entrainment coefficient will be varied as a function of the momentum ratio. The reason for varying β with momentum ratio is that as M increases, more of the rise of the plume is near vertical (θ in Figure 2-1 goes towards 90°) and β will be smaller, so introducing a dependence on M is a simple way of varying trajectory averaged β . To support this assumption, Figure 6-1 illustrates how using constant β is inaccurate. The momentum ratios examined ($M=4.0$, 6.0 and 8.0) are cases where downwash is negligible so the effects of the entrainment coefficient on the trajectory can be seen. In Figure 6-1 the trajectories of plumes with no downwash correction and $\beta = 0.6$ are plotted. It is clear that the assumption of constant β causes overprediction of the trajectory at $M = 4.0$ and underprediction for $M = 6.0$ and $M = 8.0$.

To determine the entrainment coefficient dependence on momentum ratio, β

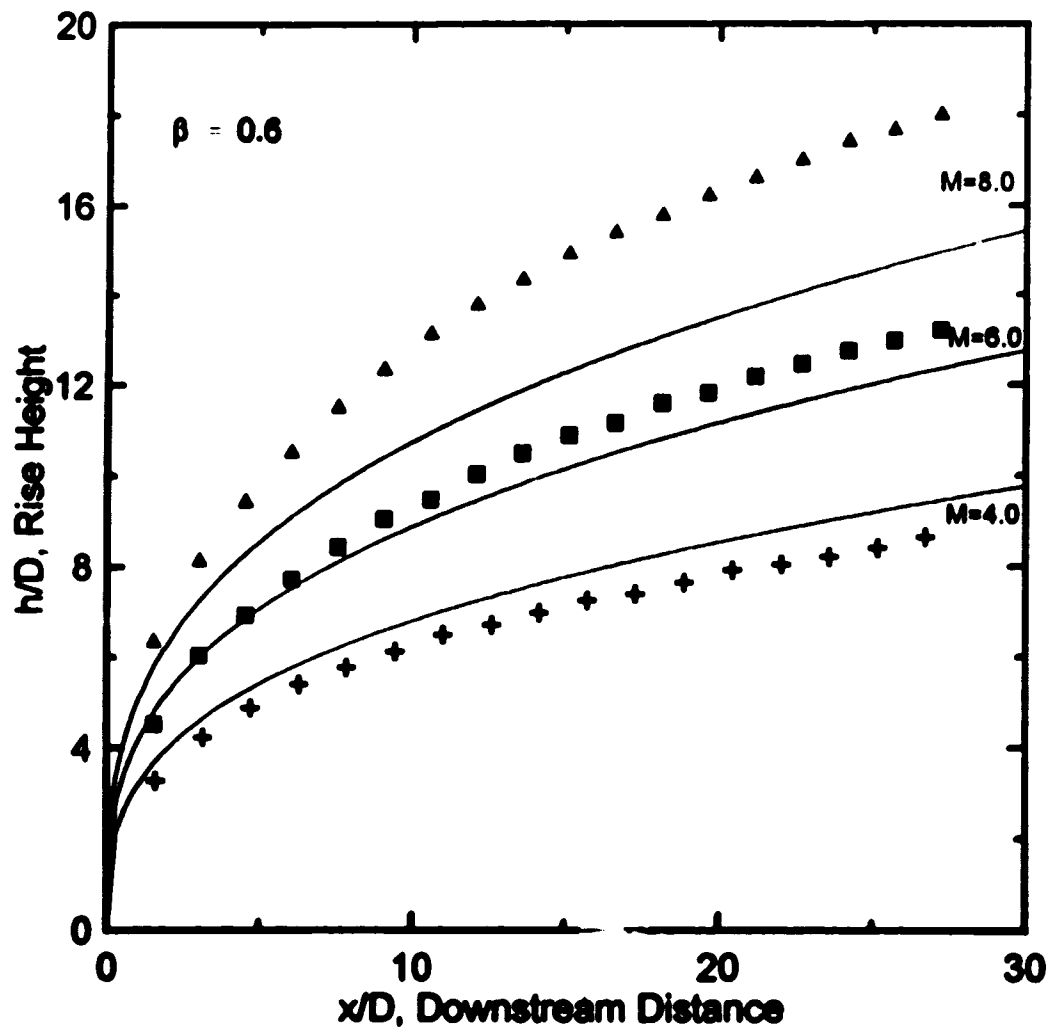


Figure 6-1: Comparison between experimental data and plume rise equation (Equation 2-5) with a constant entrainment coefficient, $\beta=0.6$, for $M = 4.0, 6.0$ and 8.0 .

was varied so the theoretical predictions for $M = 4.0$ to 8.0 , matched the experimental data. A function was fit to these values of entrainment coefficients assuming the maximum and minimum entrainment coefficients would be 0.8 and 0.3 . Figure 6-2 is a plot showing the entrainment data and the function used to predict β

$$\beta = 0.8 \left(\frac{1 + 0.015M^2}{1 + 0.04M^2} \right) \quad (6-1)$$

This function was found by an empirical fit, however varying β is supported by other studies, shown on Figure 6-2.

Table 6-1: Entrainment coefficients from various studies over a range of Momentum ratios

Reference		β	M_{\max}	M_{\min}	Lab/ Field	Buoyant/ Momentum
Hoult, Fay and Forney (1969)	■	0.90	4	4	Field	Buoyant
Hoehne and Luce (1970)	+	0.40	71	13	Lab	Momentum
Overcamp and Hoult (1971)	◆	0.78	1.5	0.02	Lab	Buoyant
Ooms (1972)	▲	0.50	8	8	Lab	Buoyant
Hoult and Weil (1972)	✕	0.60	10	3	Lab	Both
Davidson and Slawson (1982)	▲	0.63	2	2	Field	Buoyant

For example, Hoehne and Luce (1970) performed an experiment on buoyant releases where the values of the momentum ratio ranged from about 13 to 71. Their results indicated the entrainment coefficient approached 0.4 as the momentum ratio increased to 71. Overcamp and hoult (1971) predicted an entrainment coefficient of 0.78 for mometum ratios ranging from 0.02 to 1.5. For this model the choice of the asymptote of 0.3 was based on the Hoehne and Luce data, but was lower to produce a smooth fit through the data in this study. A linear fit was also made, and the equation $\beta = -0.05 + 0.81M$ was found to fit the data. However, Equation 6-1 was used because it fit the data and asymptotic boundaries as one continuous smooth

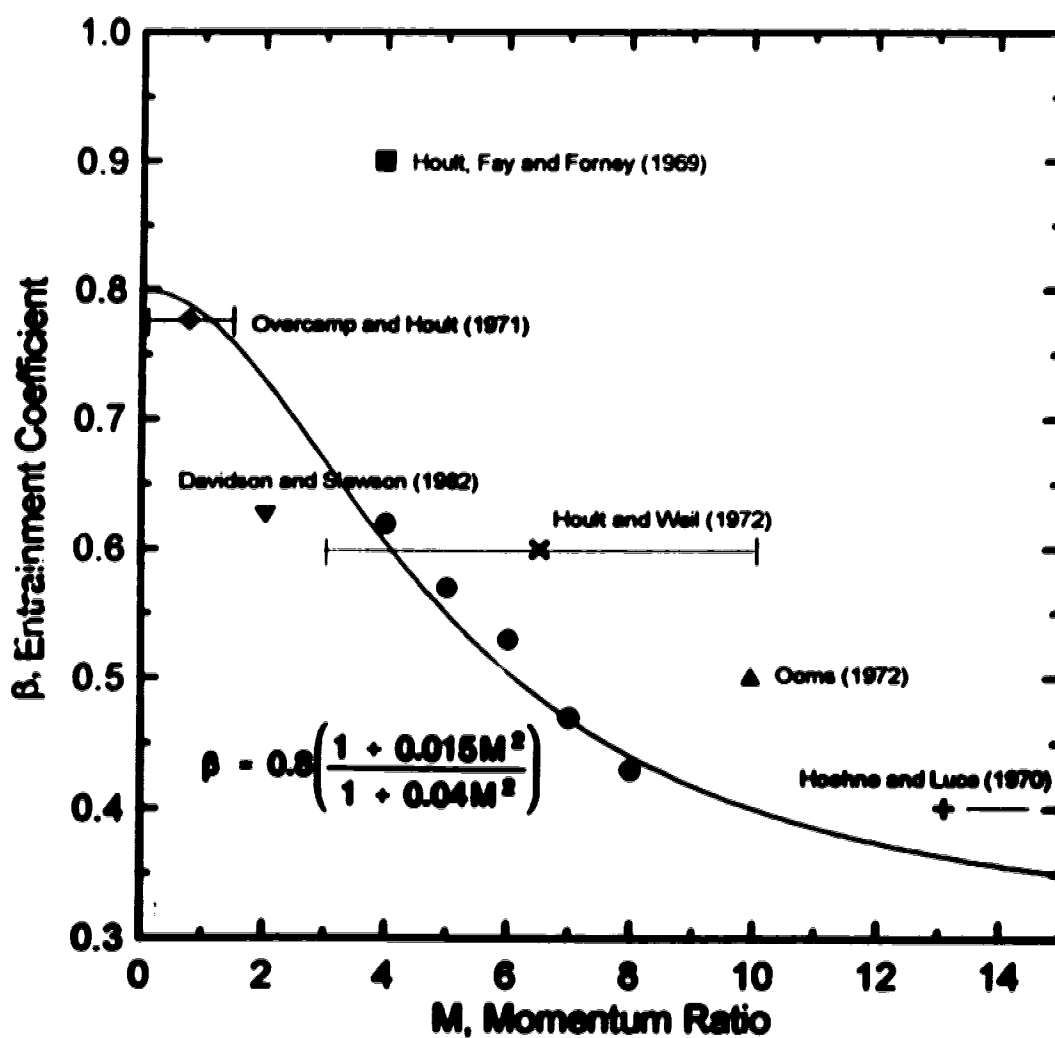


Figure 6-2: Variation of entrainment coefficient with momentum ratio for this study (circles) compared to entrainment coefficient from other studies (Described in Table 6-2).

curve. Figure 6-3 shows the predicted trajectories with the entrainment coefficient varying as Equation 6-1. Comparing Figure 6-1 and Figure 6-3 supports the assumption of varying the entrainment coefficient with the momentum ratio.

6.2.1 The Fully-Bent Over Assumption for Non-Buoyant Plumes

To determine how close to the fully bent-over assumption the plume in this thesis came, the point at which the plume path was tangent to 45° was determined for $M = 3.0$ to $M = 8.0$. From Equation 2-39, an expression for dh_m/dx (which is $\tan\theta$, where θ is the angle with the horizontal shown in Figure 2-1) was determined.

$$\frac{dh_m}{dx} = \left(\frac{1}{9\beta^2} \frac{F_m}{U_a} \right)^{1/3} \frac{1}{x^{2/3}} - (1-n) \frac{B_3}{D^{1-n}} \frac{1}{x} \quad (6-2)$$

Using Equation 6-2 the downstream distance at which the plume reached 45° was found and the corresponding rise height determined. As Table 6-2 indicates, at $M = 3.0$ the plume had completed 58% of its total observed rise by the time it has bent over to 45°. The amount of rise to reach 45° increases as the momentum ratio increases. A plume with $M = 8.0$ reached 85% of the total observed rise before it bent over to 45°. Since the $M = 3.0$ plume spends less of its rise vertical and more bent-over than the $M = 8.0$ plume it is clear an $M = 3.0$ plume would require a larger entrainment coefficient than a $M = 8.0$ plume, supporting the concept of a variable entrainment coefficient.

Table 6-2: Vertical vs. Fully Bent-Over Portions of Trajectory.

Momentum Ratio	Fraction of Total Measured Rise with $\theta < 45^\circ$
3.0	0.582
4.0	0.620
5.0	0.717
6.0	0.755
7.0	0.812
8.0	0.858

The fully bent-over assumption would be appropriate for a buoyant, low-momentum plume, rather than a non-buoyant jet. A buoyant plume emitted with a small vertical velocity would be carried down stream at the ambient velocity and rise

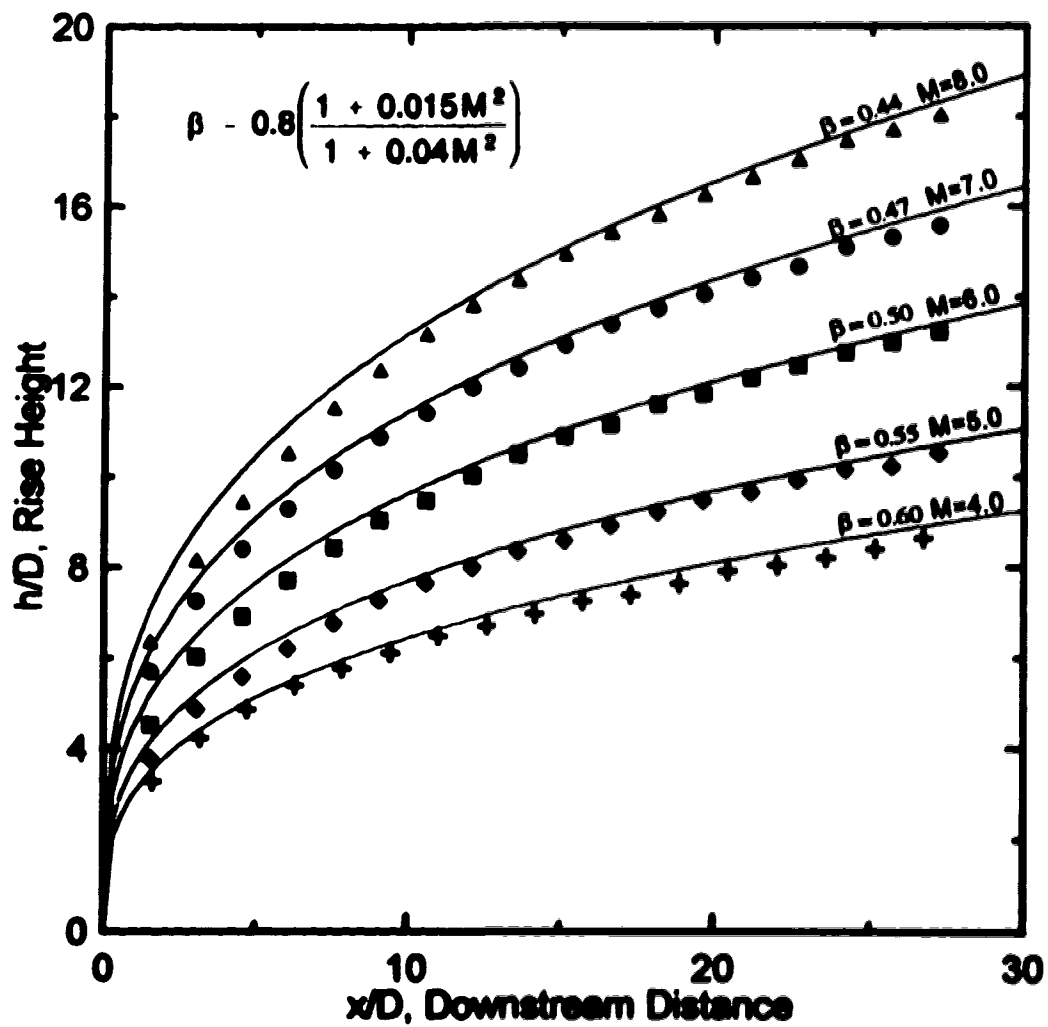


Figure 6-3: Comparison between experimental data for high momentum ratio plumes and momentum plume rise equation (Equation 2-5) using variable entrainment coefficient.

vertically only due to buoyancy. The plume would be fully bent-over for the entire rise and the entrainment coefficient would tend to $\beta > 0.6$. The assumptions used to derive the plume rise equation are more appropriate for a buoyant plume than for a momentum jet, making it surprising the plume rise equation predicts the path of a momentum jet as accurately as it does in Figure 6-2.

6.2.2 Added Mass Acceleration Effects on the Entrainment Coefficient

Dilution predictions often over-predict dilution when the entrainment coefficient for matching trajectory is used. The concept of added mass is used in several plume rise models to compensate for that problem. The added mass approach multiplies the effective mass in a plume cross-section of length dx , by a factor $(1 + f)$ to account for the force required to displace ambient fluid as the plume accelerates vertically. This added mass approach has been used by Escudier and Maxworthy (1973), Briggs (1975), Weil (1988) and Davidson (1989) in their derivation of the plume rise equations. If the fully bent-over plume is modelled as a solid circular cylinder rising with its axis parallel to the wind, potential flow theory predicts that the added mass will simply be the mass of ambient fluid displaced by the plume. The added mass factor f , would be 1.0 for this case, essentially doubling the mass of the plume. In Davidson (1989) the plume rise equations are derived including the added mass where the result was expressed as a variation of the entrainment coefficient so,

$$\beta = (1 + f)^{1/2} \beta_{\text{dilution}} \quad (6-3)$$

Briggs (1975) suggested a value of $f = 1.3$, which means β would be 1.5 times larger than the entrainment coefficient needed for dilution. Using the added mass concept allows only one entrainment coefficient to be used for both trajectory and dilution predictions.

There is some question as to whether this concept is physically realistic. For a fully bent-over plume, an analogy for the application of added mass is a log rising in water. As a log rises it will accelerate due to buoyancy. Fluid will be pushed out of the way and an added mass term would be necessary. However, a plume is not solid and there are no boundary conditions on the plume surface forcing fluid to flow around the plume. In the fully bent-over stage of rise it is entraining more fluid than is swept aside and it is possible that very little fluid is moved aside. Fluid would be entrained into the plume, where it would be directly accounted for by the vertical momentum balance. Therefore, the added mass concept should be viewed with

scepticism.

6.3 Virtual Origin Downwash Correction

It is apparent in Figure 6-4 that the predictions of rise when downwash is occurring require some correction, due to large discrepancies between predicted and actual rise. The difference between the predicted and actual rise are greatest for the lower momentum ratios, since downwash affects these cases most. Equation 2-13 presented by Briggs (1973) is a simple empirical correction for downwash. Briggs' virtual origin correction attempts to compensate for downwash by adding a displacement at the origin of the plume. The virtual origin model has no correction for downwash above $M = 1.5$, the momentum ratio which Sherlock and Stalker (1941) first suggested as the downwash cut-off.

Figure 6-5 shows the predicted trajectories when Briggs' virtual origin correction is used. This virtual origin reduces the rise of plume but does not alter the plume rise function. Since the plume rise function is not altered, the predicted trajectories always rise, never descending. The data in Figure 6-5 clearly show the plume descends for highly downwashed plumes. Briggs' correction assumes downwash effects can be lumped into one correction applied at the source.

The effects of downwash appear to be felt far downstream of the source, as the data in Figure 6-5 and Snyder and Lawson's (1991) data indicate, showing some plume trajectories continuing downwards even at 30D downstream. We concluded that the virtual origin correction is very limited in its ability to accurately predict downwash.

6.4 Initial Entrainment Downwash Correction

The second model for comparison is the initial entrainment model. This model's key assumption is that when downwash occurs a large quantity of ambient fluid is entrained into the plume close to the stack. Again the model assumes the effects of downwash can be lumped into one initial correction. It is accounted for by defining a new plume radius, R_p . This radius is determined by a balance of the source mass flux and the added initial entrainment to the bent-over mass flux, where the plume is carried at speed U_p .

This model has advantages over Briggs' empirical correction in that it alters the shape of the plume trajectory. The variable in determining the amount of downwash in this model is the ratio Q_d/Q_s . This ratio can be interpreted to represent the

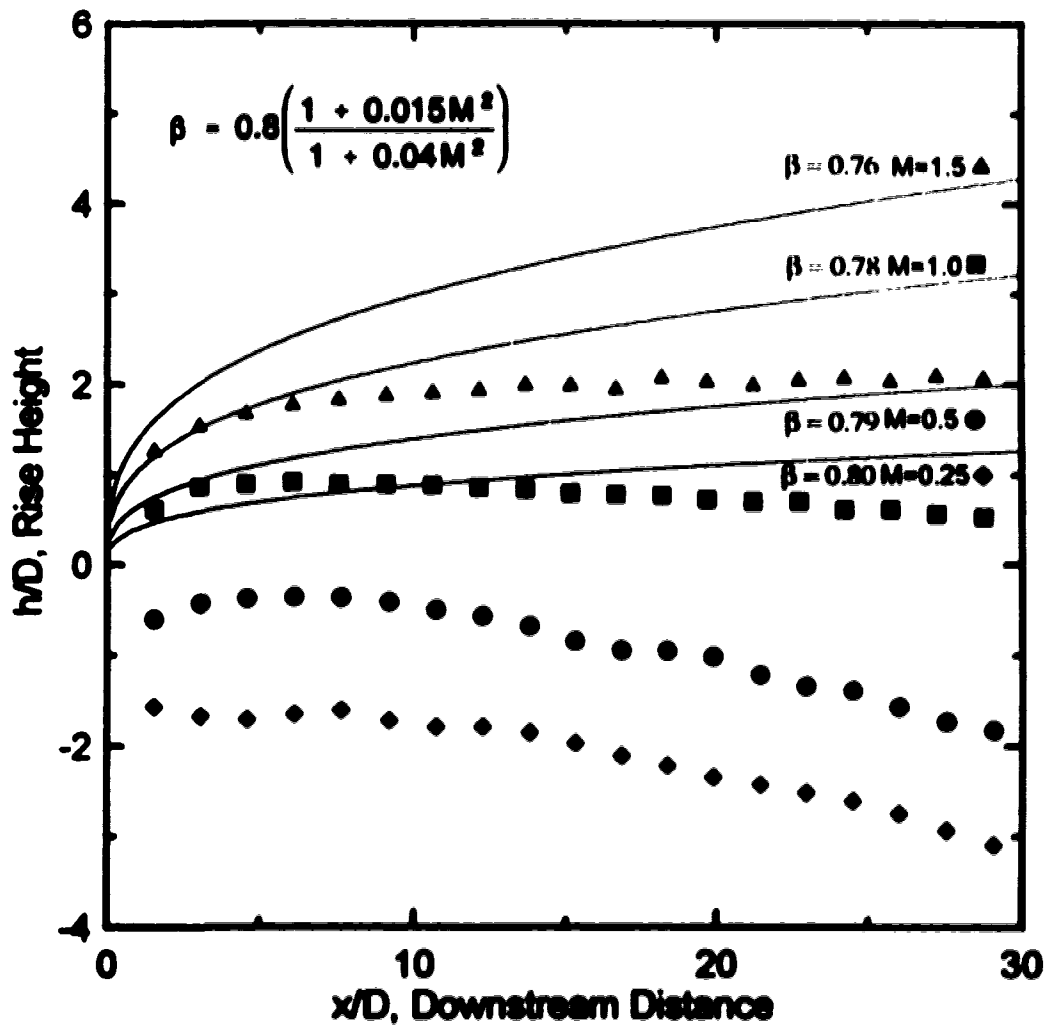


Figure 6-4: Predicted plume trajectories with no downwash correction (Equation 2-5) and corresponding experimental data for $M=0.25$ (diamonds), 0.5 (circles), 1.0 (squares) and 1.5 (triangles).

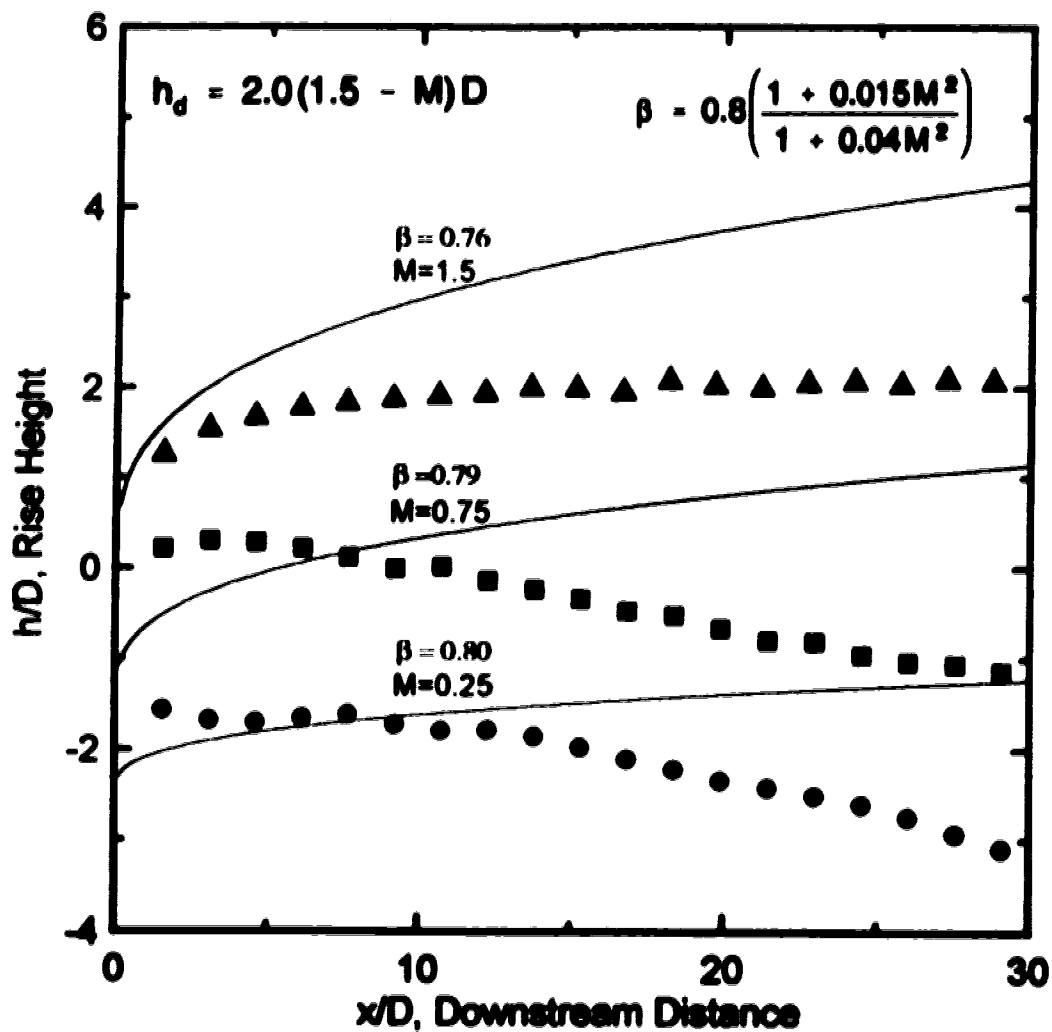


Figure 6-5: Predicted plume trajectories (Equation 2-5) using Briggs' downwash correction and corresponding experimental data for $M=0.25$ (circles), 0.75 (squares) and 1.5 (triangles).

amount of initial dilution the plume experiences when downwashed. Figure 6-6 compares the plume trajectories this model predicts. It is apparent the high downwash cases are not accurately predicted. The large initial dilution simply forces the plume, for $M < 0.75$, to remain level. For the cases of $M > 1.0$ the trajectory is more closely approximated, but still under-predicts most of the rise of the plume.

Perhaps the most critical downfall of the initial dilution model is that, as shown in Figure 6-6, the predicted trajectories never fall below $z = 0$. Since the data clearly indicates descending trajectories, the initial dilution model is not suitable for predicting downwash.

6.5 Downwash Velocity Correction

The final model for comparison is the downwash velocity model. The downwash velocity model is based on the existence of a time averaged tip vortex pair aligned in the streamwise direction from the stack tip. The plume experiences the downwash velocity produced by this vortex pair. As described in Chapter 2, a key assumption in the development of this model is that the separation between the two vortices increases at a rate equal to the growth of the stack wake width and that the influence of the vortex pair acts along the entire path of the plume. In this model, it is assumed that a jet emerging from the stack disrupts the vortex pair, causing a reduction in the vortex strength, Γ_d . It is then reasonable to assume, as a first approximation, that the downwash correction coefficient, B_3 , would be a function of the momentum ratio.

The function for B_3 was determined experimentally for two separate cases, constant entrainment coefficient and variable entrainment coefficient. Figure 6-7 shows the function chosen for B_3 when entrainment was assumed constant at $\beta = 0.6$. The function seems to fit the coefficients for low momentum ratios, but is poor at matching B_3 at higher M values ($M > 4.0$). This is another subtle suggestion that β should not be a constant.

Figure 6-8 shows the downwash velocity models predicted plume trajectories using $\beta = 0.6$ and the downwash correction coefficient shown in Figure 6-7. The predicted trajectories are better than the other models, but using a constant entrainment coefficient seems to under or overpredict the trajectory for certain momentum ratios. The trajectory for $M = 0.25$ is overpredicted, which suggests $\beta = 0.6$ models to little entrainment into the plume, and the trajectory for $M = 6.0$ and 8.0 is underpredicted, which suggests $\beta = 0.6$ models to much entrainment. The

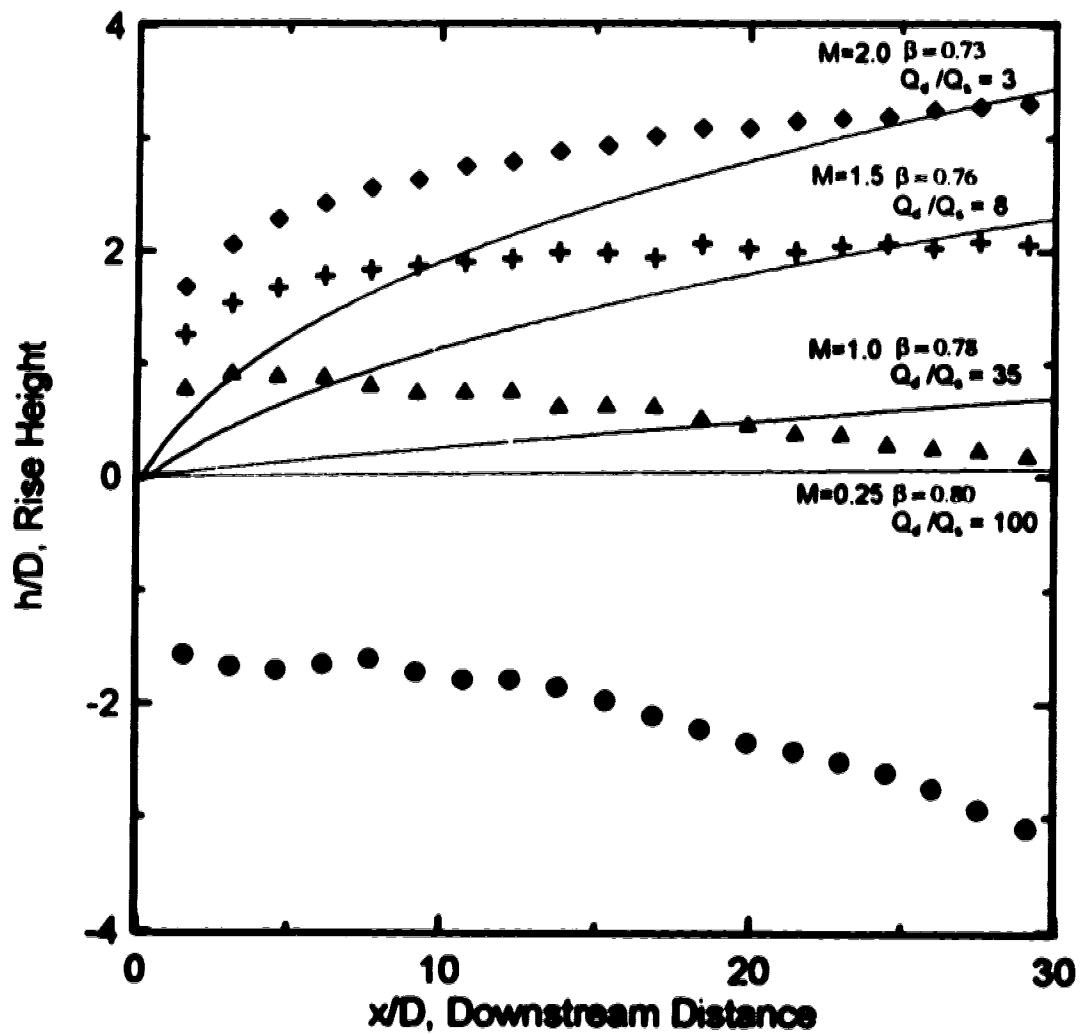


Figure 6-6: Initial entrainment downwash model predictions (Equation 2-16) for $M = 0.25$ (circles), 1.0 (triangles), 1.5 (pluses) and 2.0 (diamonds).

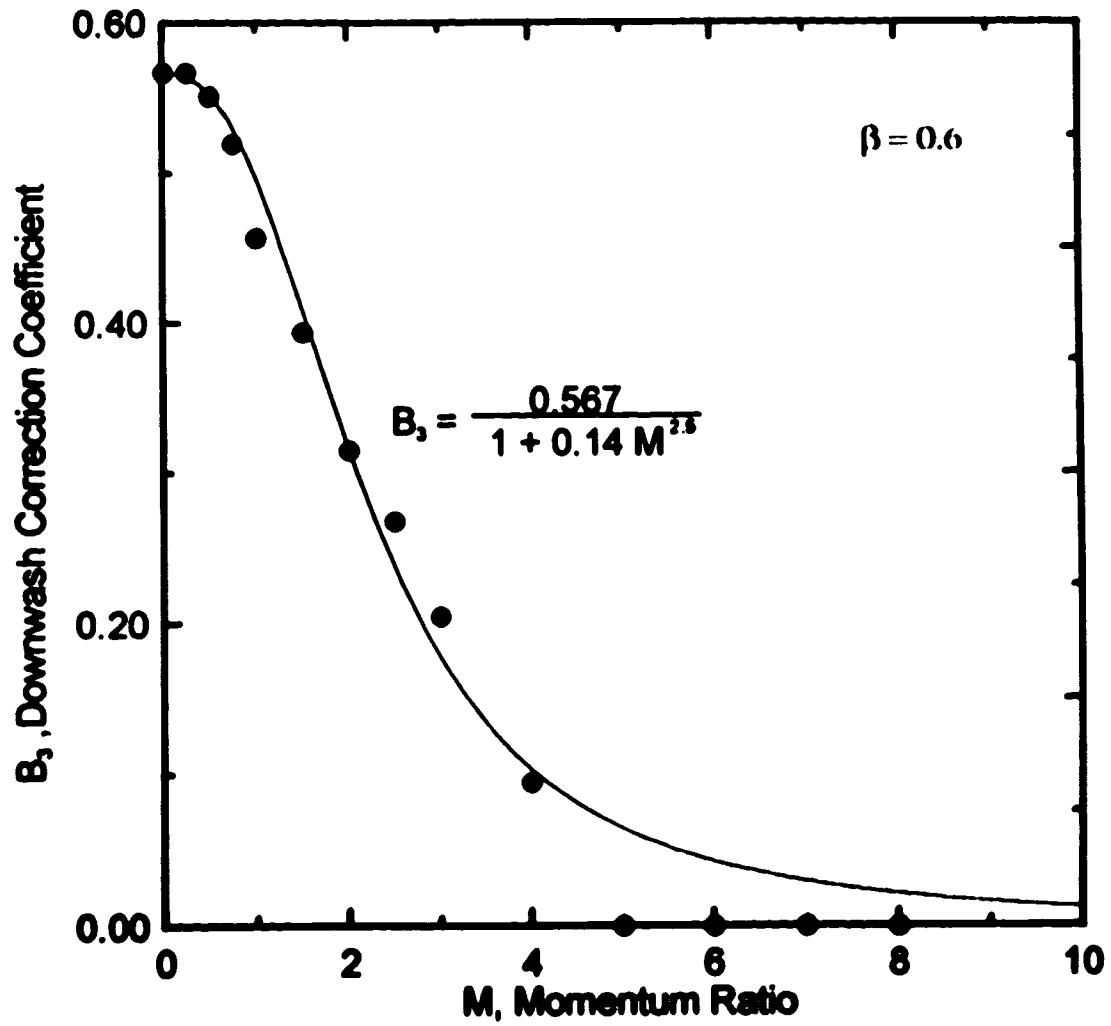


Figure 6-7: Downwash correction coefficient for a constant entrainment coefficient, $\beta = 0.6$.

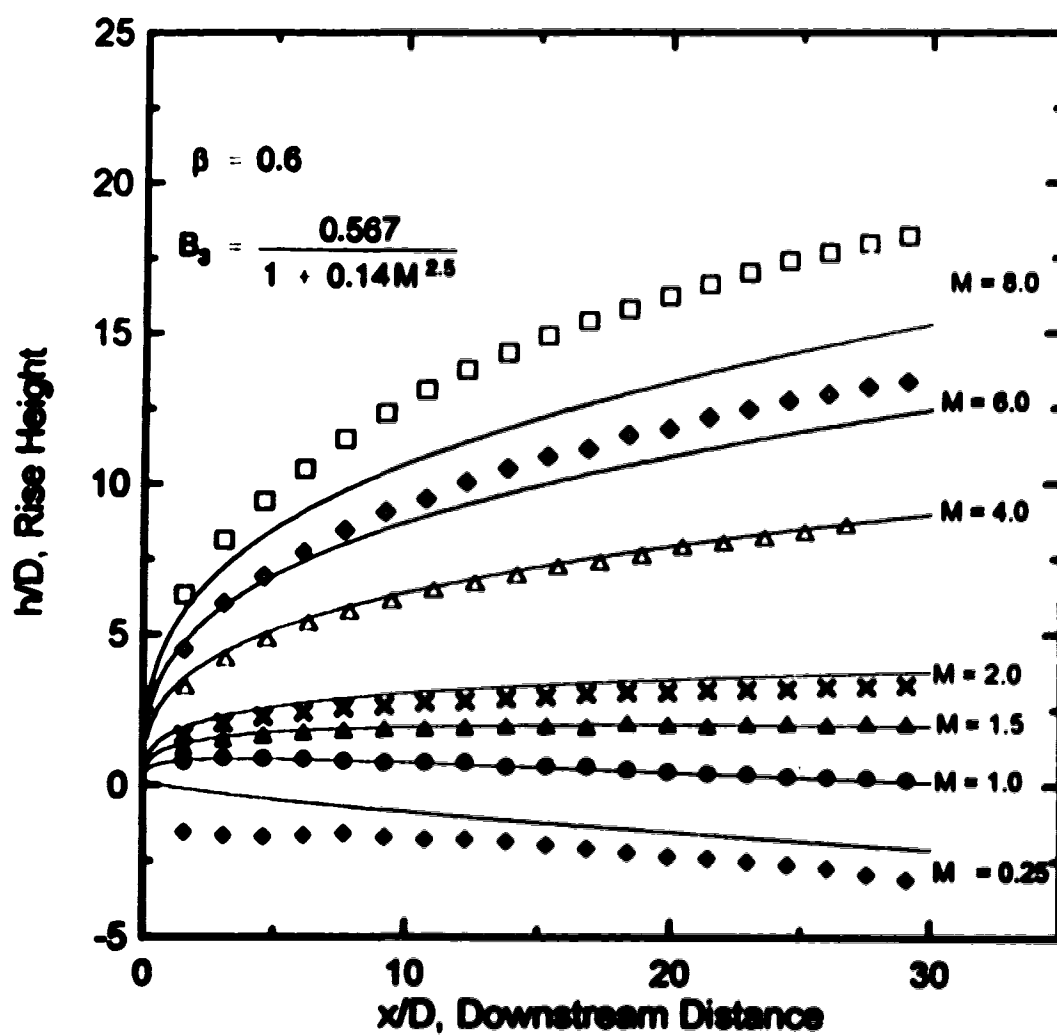


Figure 6-8: Predicted stack plume trajectories (Equation 2-39) using the downwash velocity model for a constant entrainment coefficient, $\beta = 0.6$.

conclusion which can be drawn from Figure 6-8 also supports the use of a variable entrainment coefficient.

The second case was for a variable entrainment coefficient. The function chosen for the downwash correction coefficient for a variable entrainment coefficient is shown in Figure 6-9. The function chosen to describe the downwash correction coefficient was

$$B_3 = \frac{0.567}{1 + 0.38M^2} \quad (6-4)$$

The downwash correction coefficient follows a much smoother and continuous path using plume rise with a variable entrainment coefficient, β from Equation 6-1. At high momentum ratios $M > 8.0$, the function, B_3 , will predict downwash coefficients which will be small compared to the rise and the error between measured B_3 values and the approximation of Equation 6-4 is negligible. For example, at $M = 8$ the downwash correction coefficient would be 0.022, thus, at 30 diameters downstream the downwash correction, h_d , would be 0.169D. The plume would have risen 18D, producing an error of 0.94%, easily neglected.

The downwash correction coefficient could not be determined directly from Equation 2-36 because the circulation of the streamwise vortex pair would be very difficult to determine. Since the vortex pair is time averaged an accurate determination of the total circulation is prohibitively difficult. While Equation 2-36 does not include any direct dependence on momentum ratio, changes in the vortex structure at high momentum ratios, shown in the flow visualization image of Plate 4-4, should produce a momentum ratio dependence. The high velocity jet appeared to effect the connection of the vorticity, so that the vortex street connected into the plume, shown in Plate 4-4. This new connection changed the horizontal orientation of the vortex pair to be more vertical which would reduce the downwash velocity and present a possible momentum ratio dependence.

Using the coefficient B_3 given by Equation 6-4, the downwash velocity model could be used to predict plume trajectories. Figure 6-10 shows the comparison between the experimental data and the downwash velocity model trajectory predictions for variable β rise. There are several key points illustrated by this figure.

First, the downwash velocity model predicts the trajectories of the plumes quite closely over the entire range of momentum ratios, unlike the virtual origin and

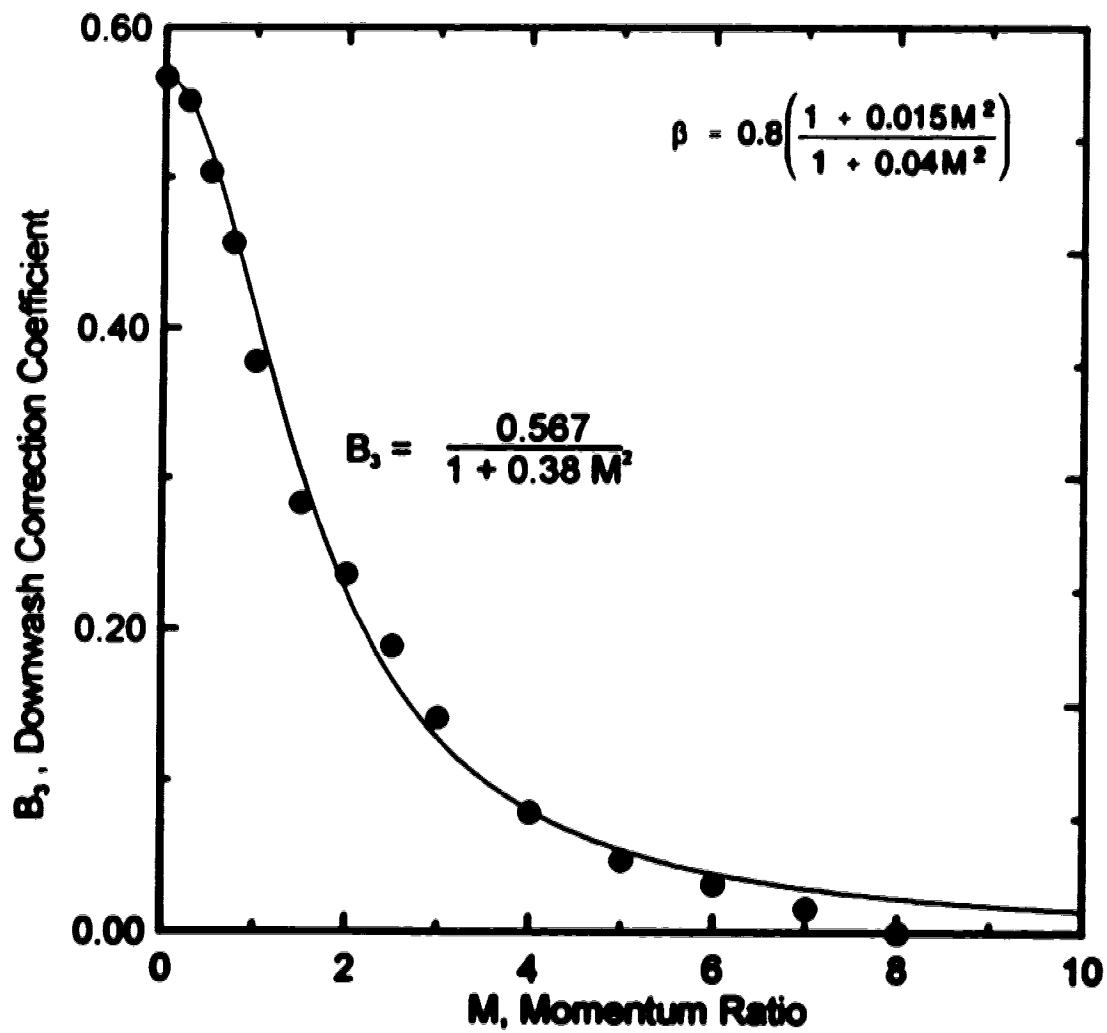


Figure 6-9: Downwash correction coefficient for variable entrainment coefficient.

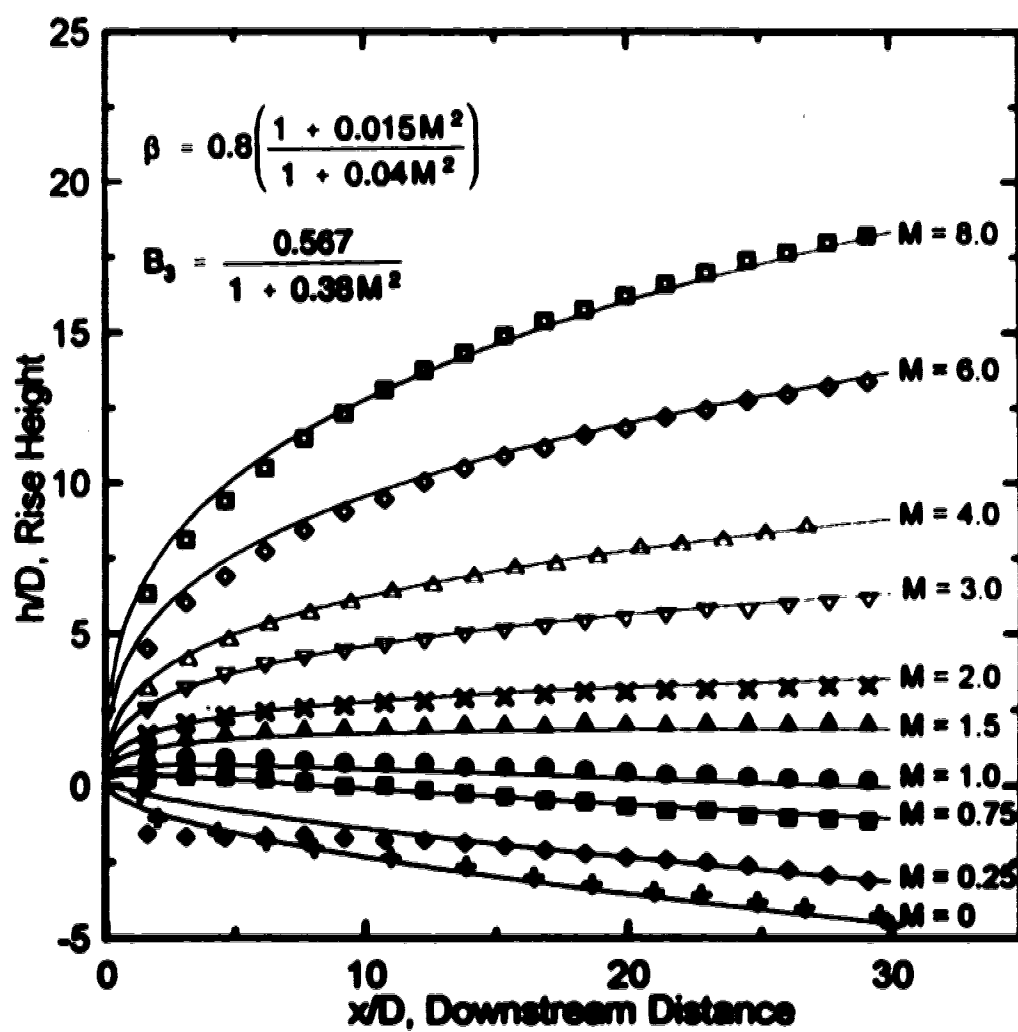


Figure 6-10: Predicted stack plume trajectories (Equation 2-39) using the downwash velocity model for variable entrainment coefficient.

initial entrainment models. The downwash velocity model is able to predict descending trajectories as well as ascending trajectories.

One surprise was the accurate prediction of the trajectory for a plume with no exit momentum ($M=0$). No other data for this case were found in the literature on plume rise. The zero momentum case was simulated by placing a plug in the stack, applying fluorescein to the top of the plug and tracking the dye. The match of the trajectory and data were unexpected as the test of $M=0$ was done, primarily for interest, after the bulk of the plume rise data had been collected. It is important to note that the exact match within the first 10 diameters is probably not a real phenomenon but a result of the smearing of the dye in the y-z plane making the determination of the centroid difficult. However, after 10 diameters the error due to the visualization technique was negligible.

A second point is the obvious mismatch between the predicted trajectory and data in the first 10 diameters for $M = 0.25$. This underprediction by the downwash velocity model is probably due to the effect of the low pressure in the lee of the stack. At a momentum ratio of 0.25, some of the plume is stripped away immediately after release and recirculates in the low pressure region. This removal of material can be seen in Figure 6-11, a concentration profile of a $M = 0.25$ and 6.0 plume at $x = 2D$. The concentration profile at $M = 6.0$ is symmetric about the centroid, but the concentration profile of the $M = 0.25$ plume shows a large amount of material sucked down into the wake, which would effect the centroid. Another view of this is seen in Figure 6-12, a concentration contour plot of a y-z cross section of the plume at $M = 0.25$ at four downstream locations.

Figure 6-12a also illustrates the capture of plume material by the near wake recirculation, which would strongly influence the centroid at this position. Five diameters downstream, (6-12b), the effect of the wake recirculation is reduced, as shown by the smaller area inside the lowest contour line, but is still affecting the centroid. At the 10D position, (6-12c), the recirculation has little effect on the centroid of the plume and at 30D the entire plume has been downwashed to below the stack tip (6-12d). The effect of the stack recirculation region on downwash appears to be limited to $x/D < 10$ and to extremely low momentum cases.

Figure 6-13 and Figure 6-14 are similar contour plots for $M=1.5$ and $M=6.0$. For $M=1.5$, (6-13) downwash is still a consideration but the effect of the recirculation does not appear to be present. In the $M = 6.0$ case, (6-14), there is no downwash and contours show the natural tendency for a time averaged plume to take the a

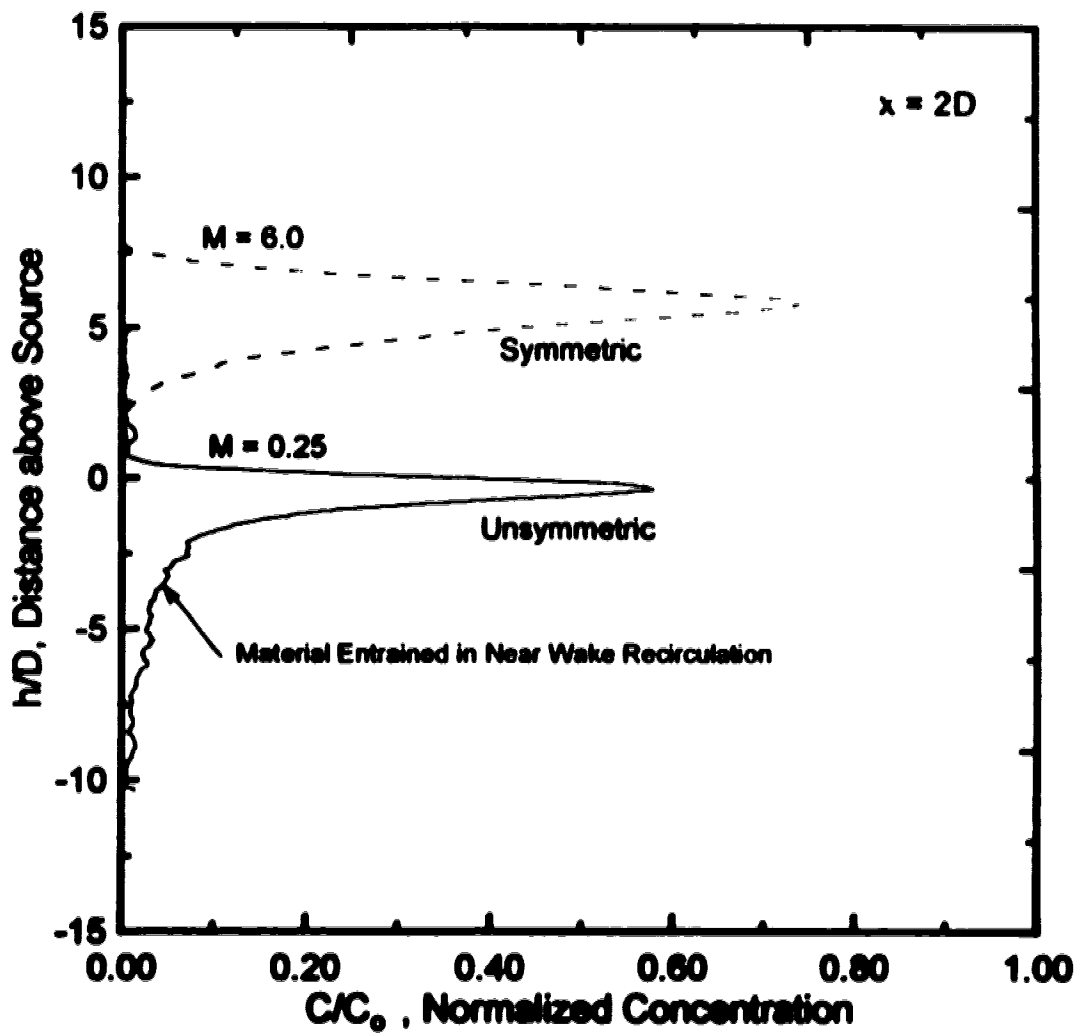


Figure 6-11: Measured concentration profiles at $x = 2D$ for plumes at $M = 0.25$ and 6.0.

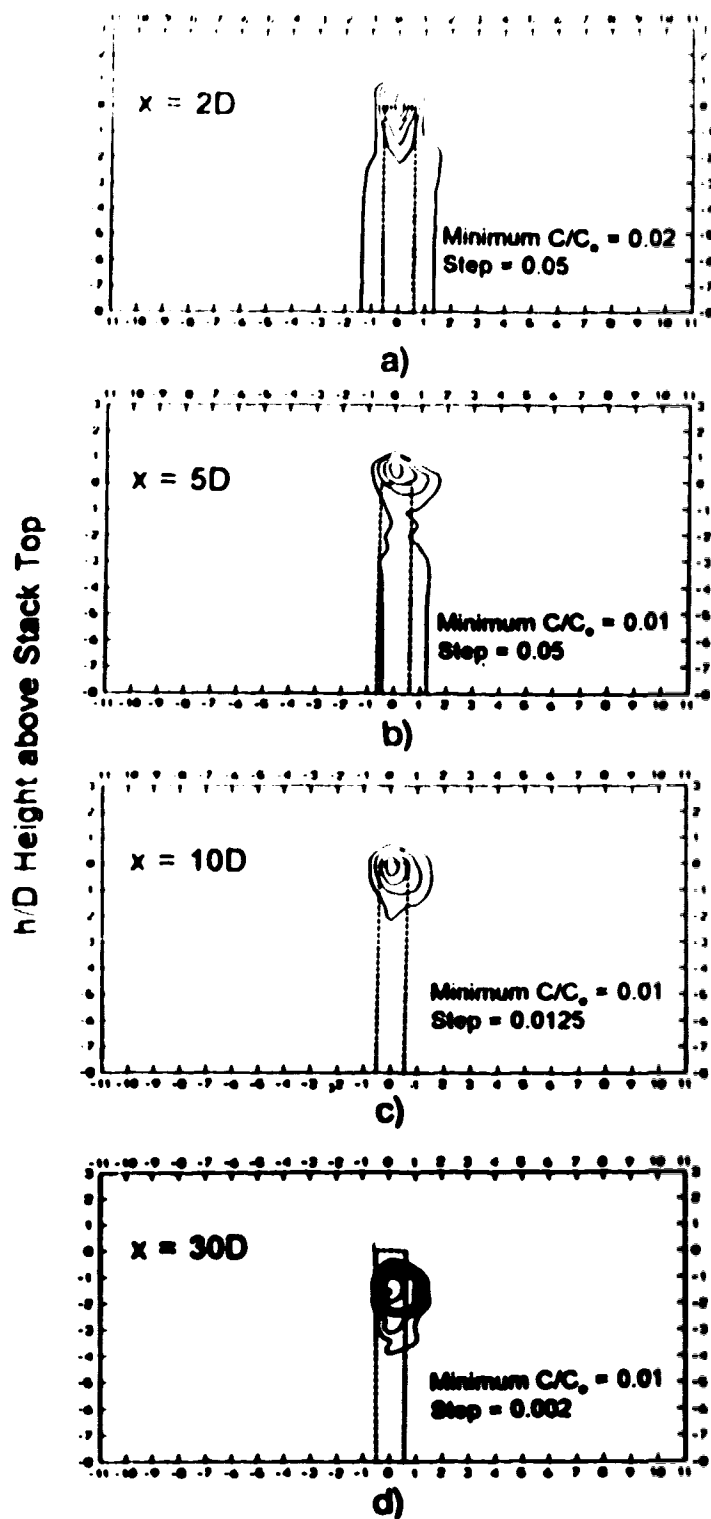


Figure 6-12: Plume cross section concentration contour plots (y-z plane) for $M = 0.25$ at $x = 2D$, $5D$, $10D$ and $30D$.

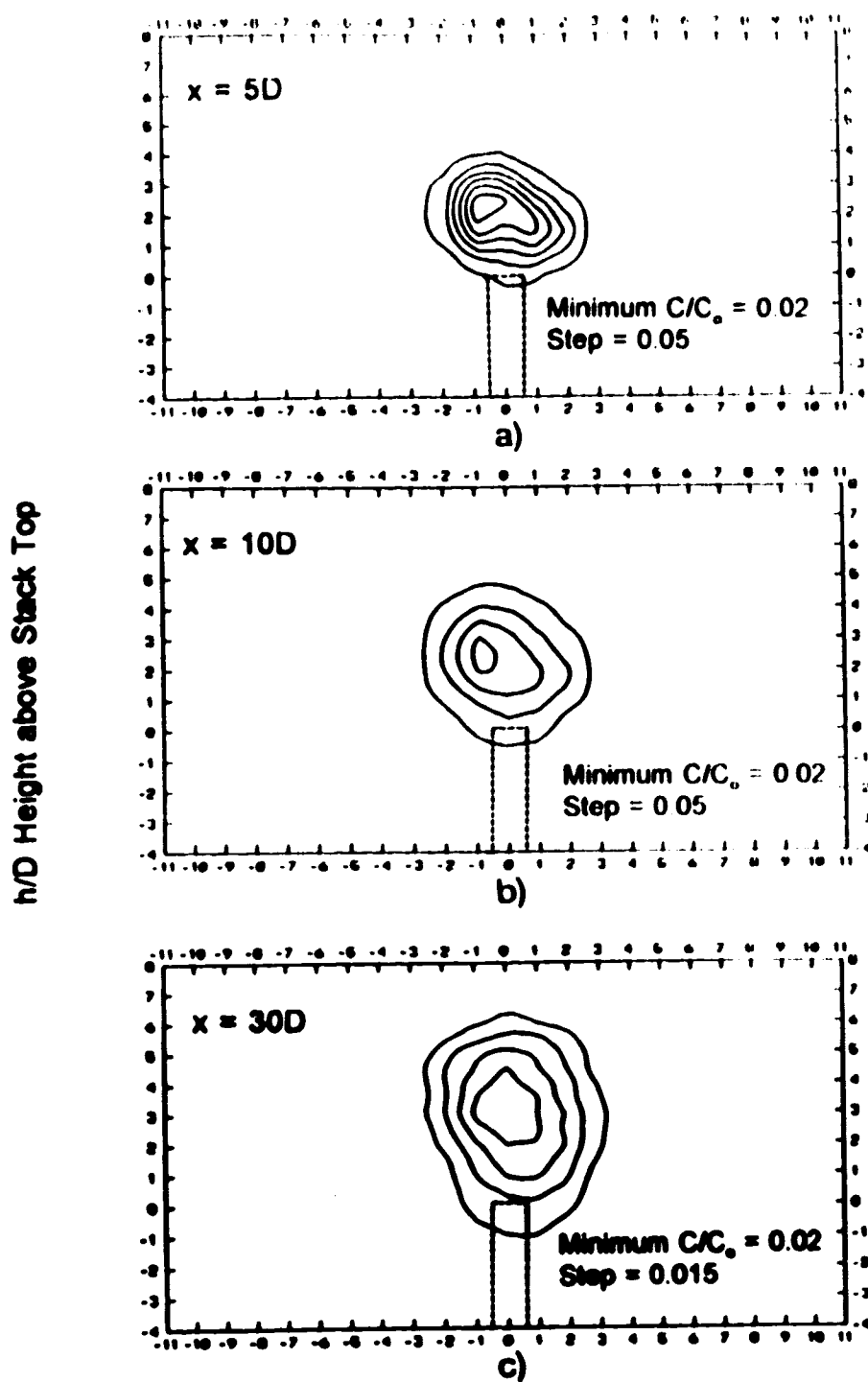


Figure 6-13: Plane cross section concentration contour plots (y - z plane) for $M = 1.5$ at $x = 5D$, $10D$ and $30D$.

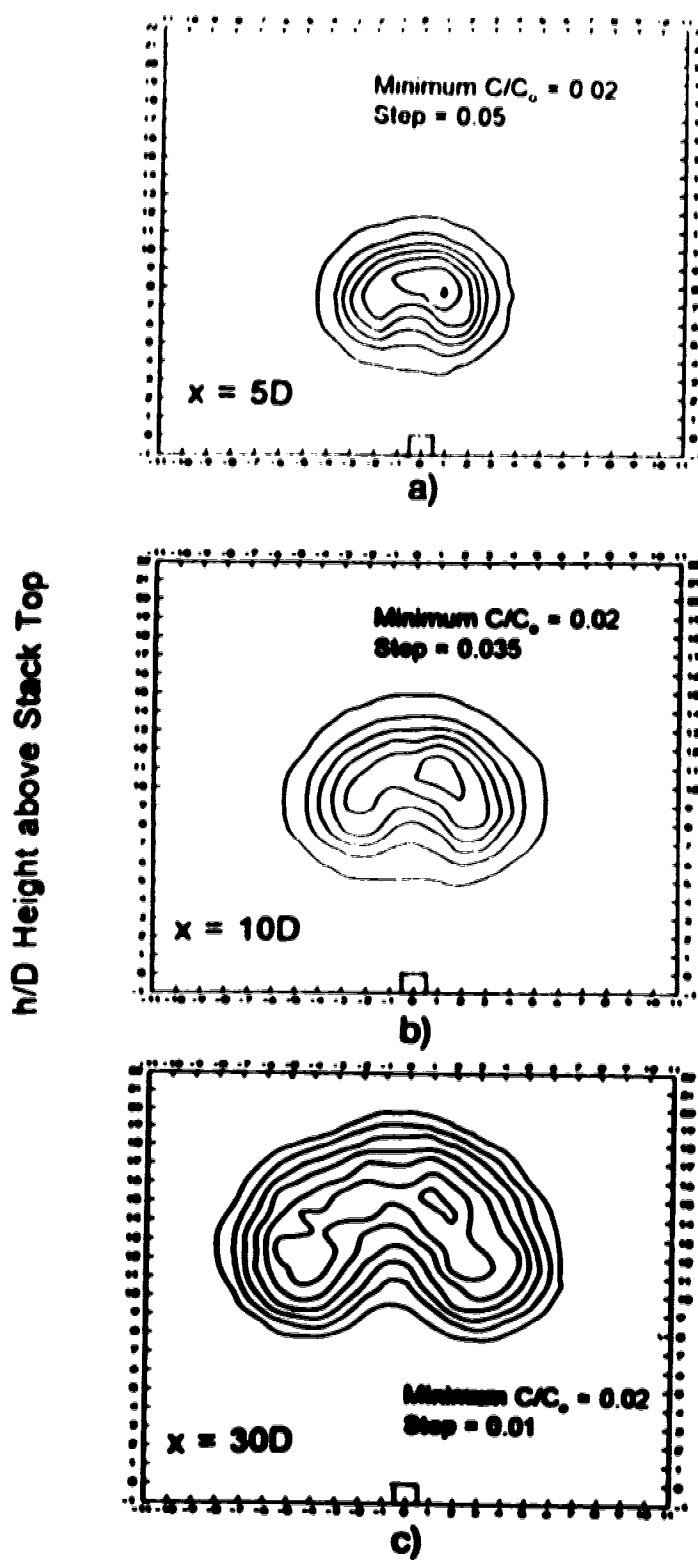


Figure 6-14: Plume cross section concentration contour plots (y-z plane) for $M = 6.0$ at $x = 5D$, $10D$ and $30D$.

kidney shape. This kidney shape is due to a plume vortex pair, distinct from the stack tip pair, which is established within the plume. The rotation of the in-plume vortex pair, opposite to the tip pair, causes the plume to suck fluid into the bottom and produce the unique shape. The absence of the kidney shape in Figure 6-13 might be caused by the tip vortex pair interacting with the plume vortex pair to reduce the in-plume circulation.

The images used to determine concentration centroids used for Figure 6-10 were vertical profiles from the x-z plane at the plume centerline. These sections cut the plume in the middle and produced a side view of the plume. A closer examination of Figure 6-14 c) suggests one possible problem with this method of determining rise height. Cutting the plume in the center means the centerline profile would be taken at the narrowest y-z cross section of the plume, as shown in Figure 6-14 c). The centerline profile would appear to be narrower than the plume's actual shape. To determine if this was a serious problem, centroids were determined for the y-z plane at 5D, 10D and 30D downstream and compared to the centerline trajectories. Figure 6-15 shows the comparison for various momentum ratios. The centroids from both streamwise and cross-stream sections match closely, suggesting the shape of the plume did not effect the measurement of the centroid. This also provided some verification that trajectories measured were correct, as even $M = 0.25$ matched in both cases.

6.6 Reynolds Number Effects on the Downwash Velocity Model

The flow around a cylinder can be placed into three categories based on Reynolds number, $Re_d = U_d D / \nu$. The first is the subcritical regime which exists for Reynolds numbers up to the lower transition of 2×10^5 . The second regime for cylinders is the supercritical regime. This extends from the lower transition point to an upper transition point which occurs around $Re_d = 3.5 \times 10^6$. In this region the boundary layer of the cylinder undergoes a transition from laminar to turbulent. The final regime is the transcritical regime, which exists at Reynolds numbers above the upper transition point. The effects of Reynolds number mismatch are a problem when modelling full scale flows with a prototype. The experiments in this study were conducted at a $Re_d = 1800$ (based on outside stack diameter), where full scale stack Reynolds numbers would be of the order of 10^6 to 10^7 . This presented a significant Reynolds number mismatch to be considered.

One major effect of the Reynolds number mismatch is the apparent change in

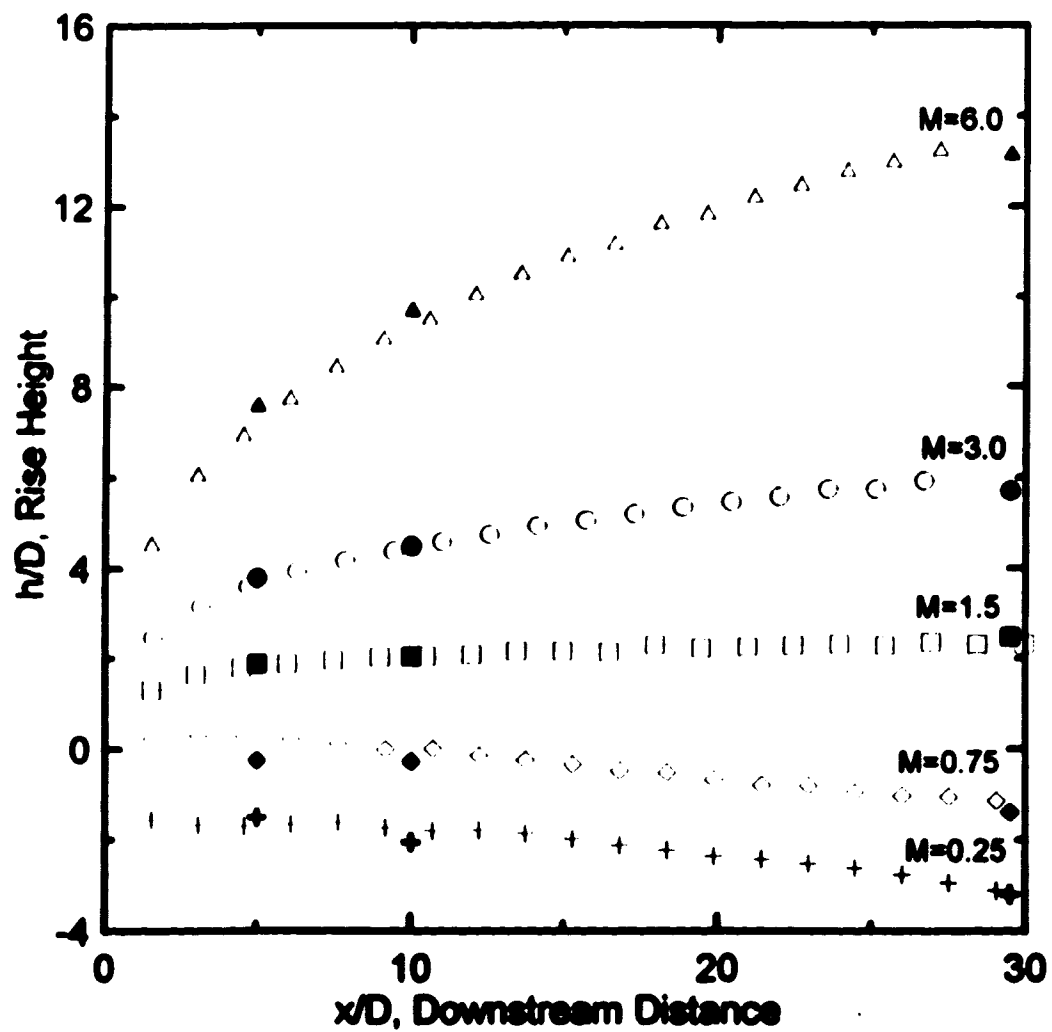


Figure 6-15: Comparison between centroids calculated using an x-z light sheet plane (empty symbols) and a y-z cross section (filled symbols).

rise height, h , between subcritical and supercritical Reynolds number flows. The transition from sub to supercritical flow occurs at about $Re_d = 2 \times 10^5$, according to Roshko (1960). Snyder and Lawson (1991) studied the difference in the rise of a plume in sub and supercritical flow and found significant differences. In their study, plumes released into subcritical flow had lower final rise heights and different trajectories than plumes in supercritical flow. No explanation for the difference was given and an empirical fit was used for the plume trajectories. The effects of downwash were still present in the supercritical case but the difference raises several concerns about modelling downwash.

To confirm whether the plumes in this study were exhibiting sub or supercritical behaviour, the downwash velocity model was compared to both sets of data from Snyder and Lawson's study. It was found that the downwash velocity model predicted the trajectories for the subcritical case; not surprising considering our experiments were preformed at subcritical Reynolds numbers. Figure 6-16 is a comparison of the downwash velocity model and Snyder and Lawson's data for several momentum ratios. The match of the model to subcritical data produced two key concerns:

- The form of B_j for the downwash velocity model is applicable to subcritical flow and but may not be directly applicable to full scale supercritical flows. What error is likely?
- What difference between the sub and supercritical flows would have to be incorporated into the model to predict trajectories for full scale flows?

The answer to these questions is not elementary. If the downwash velocity model does accurately explain the mechanism for downwash, then the real question is; how does the change from sub to supercritical flow change the influence of the stack tip vortex pair on the plume? To determine how operating in the subcritical, supercritical or transcritical flow regime effects downwash, the changes in base pressure coefficient, wake growth and vortex structure as the flow progresses from one flow regime to the next need to be examined.

6.6.1 Reynolds Number Effects on Base Pressure Coefficient

One important factor in downwash is the transition of the base pressure coefficient from laminar to turbulent flow around a cylinder. The trend of the base

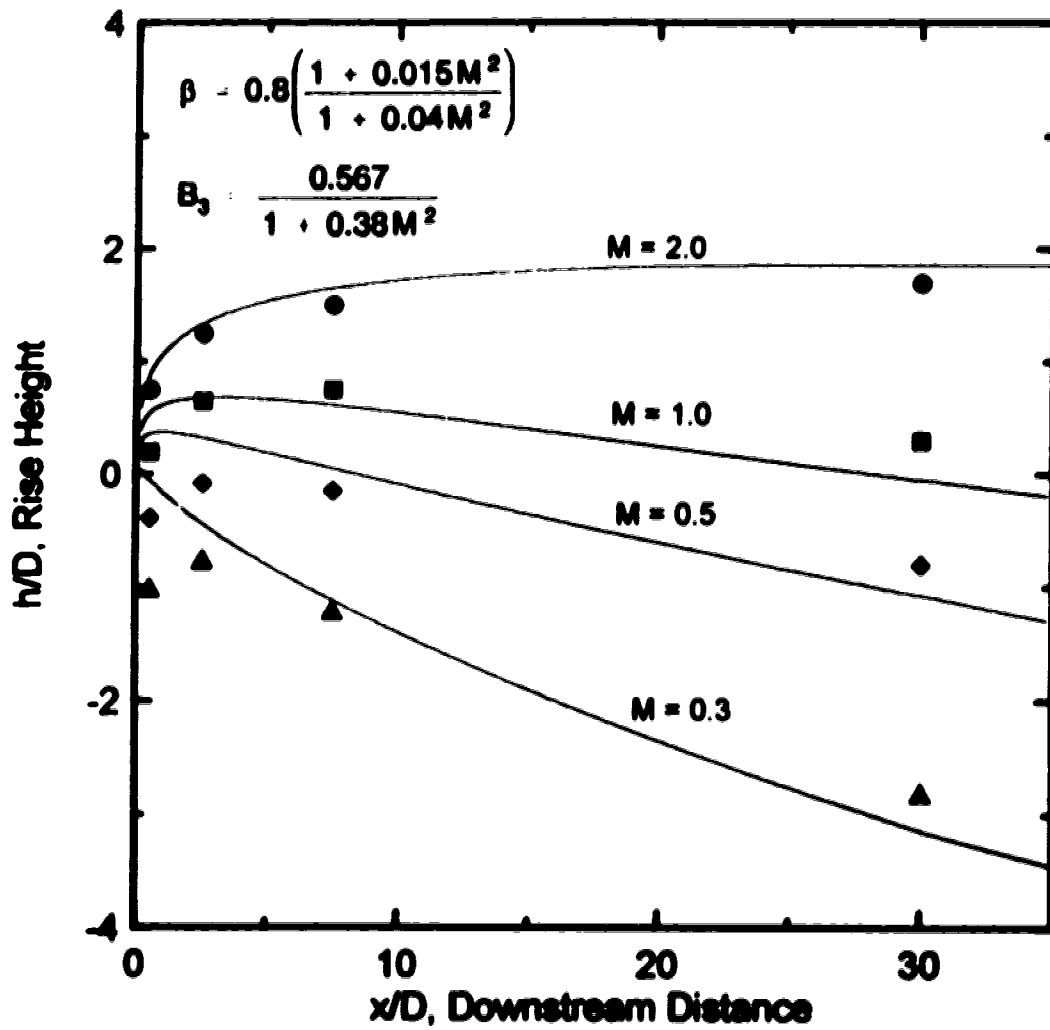


Figure 6-16: Downwash velocity model predictions (Equation 2-39) compared to Snyder and Lawson's wind tunnel data for subcritical Reynolds numbers.

pressure coefficient through the three flow regimes is a large negative coefficient for the subcritical flow ($-C_{pb} = 1.2$ to 0.8), sharply decreasing in the supercritical regime ($-C_{pb} = 0.2$) and then increasing in the transcritical regime, close to the range of subcritical values ($-C_{pb} = 0.8$ to 0.9).

Data plotted from Nieman (1979) in Figure 6-17 illustrates the trend of the base pressure coefficient over the full range of Reynolds numbers. The Reynolds number, $Re_d = 1800$, which this study was conducted at corresponds to a base pressure coefficient of about 0.85, measured from Figure 6-17. This value corresponds well with Roshko's (1960) prediction of a base pressure coefficient of 0.86 in the transcritical regime. This indicates that while the base pressure coefficient changes as the Reynolds number progresses through different flow regimes, this study matches the full scale value of base pressure coefficient.

6.6.2 Reynolds Number Effects on Wake Growth

A second factor important in downwash, which is also dependent on the Reynolds number is the size of the wake. In the subcritical regime the flow separates from the cylinder at an angle, measured from the stagnation point, of about 85° , as reported by Roshko (1960). The separation point for supercritical flow is moved forward on the cylinder to an angle of about 120° . The separation point for the transcritical regime is moved back, to an angle of about 80° , due to the stack boundary layer going turbulent earlier, according to Roshko (1960). Since the separation points for the subcritical and transcritical are at approximately the same angle, the wake which forms behind the cylinder will also be about the same size and grow at the same rate. In the supercritical regime the wake will be narrower than the other two cases because the separation point is further ahead. So again, the wake information presented in this study should be consistent with the conditions at full scale.

6.6.3 Reynolds Number Effects on Vortex Shedding

A third, and perhaps key factor, is the change in the vortex shedding from a cylinder for different Reynolds number ranges. There are several factors affecting vortex shedding, which will also effect downwash. In this section these factors will be discussed and the differences between the three flow regimes presented.

It is well known that the onset of vortex shedding begins at a Reynolds number of approximately 40 (Roshko (1960) and Chen (1972)). In the subcritical range the presence of a vortex street with a Strouhal number, $St = fD/U_\infty$, of about 0.2 was well

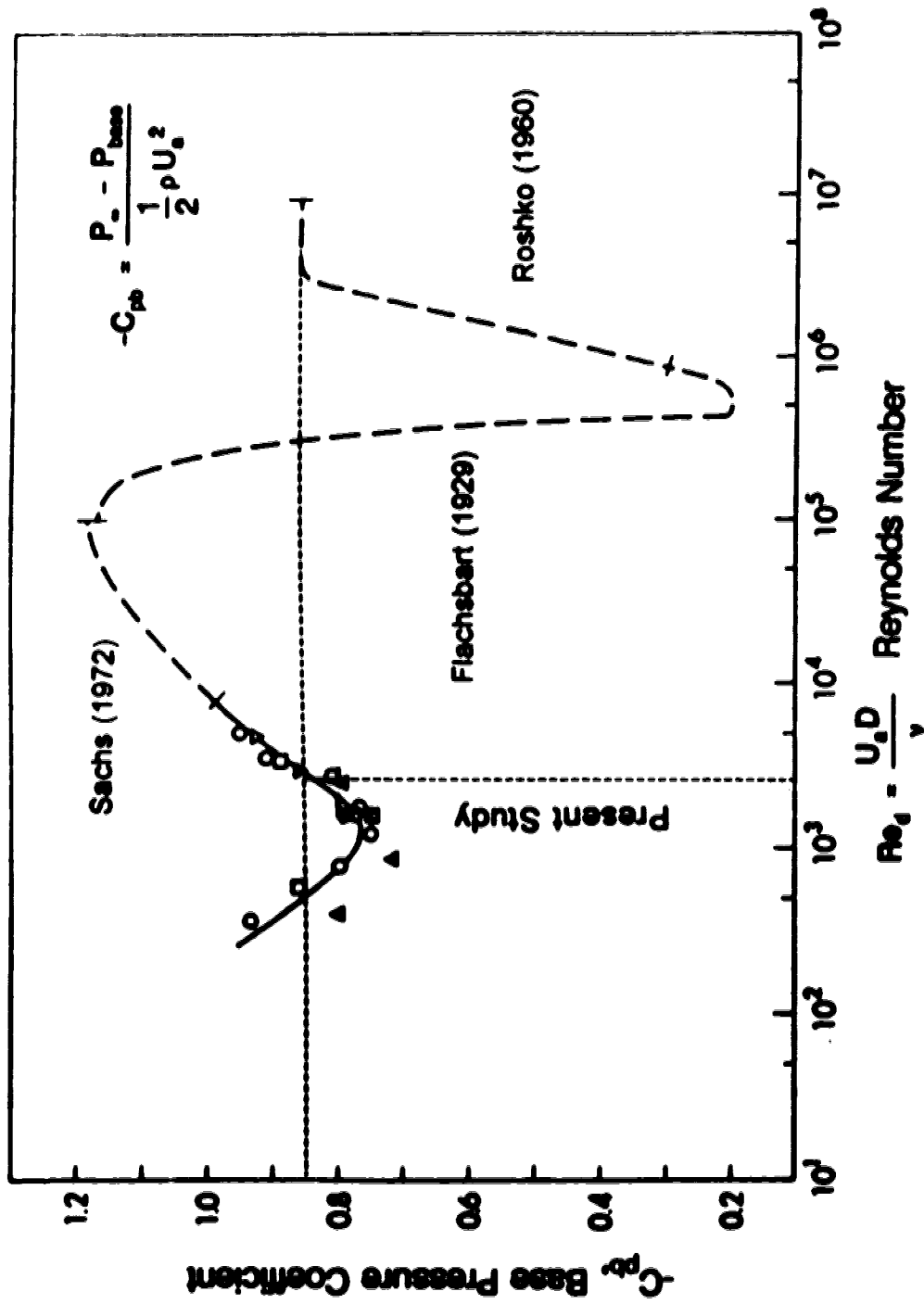


Figure 6-17: Base pressure coefficients for an infinite circular cylinder, from Neiman.

documented. The Strouhal number found for the vortex street in the present study was 0.19, very close to the established subcritical values. However, as suggested by Roshko (1960), very little is known about the vortex shedding for the super and transcritical ranges. These areas were very difficult to study in laboratories because the high Reynolds numbers could not be easily produced.

Since the time of Roshko's (1960) study, considerable more investigation has been done on vortex shedding from a cylinder, see Chen (1972), Guven, Farrell and Patel (1980) and Williamson (1989). For the downwash velocity model the key aspects concerning vortex shedding are the presence of a vortex street and the growth of the core of the vorticity.

The presence of organized structure in turbulent flow was, at one time, considered to be unlikely. When found, it was considered a special case since structure in turbulence was found so rarely as Roshko (1976) suggested. One of these special cases was the vortex shedding from a cylinder at Reynolds numbers greater than 10^7 . In the transcritical case the presence of a vortex street is well documented by Roshko (1960) and Chen (1972), however, data on the frequency of shedding is less certain. As reported by Chen (1972) the range of Strouhal numbers over which vortex shedding occurred in the transcritical regime was 0.15 to 0.30. Several factors might affect this, such as surface roughness or free stream turbulence, but the important factor is a vortex street occurs at very high Reynolds number flows. This statement could not be made as forcefully for the supercritical regime.

In the supercritical regime the presence of a vortex street is more complicated than for either the sub or transcritical flow regimes. As stated earlier, in supercritical flow the separation point is at 120° , producing a very narrow wake. When this occurs the presence of a vortex street is not certain. According to Chen (1972), the narrow wake produces a narrow vortex street. The narrow vortex street is unstable and above $Re_c = 5.5 \times 10^5$ it become completely turbulent. The instability can create no ordered arrangement of vorticity in the wake. However, Chen (1972) also notes that by changing the surface roughness or the free stream turbulence in the supercritical Reynolds number range the conversion of vorticity to turbulence can be avoided. The presence or absence of ordered vorticity in the supercritical range is obviously a very complicated problem for which no definitive answer can be made. However, in the transcritical regime there is ample evidence to conclude that a vortex street is present, as shown by Chen (1972).

Another factor effecting the shedding of vorticity, which would effect downwash,

is the change in core growth from the subcritical to the supercritical and transcritical ranges. In the subcritical range the vortex core is considered to be laminar and its growth is well established as

$$\text{Vortex Core Radius} = \sqrt{4 \nu t} \quad (6-5)$$

For this study, the core would grow, over 30 diameters, to be about 7.7 mm. Since the separation radius would grow to about 20 mm the assumption the core is contained in the separation radius, R_{sep} , is acceptable. However, the growth of a vortex core under turbulent conditions is not as well established. For laminar flow diffusion governs core growth. In the turbulent case the addition of convective will significantly change the rate at which a core will grow. No longer simply a diffusion problem, both diffusion and convection must be included. Very little data is available on the growth of a turbulent core. An analogy of the difference can be found by examining the different growths of a shear layer. For a laminar shear layer, the growth of the layer is scaled based on $x^{1/2}$, where as a turbulent shear layer scales as x . Whether the growth of a vortex core follows the same trend is uncertain, but the fact that a vortex core would grow at different rates for subcritical and super or transcritical flows is likely. This is one area where the comparison between this study and full scale would be difficult.

This discussion of Reynolds number mismatch poses as many new questions as answers. The uncertainty in the differences between laboratory experiments and full scale is made even more acute by the fact a full scale stack may be in either the supercritical or the transcritical flow regimes. This would create differences in full scale plume behaviour due to Reynolds number. One conclusion is the downwash velocity model presented is effective in predicting trajectories for plumes in subcritical flow, as Figure 6-10 indicates. Its effectiveness for plumes in supercritical or transcritical flow is, at this time, uncertain. However, there are certain characteristics which can be transferred between different Reynolds numbers flows, such as base pressure coefficient, wake growth, and the presence of a vortex street. Any further comparisons require additional investigation.

6.7 Application of the Downwash Velocity model to Buoyant Plumes

This study was conducted on momentum jets only. However, most industrial plumes are driven by not only momentum but also by buoyancy. Therefore, if the downwash velocity model is to be universally applicable, it must apply to cases where

buoyancy is the dominant force. To determine what effect buoyancy will have on the trajectory of a plume three cases were examined.

A set of sample calculations were performed for a full size stack with momentum and buoyancy driving the plume. A 2 m diameter stack, in a 5 m/s (18 km/hr) cross wind was modeled at three momentum ratios ($M = 0.5, 1.0, 2.0$) and three density ratios ($\rho_p/\rho_a = 1.0, 0.75, 0.5$). Figure 6-18 illustrates the different trajectories the downwash velocity model would predict under the different circumstances.

The case where $\rho_p/\rho_a = 1.0$ is the non-buoyant plume. Comparing that plume trajectory to the trajectories when the plume has buoyancy indicates that significant increases in rise height occur when buoyancy is present. One interesting point is that when $M = 1.0$ buoyant plume rises after being downwashed. This indicates that near the stack the rise is dominated by the momentum term and the stack tip pair can push the plume down. However, as the plume moves further downstream the buoyancy term dominates the momentum term. This makes sense when the $h \propto x^{1/3}$ term for momentum is compared to the $h \propto x^{2/3}$ term for buoyancy in Equation 2-9. The increasing buoyancy force enables the plume to lessen the influence of the downwash velocity. As the buoyancy of a plume increases (for the same M) it will more easily overcome downwash. However, before any definite conclusions concerning the downwash velocity model's application to buoyant plumes are made greater investigation into buoyant plumes should be done.

6.8 Empiricism in the Downwash Velocity Model

In deriving the downwash velocity model three fundamental factors were determined using various amounts of empirical manipulation. These factors were:

- **Wake Growth Exponent, n .** The constant n , has a low level of empiricism. This constant was determined by comparing measured values of wake growth power for 2D and 3D wakes with powers predicted by theory. The eventual choice of the $n = 0.4$ exponent was determined by experimentation but is also the average of the 2D and 3D theoretical values of n .

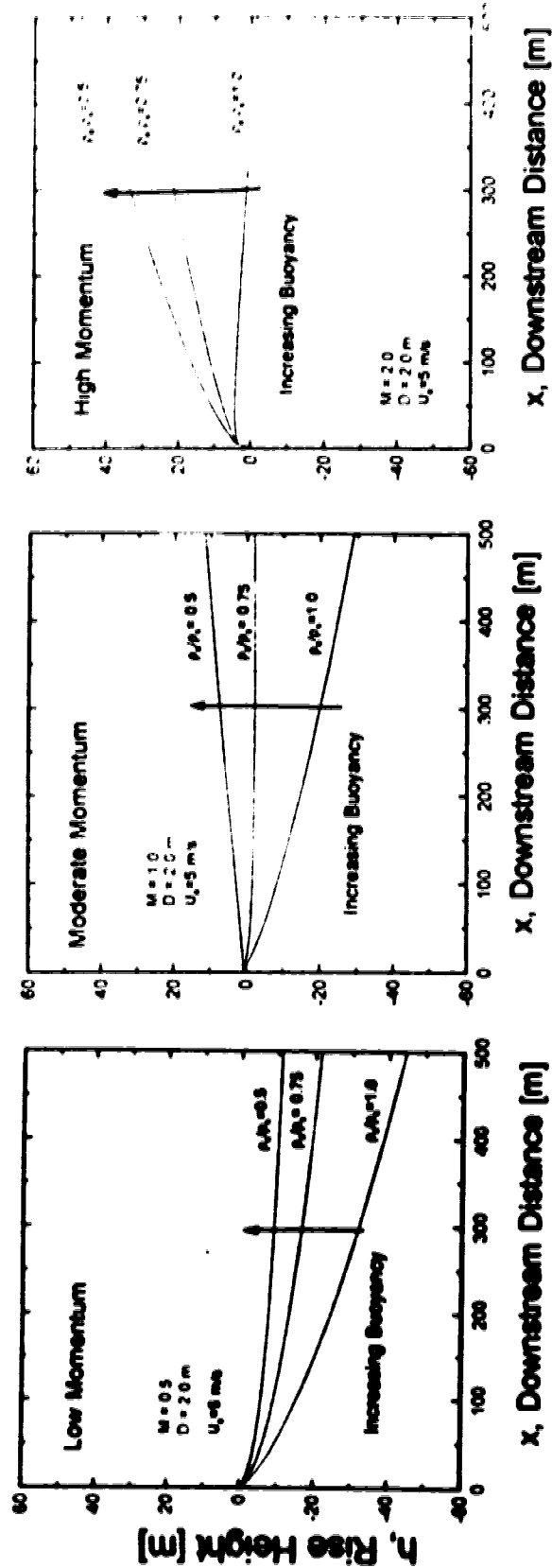


Figure 6-18: Rise of typical buoyant stack gas plumes for various momentum and density ratios ($U_g = 18$ Km/hr, $D = 2$ m, $Q_g = 15.71$ m³/s).

- **Entrainment Coefficient, β .** The entrainment coefficient possess a moderate amount of empiricism. The function used to describe entrainment was determined by fitting different curves through experimentally derived values of β for different momentum ratios. The determination of the best fit was entirely empirical. The determination that β varies was found through consideration of the dynamics of the problem and confirmed by experimental data. That a plume with $M = 8.0$ spends 85% of its rise with $\theta > 45^\circ$ suggests the entrainment would not be the same for a plume with $M = 0.25$, which is bent-over its entire trajectory. For models where β is varied, the function is usually determined empirically, as in Briggs (1975).
- **Downwash Correction Coefficient, B_3 .** The downwash correction coefficient has a high level of empiricism. Like the entrainment coefficient, the function to describe B_3 was determined by curve fitting. However, when the downwash velocity correction was applied to Snyder and Lawson's (1991) data the predicted trajectories matched the data closely. Certain aspects of the downwash velocity correction are similar to full scale stacks and the question of transferability to full scale plumes requires further study. The current model predicted the downwash of a plume in subcritical stack Reynolds number very well.

Chapter 7

Summary and Recommendations

7.1 Summary

The primary goal of this thesis was to present a new approach to modelling downwash in stack gas plumes and compare it to Briggs' virtual origin model and the initial entrainment model. The downwash velocity model incorporates the effects of a time averaged pair of diverging line vortices in the rise of a plume. The line vortices are assumed to be imbedded in the wake at the stack tip and separate at the same rate as the wake. The line vortices produce a negative velocity which causes a downward displacement of the plume. The two key components of the downwash velocity model investigated were the existence of a vortex pair at the stack tip and the growth of the momentum wake at the stack tip.

In Chapter 2, the plume rise model used in this thesis was presented and an equation for the rise of a fully bent-over plume derived. The effects of various entrainment assumptions on plume trajectories were also considered. In order to provide a comparison to the downwash velocity model, two additional downwash models were presented. Briggs' virtual origin model and an initial entrainment model for downwash were discussed and equations for predicting downwash derived. Finally, the downwash velocity model was developed and its assumptions and limitations discussed.

In Chapter 3, the experimental apparatus and methods were outlined. First, the Laser Doppler Anemometer components and operation used to collect velocity data were briefly discussed. The mechanisms of laser induced fluorescence were then introduced. Images were collected on video tape to permit reduced time playback to allow a maximum number of images to be processed. An ensemble average was taken of the stored images and saved for computer manipulation by digital image processing equipment. A description of the specific image processing techniques developed to infer the plume fluid concentration from the digital ensemble averaged image was then given. Image correction and conversion to concentration was summarized. Finally, the methods of analyzing the image to determine plume centroids, used to plot plume trajectories, were developed.

Chapter 3 also described a new and innovative method for applying fluorescein dye directly to a surface. This method used a Butyrate dope as a binder which

suspended fluorescein particles rather than dissolving them. The fluorescein particles were then dissolved by the passing flow and used to track the vorticity produced on the stack surface.

Chapter 4 covered the investigation of the structure of vorticity shed from a finite cylinder, using the method of applying fluorescein outlined in Chapter 3. This section of the thesis produced data which supported the idea of a stack tip vortex pair. The von Karman vortex street shed from a finite cylinder was oblique to the stack and each packet of the vortex street was connected to its adjacent packets by horizontal cross connecting vortices. The streamwise projection of these bridges from many shed vortices produce a time averaged vortex pair. This conclusion is consistent with data from other investigations, such as Sherlock and Stalker (1941) and Maull and Young (1973). The vortex pair was not continuous, but existed as a time average. Flow visualization also demonstrated that when a high velocity jet was issuing from the stack, the connection of the vortex street became embedded in the plume and was carried up with the plume. This change in the connection of the vortex street reduced the downwash of the plume by altering the structure of the time averaged vortex pair.

Chapter 5 reported the results of the Laser Doppler Anemometer experiments conducted in the water channel and at the stack exit. The results of an investigation into the wakes produced behind a cylinder for three conditions were also discussed. The first wake examined was a two-dimensional wake, the second was the wake growing along the stack height and third was the wake behind the stack tip height when a strong jet exited the stack. Using the LDA measurements, the exponent of the wake growth at the stack tip was determined to be $n = 0.40$. This was based on both the experimental values determined in this study (all within 5% of $n = 0.40$), and an average of the theoretical values ($n = 0.50$ and $n = 0.33$ for a two and three dimensional wake).

Chapter 6 presented an analysis of the effectiveness of the virtual origin, initial entrainment and the downwash velocity corrections in predicting plume trajectory. The virtual origin and initial entrainment models were found to lack the flow needed to accurately predict the trajectories of plumes being downwashed. Briggs' virtual origin correction was applied to the data collected in this study, and did not accurately predict the trajectory of a downwashed plume. Briggs' correction assumed that the effects of downwash could be lumped at the origin of the rise and did not affect the functional form of the plume rise. The experimental data clearly illustrates

that the plume experiences downwash along its entire trajectory and the function of the trajectory differs when downwash is experienced. The initial entrainment correction was also compared to the experimental data with equally poor results. The initial entrainment model was able to predict only positive rise heights, an unacceptable result considering the large negative displacements (below the stack tip) observed for plumes with momentum ratio less than 1.0.

The downwash velocity model was robust in its prediction of plume trajectories, matching the experimental data very closely. The downwash velocity model was found to accurately predict, for subcritical Reynolds number flows, the trajectory of plumes ranging from $M = 0$ to $M = 8.0$. A discussion of the effects of increasing Reynolds number on the downwash velocity model was conducted, highlighting some of the differences and similarities between modelled and full scale plumes. To predict plume trajectories in super or transcritical Reynolds number flows using the downwash velocity model, the changing effects of base pressure coefficient, growth of the wake and vorticity shed from the stack must be considered, a task beyond the scope of the present study.

The effects of the entrainment coefficient on plume trajectories were also investigated. In this thesis an entrainment coefficient which is a function of the momentum ratio, M , was used and was found to predict plume trajectories more accurately than a constant entrainment coefficient of $\beta = 0.6$. Chapter 6 ended by considering the level of empiricism which the downwash velocity model included.

Using the simple assumption that the line vortices grow apart as the wake separates produces an easy to use closed form solution for a downwash velocity, which very accurately corrects the trajectory of a downwashed plume. The downwash velocity model appears to be a positive step forward in the prediction of downwash.

7.2 Recommendations

In the future a more thorough investigation of the vortex shedding from a finite cylinder should be undertaken to try and determine the strength of the time averaged streamwise vortices. Also, the structure involved in the von Karman vortex street connection into a jet exiting the stack should also be examined. This would permit comparison between the downwash correction coefficient, B_p , determined in this study and its theoretical value, in Equation 2-33, which includes the strength of the vorticity.

The inclusion of an effective vortex pair in the downwash velocity model is a

good first attempt in modelling downwash. Yet, the results of the flow visualization experiment suggest improvements which could be made to the existing model. To improve the downwash velocity model, it might be more accurate to base the downwash velocity, w_d , on the distance from the streamwise vortex pair at $z = 0$ to the plume centroid at $z = h$. This approach would require an iterative solution to determine the plume height at each downstream position. The next iteration in modelling might also include a component of downwash due to the obliqueness of the vortex street. The angle at which the vorticity is shed and the sign of the vorticity would produce a velocity which would also contribute to downwash.

The importance of vorticity shed off the stack as a mechanism for downwash represents a new physical modelling approach that has been successfully applied in this thesis.

References

Ayoub, A. and Karamcheti, K. (1982) An Experiment on the Flow Past a Finite Circular Cylinder at High Subcritical and Supercritical Reynolds Numbers. *Journal of Fluid Mechanics*, 118, 1-26.

Batchelor, G.K. (1967) *An Introduction to Fluid Dynamics*. Cambridge University Press.

Bays-Muchmore, B., and Ahmed, A. (1992) On Streamwise Vortices in Turbulent Wakes of Cylinders. *Physics of Fluids* 5, 387-392.

Briggs, G.A. (1973) Diffusion Estimation for Small Emissions. ATDL No. 79. Atmospheric Turbulent Diffusion Laboratory, NOAA Environmental Resources Laboratory, Oak Ridge, TN.

Briggs, G.A. (1975) Plume Rise Predictions. *Lectures on Air Pollution and Environmental Impact Analysis*, D.A. Haugen, Ed., American Meteorology Society, Boston, 59-111.

Briggs, G.A. (1984) Plume Rise and Buoyancy Effects. *Atmospheric Science and Power Production*, D. Randerson, Ed., U.S. Department of Energy DOE/TIC-27601, available from NTIS as DE84005177, 327-366.

Bryant, L.W. (1949) The Effects of Velocity and Temperature of Discharge on the Shape of Smoke Plumes from a Funnel or Chimney in a Wind Tunnel. *National Physical Laboratory*. Great Britain, 1-14.

Campbell, R.P. (1991) Image Processing Techniques For Analysis of Full Color Turbulent Jet Images. M.Sc. Thesis. University of Alberta, Edmonton, Alberta.

Carhart, R.A. and Policastro, A.J. (1991) A Second Generation Model for Cooling Tower Plume Rise and Dispersion-I. Single Sources. *Atmospheric Environment*. 25A, 1559-1576.

Chen, Y.N., (1972) Properties of the Karman Vortex Street. Sultzer Technical Review, , 68-80.

Coelho, S.L.V., and Hunt, J.C.R. (1988) The Dynamics of the Near Field of Strong Jets in Crossflows. Journal of Fluid Mechanics. **200**, 95-120.

Davidson, G.A. (1989) Simultaneous Trajectory and Dilution Predictions from a Simple Integral Plume Model. Atmospheric Environment. **23**, 341-349.

Davidson, G.A., and Slawson, P.R. (1982) Effective Source-Flux Parameters for Use in Analytical Plume Rise Models. Atmospheric Environment, **16**, 223-227.

Escudier, M.P., and Maxworthy, T. (1973) On the Motion of Turbulent Thermals. Journal of Fluid Mechanics. **61**, 541-552.

Fan, L. (1967) Turbulent Buoyant Jets into Stratified or Flowing Ambient Fluids. California Institute of Technology Report KH-R-15.

Fay, J.A., Escudier, M.P., and Hoult, D.P. (1970) A Correlation of Field Observations of Plume Rise. Journal of the Air Pollution Control Association **20**, 391-397.

Fric, T.K., and Roshko A. (1991) Structure in the Near Field of the Transverse Jet. Turbulent Shear Flows 7. Springer-Verlag, Berlin, Heidelberg.

Hoehne, V.O., and Luce, R.G. (1970) The Effect of Velocity, Temperature, and Molecular Weight on Flammability Limits in Wind-Blown Jets of Hydrocarbon Gases. American Petroleum Institute. **56-70**, 1057-1081.

Hoult, D.P. and Weil, J.C. (1972) Turbulent Plume in a Laminar Cross Flow. Atmospheric Environment. **6**, 513-531.

Hoult, D.P., Fay, J.A. and Forney, L.J. (1969) A Theory of Plume Rise Compared with Field Observations. Journal of the Air Pollution Control Association **19**, 585-590.

Maull, D.J. and Young, R.A. (1973) Vortex Shedding from Bluff Bodies in a Shear Flow. *Journal of Fluid Mechanics*. 60, 401-409.

Morton, B.R., Taylor, G.I. and Turner, J.S. (1956) Turbulent Gravitational Convection from Maintained and Instantaneous Sources. *Proceedings of the Royal Society, Series A*, 234, 1-23.

Moussa, Z.M., Trischka, J.M. and Eskinazi, A. (1977) The Near Field in the Mixing of a Round Jet with a Cross-Stream. *Journal of Fluid Mechanics*. 80, 49-80.

Neiman, O., (1979) M.Sc. Thesis, University of Alberta, Edmonton, Alberta.

Ooms, G. (1972) A New Method for the Calculation of the Plume Path of Gases Emitted by a Stack. *Atmospheric Environment* 6, 899-909.

Overcamp, T.J. and Hoult, D.P. (1971) Precipitation in the Wake of Cooling Towers. *Atmospheric Environment* 5, 751-765.

Overcamp, T.J. and Ku, T. (1986) Effect of Virtual Origin Correction on Entrainment Coefficients as Determined from Observations of Plume Rise. *Atmospheric Environment* 20, 293-300.

Panton, R.L. (1984) *Incompressible Flow*. Wiley and Sons.

Rittmann, B. E., (1982) Application of Two-Thirds Law to Plume Rise From Industrial-Sized Sources. *Atmospheric Environment*. 16, 2575-2579.

Roshko, A. (1960) Experiments on the Flow Past a Circular Cylinder at Very High Reynolds Number. *Journal of Fluid Mechanics*. 10, 345-356.

Roshko, A. (1976) Structure of Turbulent Shear Flows: A New Look. *AIAA*. 14, 1349-1357.

Scorer, R.S., (1959) The Behavior of Chimney Plumes. *International Journal of Air Pollution*. 1, 198-220.

Scorer, R.S., (1968) Air Pollution. First Edition. Pergamon Press Ltd, Headington Hill Hall, Oxford.

Sherlock, R.H. and Stalker, E.A. (1941) A Study of Flow Phenomena in the Wake of Smoke Stacks. Engineering Research Bulletin No. 29, University of Michigan, Ann Arbor, Mich.

Snyder, W.H. and Lawson, Jr., R.E. (1991) Fluid Modeling Simulation of Stack-Tip Downwash for Neutrally Buoyant Plumes. Atmospheric Environment, 25A, 2837-2850.

Sutton, O.G. (1950) The Dispersion of Hot Gases in the Atmosphere. Journal of Meteorology. 7, 307-312.

Walker, D.A. (1987) A Fluorescence Technique for Measurement of Concentration in Mixing Liquids. Journal of Physics E: Scientific Instruments. 20, 86-94.

Weil, J.C. (1988) Plume Rise, Chapter 3 in Lectures in Air Pollution Modeling, A. Venkatkrm and J.C. Wyngaard Eds., American Meteorology Society, Boston, 119-166.

Williamson, C.H.K. (1989) Oblique and Parallel Modes of Vortex Shedding in the Wake of a Circular Cylinder at Low Reynolds Numbers. Journal of Fluid Mechanics. 206, 579-627.

Zelt, B.W. (1991) Ph.D. Thesis, University of Alberta, Edmonton, Alberta.

Appendix A

Derivation of Plume Rise Equations

The plume rise equations are derived through the conservation of mass, momentum and energy for a bent-over plume. The model includes several key assumptions stated in section 2.1.

Conservation of mass for this plume model can be determined by examining a cylindrical control volume through which the plume passes. As the plume rises it is entraining ambient fluid at its edges and is increasing the plume's volume. In the balance of the mass of the plume the entrainment is described by an entrainment velocity, v_e . Therefore, the change in volume flux can be written as

$$\frac{dQ_v}{dx} = 2R_p v_e \quad (\text{A-1})$$

The absence of a π is a convention which was started by Morton, Taylor and Turner (1956) (MTT hereafter).

The amount of buoyancy flux that a plume has is caused by the density difference between the plume and the ambient fluid ($\rho_s - \rho_a$). The actual source buoyancy flux is found by multiplying the source volume flux by the buoyancy flux per unit volume. The source volume flux is

$$Q_s = R_s^2 w_s \quad (\text{A-2})$$

The π has also been dropped in this case. The buoyancy flux per unit volume is

$$g(\rho_s - \rho_a) \quad (\text{A-3})$$

Therefore the total source buoyancy flux is

$$\begin{aligned}
 F_b &= g \left(\frac{\rho_a - \rho_s}{\rho_a} \right) Q_s \\
 &= g \left(\frac{\rho_a - \rho_s}{\rho_a} \right) R_s^2 w_s
 \end{aligned}
 \tag{A-4}$$

This equation has the densities normalized by the ambient density according to the Boussinesq approximation.

The change in buoyancy over the plume trajectory can be found by integrating over a control volume of the plume, see Briggs (1975) and Weil (1988). The result is

$$\frac{dF_b}{dx} = -S \frac{F_m}{U_s}
 \tag{A-5}$$

The new variable S , is the stability parameter. This parameter will be zero for neutrally stable conditions, greater than zero for stable conditions and less than zero for unstable conditions. Since this study was done in neutrally stable conditions the stability parameter will be zero.

The source momentum flux is found in a similar manner to the buoyancy flux. For the bent-over plume the momentum that will be considered is the vertical momentum. The volume flux is already given in Equation A-2 and the vertical momentum per unit volume is

$$\rho_s w_s
 \tag{A-6}$$

The source momentum flux is

$$\begin{aligned}
 F_m &= \frac{\rho_s}{\rho_a} w_s Q_s \\
 &= \frac{\rho_s}{\rho_a} R_s^2 w_s^2
 \end{aligned}
 \tag{A-7}$$

In this case the density is also normalized by the ambient density.

The change in momentum flux is also found through a control volume approach from Briggs (1975) or Weil (1988)

$$\frac{dF_m}{dx} = \frac{F_b}{U_s} \quad (A-8)$$

Using Morton, Taylor and Turner's (1956) definition the entrainment velocity is defined as

$$v_e = \beta w_p \quad (A-9)$$

where β is an entrainment coefficient, constant with x .

For the case of a bent over momentum jet the buoyancy force will be zero. From Equation A-8, this means that the vertical momentum flux will be constant. Therefore, if we write the momentum flux and applying the Boussinesq approximation for any time of the plume rise

$$F_m = w_s Q_s = w_p Q_p \quad (A-10)$$

Now, by using the bent over assumption the volume flux for the plume will be

$$Q_p = R_p^2 U_s \quad (A-11)$$

Substituting this back into Equation A-10 yields

$$F_m = w_p (R_p^2 U_s) \quad (A-12)$$

From MIT's definition of the entrainment velocity and the volume flux definition, another relationship can be found, such that

$$R_p = \beta z \quad (A-13)$$

If Equation A-13 is substituted into Equation A-12 the result is

$$F_m = \beta^2 U_s z^2 w_p \quad (A-14)$$

Now a substitution for w_p is made by noting that

$$w_p = \frac{dz}{dt} \quad (A-15)$$

Equation A-15 is substituted into Equation A-14 to yield

$$F_m = \beta^2 U_a z^2 \frac{dz}{dt} \quad (\text{A-16})$$

Using the substitution $d/dx = U_a d/dt$ and rearranging the equation for integration

$$\int_0^x \frac{F_m}{\beta^2 U_a^2} dx = \int_0^{h_m} z^2 dz \quad (\text{A-17})$$

Performing this integration and solving for h yields

$$h_m = \left(\frac{3}{\beta^2} \frac{F_m}{U_a^2} x \right)^{1/3} \quad (\text{A-18})$$

This is called the "1/3 Law" for momentum rise.

For the case where the plume, rising in neutrally stable conditions, is also effected by buoyancy the stability parameter will be zero. Then the buoyancy conservation equations implies that the change in buoyancy flux will be zero and thus the buoyancy flux will be constant. Equation A-8, the momentum equation can then be easily integrated to

$$w_p Q_p = F_m + \frac{F_b}{U_a} x \quad (\text{A-19})$$

If in Equation A-19, Equation A-11 is substituted for Q_p , Equation A-13 for R_p and Equation A-15 for w_p , an integration can be written where

$$\int_0^h z^2 dz = \int_0^x \left(\frac{F_m}{U_a^2 \beta^2} + \frac{F_b}{U_a^3 \beta^2} x \right) dx \quad (\text{A-20})$$

Performing this integration produces the combined rise equation for a plume with both momentum and buoyant components

$$h = \left(\frac{3}{\beta^2} \frac{F_m}{U_s^2} x + \frac{3}{2\beta^2} \frac{F_b}{U_s^3} x^2 \right)^{1/3} \quad (\text{A-21})$$

If the momentum rise component of Equation A-21 is removed, the remaining expression would express the rise due to buoyancy, which is

$$h_b = \left(\frac{3}{2\beta^2} \frac{F_b}{U_s^3} x^2 \right)^{1/3} \quad (\text{A-22})$$

For the remainder of this Appendix the buoyancy contribution for plume rise will be neglected since this study only examined momentum jets.

The assumption the plume is emitted from a point source is not necessarily correct. It is fairly obvious a plume has an initial radius. To try and account for this a correction is added to Equation A-13. An initial radius, R_o , is included so that the new expression for the growth of the plume will be

$$R_p = \beta z + R_o \quad (\text{A-23})$$

R_o is found by conserving mass from the vertical exit conditions at the source to the bent-over case. This is done so the mass flux and momentum fluxes are the same. R_o is defined by

$$\rho_s \pi R_s^2 w_s = \rho_s \pi R_o^2 U_s \quad (\text{A-24})$$

If Equation A-23 was substituted into Equation A-12 instead of Equation A-13 in the derivation of the momentum rise, Equation A-14 would become

$$F_m = (\beta z + R_o)^2 U_s w_p \quad (\text{A-25})$$

substituting Equation A-15 into Equation A-25 and expanding the terms

$$F_m = \frac{dz}{dt} (U_s (\beta^2 z^2 + 2\beta z R_o + R_o^2)) \quad (\text{A-26})$$

Rearranging the terms, substituting for the time derivative and integrating gives

$$F_m x = U_s^2 \left(\frac{\beta^2 h_m^3}{3} + \beta h_m^2 R_o + R_o^2 h_m \right) \quad (A-27)$$

Transposing U_s and β produces

$$\frac{3 F_m}{\beta^2 U_s^2} x = h_m^3 + 3 \frac{R_o}{\beta} h_m^2 + 3 \left(\frac{R_o}{\beta} \right)^2 h_m \quad (A-28)$$

The RHS of Equation A-28 can be put into the form $(h + R_o/\beta)^3$ by adding a $(R_o/\beta)^3$ to both sides

$$\frac{3}{\beta^2} \frac{F_m}{U_s^2} x + \left(\frac{R_o}{\beta} \right)^3 = \left(h_m + \left(\frac{R_o}{\beta} \right) \right)^3 \quad (A-29)$$

Finally, by solving for h_m

$$h_m = \left(\frac{3}{\beta^2} \frac{F_m}{U_s^2} x + \left(\frac{R_o}{\beta} \right)^3 \right)^{1/3} - \left(\frac{R_o}{\beta} \right) \quad (A-30)$$

where R_o is defined by the initial conditions in Equation A-24.

Initial Entrainment Model

The initial entrainment model for downwash assumes that a mass of ambient air is entrained into the plume close to the stack ($\approx 10D$ downstream). Figure 2-2b illustrates the entrainment model. This additional mass in the plume would cause the radius of the plume to increase. Therefore, the initial radius of the bent over plume would not be R_o but R_d , where R_d is the plume radius after the initial entrainment. A key assumption in this model is that the entrained fluid's vertical velocity is small compared to the plumes vertical velocity at the stack exit. With the addition of the initially entrained fluid, Q_e , the mass balance becomes

$$\rho_s Q_s + \rho_s Q_e = \rho_s \pi R_d^2 U_s \quad (A-31)$$

It is assumed that the density of the plume fluid will have the density of the stack

fluid very close to stack. The vertical momentum balance is then

$$\rho_s Q_s w_s + \rho_s Q_d w_o = \rho_s \pi R_d^2 U_s w_{p,d} \quad (\text{A-32})$$

Since it has already been noted that the entrained fluid has no vertical velocity, w_o in Equation A-32 will be zero. Now, the growth of the plume will be remain the same with the exception of the initial radius. The initial radius will now become R_d such that

$$R_p = \beta z + R_d \quad (\text{A-33})$$

The derivation now proceeds in the same manner as the derivation for the initial radius R_o as shown above. Therefore the equation to describe the plume trajectory with an initial downwash entrainment is

$$h_m = \left(\frac{3}{\beta^2} \frac{F_m}{U_s^2} x + \left(\frac{R_d}{\beta} \right)^3 \right)^{1/3} + \left(\frac{R_d}{\beta} \right) \quad (\text{A-34})$$

In this case R_d is defined by the initial mass and momentum balances. If Equation A-31 were written for the momentum jet where there is no density differences would be

$$Q_s + Q_d = R_d^2 U_s \quad (\text{A-35})$$

If both sides are divided by Q_s and Equation A-2 is substituted for Q_s on the RHS Equation A-35 becomes

$$1 + \frac{Q_d}{Q_s} = \frac{U_s R_d^2}{w_s R_s^2} \quad (\text{A-36})$$

Rearranging to solve for R_d^2 produces

$$\begin{aligned}
 R_d^2 &= \frac{w_i}{U_i} \left(1 + \frac{Q_d}{Q_i} \right) R_i^2 \\
 &= M \left(1 + \frac{Q_d}{Q_i} \right) R_i^2
 \end{aligned}
 \tag{A-37}$$

Appendix B

Length Scales for Vorticity and Dye Diffusion.

We first will consider the vorticity equation

$$\frac{\partial \bar{\omega}}{\partial t} + (\bar{u} \cdot \nabla) \bar{\omega} = (\bar{\omega} \cdot \nabla) \bar{u} + \nu \nabla^2 \bar{\omega} \quad (\text{B-1})$$

The first term of the R.H.S. will be zero since there is no tilting or stretching of the vortex and there is no axial strain. The vorticity equation can be re-written as

$$\frac{\partial \omega_z}{\partial t} = \nu \frac{\partial^2 \omega_z}{\partial x^2} \quad (\text{B-2})$$

Now by writing this equation in polar coordinates we get

$$\frac{\partial \omega_z}{\partial t} = \nu \frac{1}{r} \frac{\partial}{\partial r} \left(r \frac{\partial \omega_z}{\partial r} \right) \quad (\text{B-3})$$

Now we look for a possible similarity solution and find that by using the Buckingham-Pi method we can produce two non-dimensional groups

$$\eta = \frac{r^2}{\nu t} \quad (\text{B-4})$$

$$\omega_z t = g\left(\frac{r^2}{\nu t}\right) \quad (\text{B-5})$$

By using this relationship we can say that

$$\frac{\partial \omega_z}{\partial t} = \frac{\partial}{\partial t} \left(\frac{1}{t} g(\eta) \right) \quad (\text{B-6})$$

which can be expanded to become

$$\frac{\partial \omega_z}{\partial t} = -\frac{1}{t^2} g(\eta) + \frac{1}{t} g'(\eta) \frac{\partial \eta}{\partial t} \quad (\text{B-7})$$

We can also write this in terms of the radius, r , such that

$$\frac{\partial \omega_z}{\partial r} = \frac{1}{t} g'(\eta) \frac{2r}{vt} \quad (\text{B-8})$$

We may now use these bases in order to fully expand the vorticity equation. We can now substitute back into the original vorticity equation and get

$$\frac{\partial}{\partial r} \left(r \frac{\partial \omega_z}{\partial r} \right) = \frac{1}{t} g'(\eta) \frac{2r}{vt} + r g''(\eta) \frac{4r^2}{v^2 t^2} + \frac{r}{t} g'(\eta) \frac{2}{vt} \quad (\text{B-9})$$

Which can be reduced to

$$-\frac{1}{t^2} g(\eta) - \frac{r^2}{vt^3} g'(\eta) = \frac{4}{t^2} \left(g'(\eta) + \left(\frac{r^2}{vt} \right) g''(\eta) \right) \quad (\text{B-10})$$

By cancelling the r^2 terms on both sides of the equation and realizing that $\eta = \frac{r^2}{vt}$

we can write that

$$-g'(\eta) - \eta g''(\eta) = 4(g'(\eta) + \eta g''(\eta)) \quad (\text{B-11})$$

Which can be further simplified to be

$$-(\eta g(\eta))' = 4(\eta g'(\eta))' \quad (\text{B-12})$$

Integrating both sides of the equation we get

$$4\eta g'(\eta) + \eta g(\eta) = B_4 \quad (\text{B-13})$$

If $g(\eta)$ is finite and $\eta=0$ then from Equation B-13 $B_4 = 0$. Now we can write

$$4g'(\eta) + g(\eta) = 0 \quad (\text{B-14})$$

which leads to

$$g'(\eta) = -\frac{1}{4}g(\eta) \quad (\text{B-15})$$

From this equation we can see that the solution will be the decaying exponential with the following form

$$g(\eta) = B_5 \exp\left(-\frac{\eta}{4}\right) \quad (\text{B-16})$$

Now replacing for $g(\eta)$ and η we get

$$\omega_z(r,t) = \frac{B_5}{t} \exp\left(-\frac{r^2}{4vt}\right) \quad (\text{B-17})$$

K_z can be determined by using the relationship for the circulation given by

$$\Gamma = \int_0^{\infty} \omega_z(r,t) 2\pi r dr \quad (\text{B-18})$$

by substituting for ω_z and performing the integral we find that

$$B_5 = \frac{\Gamma}{4\pi v} \quad (\text{B-19})$$

and so we can write the final form of ω_z as

$$\omega_z(r,t) = \frac{\Gamma}{4\pi\nu t} \exp\left(-\frac{r^2}{4\nu t}\right) \quad (\text{B-20})$$

Now if we define a radius, δ_w , such that 90% of the vorticity is contained within that radius we can find an expression for this radius which will be an indication of the diffusive length scale for the vorticity.

We start by defining

$$0.1 \frac{\Gamma}{4\pi\nu t} = \frac{\Gamma}{4\pi\nu t} \exp\left(-\frac{\delta_w^2}{4\nu t}\right) \quad (\text{B-21})$$

which becomes

$$0.1 = \exp\left(-\frac{\delta_w^2}{4\nu t}\right) \quad (\text{B-22})$$

Now by taking the natural log of both sides and solving for δ_w we get

$$\delta_w = 1.52(4\nu t)^{0.5} \quad (\text{B-23})$$

If we now pose this same problem for the diffusion of dye dissolved in water for the same set of circumstances as the vorticity we can find that by following the same derivation as the vorticity we will find that

$$C_z(r,t) = C_o \exp\left(-\frac{r^2}{4K_{dw}t}\right) \quad (\text{B-24})$$

where C_o is the constant that would describe the constant amount of concentration that would be found if the integral

$$C_o = \int_0^\infty C_z(r,t) 2\pi r dr \quad (\text{B-25})$$

was performed.

We would now take the area which contains 90% of the concentration of dye and determine the radius, δ_c , at which this is true. Again, we do this by solving the concentration equation for the radius at which the concentration is $0.1C_0$.

$$0.1C_0 = C_0 \exp\left(-\frac{\delta_c^2}{4K_{dye}t}\right) \quad (B-26)$$

By cancelling the C_0 terms, taking the natural log of both sides and solving for δ_c we find that

$$\delta_c = 1.52(4K_{dye}t)^{0.5} \quad (B-27)$$

To find the ratio of the diffusivity of vorticity and dye we divide δ_w by δ_c and get

$$\frac{\delta_w}{\delta_c} = \frac{1.52(4\nu t)^{0.5}}{1.52(4K_{dye}t)^{0.5}} \quad (B-28)$$

By cancelling all common factors on top and bottom we find that

$$\frac{\delta_w}{\delta_c} = \left(\frac{\nu}{K_{dye}}\right)^{0.5} \quad (B-29)$$

We can recognize from Batchelor that the Schmidt number is $Sc = \frac{\nu}{K_{dye}}$, so we

can write our relationship in terms of the Schmidt number, such that

$$\frac{\delta_w}{\delta_c} = \left(\frac{\nu}{K_{dye}}\right)^{0.5} = Sc^{0.5} \quad (B-30)$$

This can be interpreted to say that any vortex line that is being tracked by dye will diffuse at a rate equal to the $Sc^{0.5}$ faster than the dye.

END

2 8-0 8-9 6

FIN